

NEW APPROACHES TO MULTI-FUNCTIONAL SOFT MATERIALS

by

Seyedali Banisadr

A Dissertation Submitted in
Partial Fulfillment of the
Requirements for the Degree of

Doctor of Philosophy
in Chemistry

at

The University of Wisconsin-Milwaukee

May 2018

ABSTRACT

NEW APPROACHES TO MULTI-FUNCTIONAL SOFT MATERIALS

by

Seyedali Banisadr

The University of Wisconsin-Milwaukee, 2018
Under the Supervision of Professor Jian Chen

Soft robotics is a relatively new, but fast-developing field of science and technology that utilizes soft materials such as polymers in their body structure. Despite significant progress in soft robotic devices, robots that can sense their environments are still very rare. Although some soft robots have exhibited sensing capabilities, they still have not demonstrated synergistic coupling of sensing and actuation. From our perspective, this type of coupling may take us one step closer to fabricate soft robots with autonomous feedback dynamics. In this work, we present new approaches to soft robotic devices, which are fabricated from responsive soft materials and are able to exhibit synergistic coupling of structural color-based sensing and actuation in response to environmental stimuli.

Cephalopods, such as cuttlefish, are excellent models of coupled sensing and actuation. They demonstrate remarkable adaptability to the coloration and texture of their surroundings by modulating their skin color and surface morphology simultaneously and reversibly, for adaptive camouflage and signal communication. Inspired by this unique feature of cuttlefish skins, we present a general approach to remote-controlled, smart films that undergo simultaneous changes of surface color and morphology upon infrared (IR) actuation. The smart film has a reconfigurable laminated structure that comprises an IR-responsive nanocomposite actuator layer and a mechanochromic elastomeric

photonic crystal layer. Upon global or localized IR irradiation, the actuator layer exhibits fast, large, and reversible strain in the irradiated region, which causes a synergistically coupled change in the shape of the laminated film and color of the mechanochromic elastomeric photonic crystal layer in the same region. Complex 3D shapes, such as bending and twisting deformations, can be created under IR irradiation, by modulating the strain direction in the actuator layer of the laminated film. Finally, the laminated film has been used in a remote-controlled inchworm walker that can directly couple a color-changing skin with the robotic movements. Such IR-actuated, reconfigurable films could enable new functions in soft robots and wearable devices.

A crucial aspect of soft robotics is the sensing capabilities of the robot. Colorimetric sensing based on structural colors, mostly photonic crystals, has been explored. A major challenge is overcoming the problems of limited scalability and time-consuming fabrication process, which affect the real-world applications of photonic crystals. Herein, we have developed a new scalable and affordable platform technology for fabrication of stimuli-responsive, interference colored films. Our system is composed of a thin film of a transparent polymer deposited on a metal-coated substrate. The facile fabrication process allows us to create full spectrum of interference colors on both rigid and soft substrates by simply adjusting the thickness of the polymer layer. Furthermore, our films have been used as colorimetric sensors which undergo fast and reversible change of surface color upon changes in environmental humidity. Such polymer-based, responsive interference coloration could empower colorimetric sensing of various environmental stimuli (e.g. humidity, chemicals, heat, and mechanical forces), which could enable a wide range of applications.

To my mother, for her unconditional love, support, and encouragement

,

To my father, who values education and hard work above all

and

To my beloved wife, who has always supported me

TABLE OF CONTENTS

Chapter 1: Introduction

1.1 Introduction.....	1
1.2 Our Vision.....	3
1.3 References.....	4

Chapter 2: Simultaneous Reconfiguration of Surface Color and Morphology

2.1 Introduction.....	6
2.2 Experimental.....	11
2.2.1 Materials.....	11
2.2.2 Preparation and Characterization of liquid crystalline monomers.....	12
2.2.3 Preparation and Characterization of 0.1 wt% SWNT-LCE Nanocomposite Films.....	18
2.2.4 Preparation and Characterization of Crosslinked Polystyrene (PS) Nanospheres.....	20
2.2.5 Preparation and Characterization of Elastomeric Photonic Crystal Films.....	21
2.2.6 Preparation and IR Actuation of the Laminated Films.....	22
2.2.7 Conversion of Image Signals to Audio Signals.....	23
2.3 Results and Discussion.....	24
2.3.1 SWNT-LCE Nanocomposite Films.....	24
2.3.2 Elastomeric Photonic Crystal Films.....	28
2.3.3 The Laminated Films.....	36

2.3.4 IR Actuation of the Laminated Films.....	37
2.4 Conclusion.....	58
2.5 References.....	60

Chapter 3: Soft Films for Responsive Interference Coloration

3.1 Introduction.....	65
3.2 Experimental.....	69
3.2.1 Materials.....	69
3.2.2 Preparation of Thin Films of Metal.....	71
3.2.3 Preparation and Characterization of Thin Films of Polymer on Metal-Coated Substrates.....	71
3.3 Results and Discussion.....	72
3.3.1 Metal Coating.....	72
3.3.2 Polymer Deposition.....	74
3.3.3 Thin-Film Interference Coloration.....	75
3.3.4 Responsive Interference Coloration.....	92
3.4 Conclusion.....	96
3.5 References.....	97

Appendix: Supporting Information for Chapter 2

¹ H-NMR Spectra of Compounds 1, 2a, 3a, 4a, 2b, 3b, and 4b.....	100
--	-----

Curriculum Vitae	107
-------------------------------	-----

LIST OF FIGURES

Figure 2.1. Schematic illustration of the preparation of the laminated film.....23

Figure 2.2. Chemical structures of monomers, crosslinker, and initiator used in the preparation of LCE composites.....26

Figure 2.3. (a) Photograph of the 0.1 wt% SWNT-LCE film. Scale bar: 5 mm. **(b)** SEM image of SWNTs in the 0.1 wt% SWNT-LCE film. The hot-drawing direction is roughly 50° relative to the scale bar. Scale bar: 5 μm.....27

Figure 2.4. SEM image of crosslinked PS nanospheres with diameter ~ 180 nm. Scale bar: 500 nm.....30

Figure 2.5. (a) Photograph and **(b)** Reflection spectrum ($\theta = 90^\circ$) of the self-assembled photonic crystal film. Scale bar: 1 cm.....31

Figure 2.6. SEM image of crosslinked PS nanospheres embedded in PDMS matrix. Scale bar: 2 μm.....32

Figure 2.7. (a) Photograph and **(b)** Reflection spectrum ($\theta = 90^\circ$) of the elastomeric photonic crystal film. Scale bar: 5 mm.....33

Figure 2.8. Photographs of **(a)** top view and **(b)** side view of the elastomeric photonic crystal film. Scale bar: 1 cm.....34

Figure 2.9. (a) Photographs of the elastomeric photonic crystal film before and after being stretched. Scale bar: 5 mm. **(b)** Photographs of the elastomeric photonic crystal film before and after being deformed with a wooden stick. Scale bar: 1 cm.....35

Figure 2.10. Scheme of the laminated film undergoing bending towards the SWNT-LCE side upon IR irradiation.....38

Figure 2.11. (a) Photographs (top view) of reversible bending and unbending of the laminated film in response to global IR irradiation. **(b)** Photograph (side view) of bent laminated film upon global IR irradiation. Scale bar: 5 mm.....38

Figure 2.12. Temperature of the laminated film as a function of on and off cycles of global IR irradiation.....40

Figure 2.13. (a) Reflection spectra ($\theta = 90^\circ$) of the highly deformed region of the laminated film, represented by the encircled area A in Figure 2.11a, before and upon global IR irradiation, respectively. Inset images are corresponding photographs. **(b)** Reflection spectra ($\theta = 90^\circ$) of the less deformed region of the laminated film, represented by the encircled area B in Figure 2.11a, before and upon global IR irradiation, respectively. Scale bar: 5 mm.....41,42

Figure 2.14. Reflection spectra ($\theta = 90^\circ$) of the unbent laminated film before (IR off, 0 s) and after (IR off, 60 s) global IR irradiation.....43

Figure 2.15. Photographs of localized IR actuation in the encircled area A of the laminated film at **(a)** top view and **(b)** side view, respectively. Photographs of localized IR actuation in the encircled area B of the laminated film at **(c)** top view and **(d)** side view, respectively. Scale bar: 5 mm.....45

Figure 2.16. (a) Reflection spectra ($\theta = 90^\circ$) of the encircled area A (Figure 2.15a) of the laminated film before and upon localized IR irradiation, respectively. **(b)** Reflection

spectra ($\theta = 90^\circ$) of the encircled area B (Figure 2.15c) of the laminated film before and upon localized IR irradiation, respectively.....46

Figure 2.17. (a) Schematic illustration of the SWNT-LCE film subjected to a cutting angle of 45° relative to the nematic director. **(b)** Scheme of the laminated film undergoing twisting upon IR irradiation.....47

Figure 2.18. (a) Photographs (side view) of reversible twisting and untwisting of the laminated film in response to global IR irradiation. Scale bar: 5 mm. **(b)** Reflection spectra ($\theta = 90^\circ$) of the encircled area A (Figure 2.18a) of the laminated film before and upon global IR irradiation, respectively. In order to acquire the reflection spectra ($\theta = 90^\circ$) of the laminated film, the fiber optic probe is oriented perpendicular to the plane of the area A of the laminated film for both untwisted and twisted shapes.....49

Figure 2.19. Photographs (top view) of reversible twisting and untwisting of the laminated film in response to global IR irradiation. The top-view photographs are taken at the fixed angle that is perpendicular to the substrate. Scale bar: 5 mm.....50

Figure 2.20. (a) Photographs (top view) of the laminated film-based inchworm walker movements on glass in response to on and off cycles of global IR irradiation. **(b)** Photograph (side view) of the laminated film-based inchworm walker movement from left to right on paper in response to global IR irradiation during the first on and off cycle.....52

Figure 2.21. (a) Photograph and **(b)** audio frequency spectrum of cyan unbent laminated film. **(c)** Photograph and **(d)** audio frequency spectrum of blue bent laminated film upon global IR irradiation. Scale bar: 5 mm.....54

Figure 2.22. (a) SEM image of crosslinked PS nanospheres with diameter ~ 236 nm. Scale bar: 500 nm, and (b) photograph of the self-assembled photonic crystal film. Scale bar: 1 cm.....56

Figure 2.23. Photographs of (a) top view and (b) side view of the elastomeric photonic crystal film comprising crosslinked PS nanospheres with diameter of 236 nm embedded in PDMS matrix. Reflection spectra ($\theta= 90^\circ$) of (c) self-assembled photonic crystal film and (d) elastomeric photonic crystal film, respectively. Inset images are corresponding photographs. Scale bar: 1 cm.....58

Figure 3.1. Chemical structures of PVP (polyvinylpyrrolidone), PC (polycarbonate), and PDMS (polydimethylsiloxane) used in fabrication of the thin-film interference coloration.70

Figure 3.2. Schematic illustration of the preparation of the thin films of polymer on metal-coated substrates.....72

Figure 3.3. (a) Photograph of a glass substrate coated with a thin film of iridium (5 nm thick). (b) Photograph of a PDMS substrate (~750 μm thick) coated with a thin film of iridium (5 nm thick). (c) Reflection spectra of the glass substrate and iridium-coated glass, respectively. (d) Absorption spectra of the glass substrate and iridium-coated glass, respectively. Scale bar: 1 cm.....73

Figure 3.4. Top view photographs of different colors generated by thin films of PVP deposited on iridium-coated glass substrates (thickness of the iridium film= 5 nm). Scale bar: 1 cm.....76

Figure 3.5. Photographs (top view) of different interference colors created by thin films of PC deposited on iridium-coated glass substrates (thickness of the iridium film= 5 nm). Scale bar: 1 cm.....77

Figure 3.6. Top view images of different colors generated by thin films of PVP deposited on iridium-coated PDMS substrates. Thickness of the iridium film is 5 nm. PDMS substrates are ~ 750 μm thick. Scale bar: 1 cm.....78

Figure 3.7. Photographs of different interference color coatings generated by thin films of PVP deposited on iridium-coated glass substrates at **(a)** top view **(b)** side view, respectively. Images of various interference colors created by thin films of PC deposited on iridium-coated glass substrates at **(c)** top view **(d)** side view, respectively. Photographs of different interference colors produced by thin films of PVP deposited on iridium-coated PDMS substrates at **(e)** top view **(f)** side view, respectively. Thickness of the iridium film is 5 nm. Scale bar: 1 cm.....79

Figure 3.8. (a) Cross-sectional SEM image of the thin film of PVP deposited on iridium-coated glass substrate. Scale bar: 500 nm. Inset image is the corresponding photograph taken at top view. Scale bar: 1 cm. **(b)** Corresponding reflection spectrum ($\theta_1= 0^\circ$). The fiber optic is oriented perpendicular to the plane of the glass substrate. The arrows on the spectrum show the calculated peak wavelengths for first-order (m_1) and second-order (m_2) reflections, respectively. Thickness of the iridium film is 5 nm.....81

Figure 3.9. (a) Cross-sectional SEM image of the thin film of PVP deposited on iridium-coated glass substrate. Scale bar: 1 μm . Inset image is the corresponding photograph taken at top view. Scale bar: 1 cm. **(b)** Corresponding reflection spectrum ($\theta_1=0^\circ$). The

fiber optic is oriented perpendicular to the plane of the glass substrate. The arrows on the spectrum show the calculated peak wavelengths for first-order (m_1) and second-order (m_2) reflections, respectively. Thickness of the iridium film is 5 nm.....83

Figure 3.10. (a) Cross-sectional SEM image of the thin film of PVP deposited on iridium-coated glass substrate. Scale bar: 1 μm . Inset image is the corresponding photograph taken at top view. Scale bar: 1 cm. **(b)** Corresponding reflection spectrum ($\theta_1 = 0^\circ$). The fiber optic is oriented perpendicular to the plane of the glass substrate. The arrows on the spectrum show the calculated peak wavelengths for second-order (m_2) and third-order (m_3) reflections, respectively. Thickness of the iridium film is 5 nm.....85

Figure 3.11. (a) Cross-sectional SEM image of the thin film of PVP deposited on iridium-coated glass substrate. Scale bar: 1 μm . Inset image is the corresponding photograph taken at top view. Scale bar: 1 cm. **(b)** Corresponding reflection spectrum ($\theta_1 = 0^\circ$). The fiber optic is oriented perpendicular to the plane of the glass substrate. The arrows on the spectrum show the calculated peak wavelengths for second-order (m_2) and third-order (m_3) reflections, respectively. Thickness of the iridium film is 5 nm.....87

Figure 3.12. (a) Cross-sectional SEM image of the thin film of PVP deposited on iridium-coated glass substrate. Scale bar: 1 μm . Inset image is the corresponding photograph taken at top view. Scale bar: 1 cm. **(b)** Corresponding reflection spectrum ($\theta_1 = 0^\circ$). The fiber optic is oriented perpendicular to the plane of the glass substrate. The arrows on the spectrum show the calculated peak wavelengths for second-order (m_2), third-order (m_3), and fourth-order (m_4) reflections, respectively. Thickness of the iridium film is 5 nm.....89

Figure 3.13. Absorption spectrum of the thin film of PVP deposited on iridium-coated glass substrate. Inset image is the corresponding photograph at top view. Thickness of the iridium film is 5 nm. Scale bar: 1 cm.....90

Figure 3.14. Photographs (top view) of the interference color patterns generated by thin films of PVP deposited on iridium-coated glass substrate. To form patterns, a pre-cut plastic stencil mask was used during the sputter coating of iridium. Thickness of the iridium film is 5 nm. Scale bar: 1 cm.....91

Figure 3.15. Effect of the thickness of metal coating on the interference coloration. **(a)** Photo images (top view), and **(b)** reflection spectra ($\theta_1 = 0^\circ$) of the interference coloration generated by thin films of PVP on the glass substrates coated with various thicknesses of iridium (from left to right: 1 nm, 5 nm, and 50 nm). Scale bar: 1 cm.....92

Figure 3.16. (a) A schematic illustration of the mechanism of color change in the thin film of PVP deposited on iridium-coated glass substrate between high and low humidity environments. **(b)** Photographs (top view) of the thin film of PVP deposited on iridium-coated glass substrate in response to mist created by a humidifier. **(c)** Photo images (top view) of the initial response of the thin film of PVP deposited on iridium-coated glass substrate to mist generated by a humidifier. Thicknesses of the PVP and iridium films are ~ 300 nm and 5 nm, respectively. Scale bar: 1 cm.....95

Figure 3.17. Photographs (top view) of the thin film of PC deposited on iridium-coated glass substrate in response to mist created by a humidifier. Thickness of the iridium film is 5 nm. Scale bar: 1 cm.....96

LIST OF TABLES

Table 2.1. Mechanical properties of the 0.1 wt% SWNT-LCE and laminated films at room temperature.....37

LIST OF SCHEMES

Scheme 2.1. Liquid crystal monomer synthesis, (4"-Acryloyloxybutyl) 2,5-di(4'-butyloxybenzoyloxy) benzoate (monomer A).....	13
Scheme 2.2. Liquid crystal monomer synthesis, (4"-acryloyloxybutyl)2,5-di(4'-pentylcyclohexylcarboxyloxy) benzoate (monomer B).....	14
Scheme 3.1. Physical mechanism of the thin-film interference.....	67

ACKNOWLEDGEMENTS

First, I would like to express my sincere appreciation to my advisor, Dr. Jian Chen, for his guidance, instruction, and advice throughout my PhD studies in his research group. His ideas, thoughts, and work ethic have been integral to my professional development. I would like to thank my committee members Dr. James Cook, Dr. Mark Dietz, Dr. Guilherme Indig, and Dr. Alan Schwabacher for their time, valuable feedback, and advice.

I am grateful to Dr. Ryan R. Kohlmeyer, the former member of the Chen group, for his tutorial and willingness to help on preparation and IR actuation of SWNT-LCE nanocomposites. I would like to acknowledge Dr. Heather Owen for her help and instruction on SEM and thin film fabrication. I would also like to thank Dr. Woo Jin Chang for allowing me to use his lab's oxygen plasma equipment with the assistance of his graduate student, Tae Joon Kwak. Thank you to all current members of the Chen group, Ali Altan, Adebola Oyefusi, and Milad Momtaz.

Finally, I would like to sincerely acknowledge my parents for their continuous support throughout my life. Without them, none of my success would be possible. I would like to thank my wife, Jennifer Banisadr, for her love, understanding, support, and positive attitude. She is my best friend and has made my life better in so many ways; encouraging me to believe in myself and supporting me through my graduate studies.

Chapter 1: Introduction

1.1. Introduction

Robotics is an important and fast-growing field of science and engineering. Robots have a broad impact on industries as diverse as manufacturing, medicine, healthcare, military, agriculture, and consumer products. Robots are developed to increase range of motions and functions of machines, and to incorporate some key features into them such as adaptability to environment, ability of decision making, and autonomous operation.¹⁻³ Unlike biological systems, traditional robots have rigid body structures that are usually made of metals, which limits their ability to interact with the environment and handle fragile or irregular objects of various shapes and sizes.

Recently, there has been a growing interest in the field of bioinspired soft robotics.³⁻⁷ Inspired by softness and body compliance features found in animals and marine organisms, including starfish, various methods have been developed to fabricate soft robots from stretchable and flexible materials. Due to their soft nature, soft robots offer several advantages compared with robots built with hard materials; therefore, they may find applications where the conventional hard robots are unsuitable. Soft robots are capable of handling objects that are fragile or complex in shape. Since they have a wide range of motion, they are highly adaptive to sophisticated environments and can maintain their stability when moving in complex terrains. Moreover, due to their soft and deformable body structure, soft robots are less dangerous to work alongside humans in future applications compared with their hard counterparts.

Actuation is a key component of soft robotics. Actuators can convert various forms of stimulation into mechanical deformation and perform mechanical work on the macro-, micro-, and nanoscale. Most soft robots are actuated by pneumatic systems, or electric motors.¹⁻³ To make soft robotic devices smart, responsive soft materials (so-called “smart materials”) have been developed as actuators over the past few decades. Compared with other smart materials, stimuli-responsive polymers have many advantages, such as good processability, excellent corrosion resistance, light-weight, biocompatibility, and the potential to mimic the movements of natural creatures. These smart materials are actuated in response to external environmental stimuli (e.g., heat, chemicals, light or humidity).^{8,9}

Another crucial aspect of robotics is the ability of robots to sense their environments. The softness and morphology of soft robots hinder the use of many conventional sensors, including encoders and metal or semiconductor strain gauges. Among all types of sensors, colorimetric sensing, which transduces environmental changes into visible color changes, provides a simple and powerful detection tool for development of low-cost and low-power sensors.^{10,11}

A promising new strategy towards sensing capabilities in soft robotic devices is to utilize soft materials with structural coloration as sensors.¹⁰ In contrast to chemical dyes, structural colorations are widely found in nature, including cuttlefish, where colors originate from micro- or nanostructures.¹⁰⁻¹⁴ One main advantage of structural colors is that they are not easily degraded by environmental conditions such as ultraviolet (UV) light, heat, oxygen, and moisture. Recently, there has been great interest in fabricating materials with responsive structural colors, which can reversibly change their color upon

exposure to an external stimulus (e.g., heat, chemicals, mechanical strains or light).^{10,15,16} For instance, Asher *et al.* developed a colorimetric glucose sensor for patients with diabetes, which consists of a polyacrylamide hydrogel with pendent boronic acid groups. Their sensor responds to sugars in low ionic strength aqueous solutions by red shifting its diffraction as the sugar concentration increases.¹⁷

Despite significant progress in soft robotic devices, robots that can sense their environments are still very rare. For instance, Morin and coworkers developed a locomotive soft robot which exhibits adaptive camouflage by pneumatic pumping of dye fluids in the microfluidic networks, however their system lacks sensing functionality.¹⁸ Although, some soft robotic devices have exhibited sensing capabilities, they still have not demonstrated synergistic coupling of sensing and actuation. Mimicking the intelligence of natural species in soft robotic systems, that is, realization of soft robots that act autonomously and can adapt to environmental changes, is a long-standing challenge.

1.2. Our Vision

Our perspective for the field of soft robotics is to create robots that are almost entirely created with soft materials and possess coupled sensing and actuation functionalities. This coupling may take us one step closer to fabricate soft robots with autonomous feedback dynamics. Nature has provided us with numerous fascinating examples of coupled sensing and actuation. For instance, cuttlefish has an extraordinary capability to instantly and reversibly change its skin color and morphology in response to environmental stimuli. They use such modulation of their appearance for camouflage and

communication.¹⁹ Another fascinating example can be found in the Venus Flytrap, which has inspired scientists due to its unique features such as automatic closure of leaf upon mechanical stimulation, sub-second-scale actuation, and ability to distinguish insects and other prey from random particles like dust.²⁰

Herein, we report new approaches to soft robotic devices, that are fabricated from stimuli-responsive soft materials and are able to exhibit synergistic coupling of structural color-based sensing and actuation in response to environmental stimuli. Such soft robotic devices may open up new application possibilities as smart artificial skins in soft robotics, wearable devices, sensors, and dynamic camouflage.

1.3. References

- (1) Ilievski, F.; Mazzeo, A. D.; Shepherd, R. F.; Chen, X.; Whitesides G. M. *Angew. Chem. Int. Ed.* **2011**, 50, 1890-1895.
- (2) Shepherd, R. F.; Ilievskia, F.; Choia, W.; Morina, S. A.; Stokesa, A. A.; Mazzeoa, A. D.; Chena, X.; Wang, M.; Whitesides, G. M. *Proc. Natl. Acad. Sci. USA* **2011**, 108, 20400-20403.
- (3) Rus, D.; Tolley, M. T. *Nature* **2015**, 521, 467-475.
- (4) Rogers, J. A.; Someya, T.; Huang, Y. *Science* **2010**, 327, 1603-1607.
- (5) Chortos, A.; Liu, J.; Bao, Z. *Nature Mater.* **2016**, 15, 937-950.
- (6) Kim, S.; Laschi, C.; Trimmer, B. *Trends in Biotechnology* **2013**, 31, 287-294.
- (7) Someya, T.; Bao, Z.; Malliaras, G. G. *Nature* **2016**, 540, 379-385.
- (8) Behl, M.; Zotzmann, J.; Lendlein, A. *Adv. Polym. Sci.*, **2010**, 226, 1-40.

- (9) Oliver, K.; Seddon, A.; Trask, R. S. *J. Mater. Sci.* **2016**, *51*, 10663-10689.
- (10) Burgess, I. B.; Loncar, M.; Aizenberg, J. *J. Mater. Chem. C* **2013**, *1*, 6075-6086.
- (11) Hawkeye, M. M.; Brett, M. J. *Adv. Funct. Mater.* **2011**, *21*, 3652-3658.
- (12) Sun, J.; Bhushan, B.; Tonga, J. *RSC Adv.* **2013**, *3*, 14862-14889.
- (13) Zhao, Y.; Xie, Z.; Gu, H.; Zhu, C.; Gu, Z. *Chem. Soc. Rev.* **2012**, *41*, 3297-3317.
- (14) Fu, Y.; Tippets, C. A.; Donev, E. U.; Lopez, R. *WIREs Nanomed. Nanobiotechnol.* **2016**, *8*, 758-775.
- (15) Ge, J.; Yin, Y. *Angew. Chem. Int. Ed.* **2011**, *50*, 1492-1522.
- (16) Chan, E. P.; Walish, J. J.; Urbas, A. M.; Thomas, E. L. *Adv. Mater.* **2013**, *25*, 3934-3947.
- (17) Alexeev, V. L.; Sharma, A. C.; Goponenko, A. V.; Das, S.; Lednev, I. K.; Wilcox, C. S.; Finegold, D. N.; Asher, S. A. *Anal. Chem.* **2003**, *75*, 2316-2323.
- (18) Morin, S. A.; Shepherd, R. F.; Kwok, S. W.; Stokes, A. A.; Nemiroski, A.; Whitesides, G. M. *Science* **2012**, *337*, 828-832.
- (19) Hanlon, R. *Curr. Biol.* **2007**, *17*, R400-R404.
- (20) Wani, O. M.; Zeng, H.; Priimagi, A. *Nat. Commun.* **2017**, *8*, 15546.

Chapter 2: Simultaneous Reconfiguration of Surface Color and Morphology

2.1. Introduction

Cephalopods, such as cuttlefish, are excellent models of coupled sensing and actuation. They demonstrate remarkable adaptability to the coloration and texture of their surroundings by modulating their skin color and surface morphology simultaneously and reversibly, for the purpose of adaptive camouflage and signal communication.¹⁻³ Inspired by this unique feature of cuttlefish skins, we present a general approach to remote-controlled, soft robots that undergo simultaneous changes of surface color and morphology upon infrared (IR) actuation. The colorimetric sensing in this soft robot is based on structural color materials that are responsive to mechanical forces.

The coloration in cuttlefish skins is due to the chromatophores embedded in sacs which are controlled by multiple radial muscles, as well as the structural colors (iridophores, and leucophores).^{3,4} Cuttlefish also can rapidly change the surface morphology of their skins from smooth to spiky, which is unique in the animal kingdom. This physical change relies on the papillae, a network of dermal erector muscles.⁵ Cephalopods, including cuttlefish, commonly swim in large schools. It is clear that the coordination of the movements of members in a school plays a crucial role for preserving the integrity of the school. Iridophores of their skins provide them with an exceptional means of communication.³ One distinct optical feature of the iridophores is the

dependence of the peak wavelength of the reflected light on the angle of observation/incidence, which is used by members of a school for coordination of their swimming direction. Moreover, the polarized light reflected from the iridophores enable them to communicate with the other members of the group in a hidden way, since cephalopods are especially sensitive to polarized light.³ These unique features of their skins have attracted growing interest in recent years to develop soft material systems and devices to mimic such functions for potential applications in soft robotics and wearable devices.⁶⁻¹⁹

Significant progress has been made recently in engineering some of the key functions inspired by cuttlefish skins.⁶⁻¹⁴ For instance, Morin and coworkers utilized soft robots equipped with microfluidic networks to exhibit active camouflage and displays by pneumatic pumping of chemical dye fluids through the network.⁶ Yu and coworkers developed adaptive optoelectronic camouflage systems that can autonomously sense and adapt to the coloration of their surroundings.⁷ Wang and coworkers demonstrated an electro-mechano-chemically responsive elastomer system that can produce voltage-controlled on-demand fluorescent patterns.⁸ The fluorescent signals result from large deformation of a stretchable elastomer covalently coupled with spiropyran-based mechanochromic molecules under the control of electric fields. More recently, Larson and coworkers reported a highly stretchable electroluminescent material composed of a ZnS phosphor-doped dielectric elastomer layer sandwiched between layers of hydrogel electrodes, which can change illuminance and capacitance under voltage-induced deformation.¹²

The colorations in the aforementioned studies were based on chemical dyes and phosphors. In contrast, structural colorations are widely found in nature, including cephalopods, where colors originate from micro- or nanostructures.²⁰⁻²² As mentioned earlier, one main advantage of structural colors is that they are not easily degraded by environmental conditions such as ultraviolet (UV) light, heat, oxygen, and moisture. An important source of structural colorations is from photonic crystals, which are 1-D, 2-D, or 3-D ordered nanostructures of two or more media with different refractive indices arranged in a spatially periodic fashion. Due to the periodic arrangement of materials with different refractive indices, a photonic bandgap appears, which leads to selective prohibition of the light of certain wavelength from propagating through the photonic crystal. A 3D photonic crystal diffracts light of a specific wavelength as determined by Bragg's law (Equation 2.1):

$$m\lambda = 2nd \sin\theta \quad (2.1)$$

Where m is the order of diffraction, λ is the diffracted wavelength of the incident light, n is the effective refractive index of the system, d is the spacing between the diffracting planes, and θ is the Bragg glancing angle between the incident light and diffracting planes.²³

3D photonic crystals, long-range-ordered lattices assembled from nanospheres, may represent a class of ideal candidates for fabricating optical sensors that can be used to monitor, measure, and display environmental variations in terms of color changes, which can be easily visualized by naked eye. There has been great interest in responsive photonic crystals, which can change the photonic bandgaps upon exposure to external

stimuli such as heat, chemicals, mechanical strains, light, electric fields, and magnetic fields.²⁰⁻²⁷ The approaches to stimulus-responsive photonic crystals include changing the lattice spacing of the photonic crystal and the refractive indices of the constituent materials.²³ For instance, Asher *et al.* have demonstrated the fabrication of temperature-, pH-, and ion-responsive optical sensors by embedding colloidal crystals in polymer hydrogels; these are referred to as intelligent sensors.²⁷

A promising new strategy towards cuttlefish-inspired smart films is to integrate an elastomeric photonic crystal²⁸⁻⁴⁰ with a mechanical actuator⁴¹⁻⁴⁴, where the actuator provides mechanical strains that can induce the out-of-plane deformation and change the photonic bandgap of the elastomeric photonic crystal. Liquid crystalline elastomers (LCEs) are excellent candidates for mechanical actuators because they can translate small molecular movements triggered by an external stimulus such as heat or light into large, fast, and reversible mechanical motions.⁴⁵⁻⁵⁷ However, this new strategy for bio-inspired smart films has been underexplored so far in the literature.

Nematic LCEs have fascinated scientists since 1981 when they were first synthesized by Finkelmann *et al.*⁴⁵ LCEs possess three important features: orientational order exhibited by the mesogenic units in amorphous soft materials, topological constraints via the crosslinks, and a responsive molecular shape due to the coupling between the orientational order and mechanical strain.⁴⁷ These three features have made LCEs excellent actuators.⁴⁸⁻⁵³ Nematic LCEs can exhibit large and reversible elongation or contraction in response to temperature changes. Due to the low thermal-conductivity of LCEs, these types of LCE actuators have a slow response time and cannot be actuated remotely which limits their potential applications.

Carbon nanotubes (CNTs) have high thermal conductivities and excellent mechanical properties, which make them ideal fillers for LCE actuators. Both the multi-walled carbon nanotubes (MWNTs) and single-walled carbon nanotubes (SWNTs) exhibit a photomechanical response.⁵⁸⁻⁶¹ We have previously demonstrated that the IR light-driven LCE composite films based on near IR absorbing fillers, such as single-wall carbon nanotubes (SWNTs) and near IR (NIR) dyes, are suitable candidates for soft robotics applications.^{62,63}

Light-driven actuation is highly desirable for various applications, because it not only offers remote, spatial, and temporal control over the actuators, but also permits sophisticated control over light direction, wavelength, intensity, and polarization.^{43,44} Hence the light allows for complicated actuation movements without using additional energy sources and complex components, which can considerably simplify the design of actuator devices and reduce their sizes and weights. Infrared (IR) light is usually better than either UV or visible light for light-driven actuation, because IR light can penetrate much deeper in most polymeric materials^{48,61} and it generally causes little material damage compared with UV or visible light. In addition, numerous near IR absorbing materials and IR lasers with different wavelengths are available for different target applications.

In the present study, we report a general approach to remote-controlled, smart films that undergo simultaneous changes of surface color and morphology upon IR actuation. The smart film has a reconfigurable laminated structure that comprises an IR-responsive nanocomposite actuator layer and a mechanochromic elastomeric photonic crystal layer, which can be disassembled with appropriate tools and reassembled based

on various needs. Upon global or localized IR irradiation, the nanocomposite actuator layer exhibits fast, large, and reversible strain in the irradiated region, which causes a synergistically coupled out-of-plane deformation of the laminated film and structural color change in the mechanochromic elastomer layer in the same region.

Our IR-actuated laminated film design has brought together several important features: i) Large, fast, and reversible remote-controlled actuation that is suitable for soft robotic applications; ii) Intrinsically coupled change of both surface color and morphology that is inspired by cuttlefish skins; iii) IR laser-induced localized actuation that enables generation of different patterns of surface color and morphology; iv) Reconfigurability of the laminated film through disassembly with appropriate tools and reassembly that can repurpose the film for different uses and reduce the materials cost and waste.

2.2. Experimental

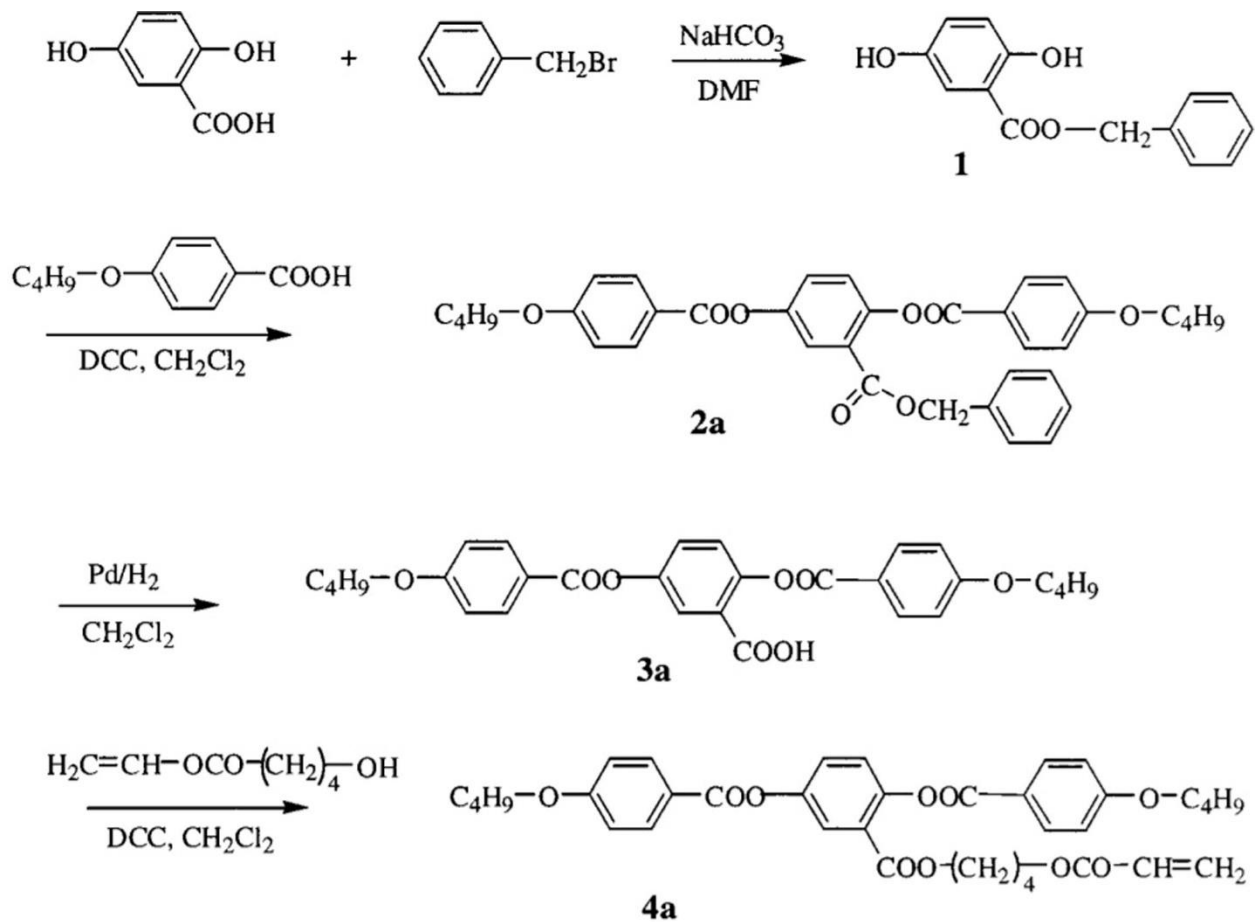
2.2.1. Materials

2,5-Dihydroxybenzoic acid, benzyl bromide, 1,6-hexanediol diacrylate, *N,N*-dicyclohexylcarbodiimide, palladium (5% on carbon), styrene, and divinylbenzene were purchased from Alfa Aesar. Styrene and divinylbenzene were further purified separately by washing with aqueous NaOH (5 wt%) solution three times to remove polymerization inhibitors, followed by washing with deionized water, and drying over anhydrous calcium chloride. *N,N*-dimethylformamide, dichloromethane, chloroform, Irgacure 369 and silicone oil (viscosity: 10 cSt) were purchased from Sigma-Aldrich. Potassium persulfate

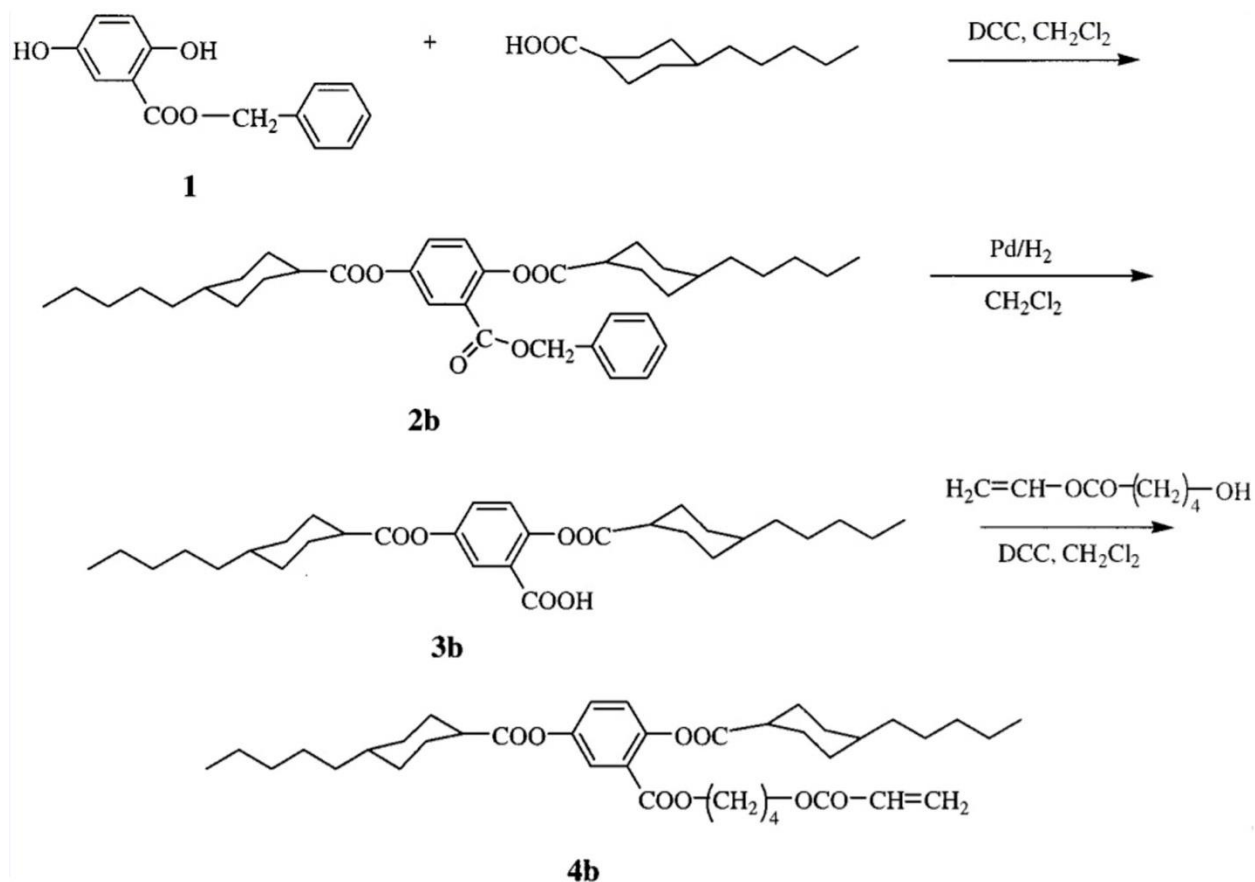
was purchased from Mallinckrodt. 4-Pentylcyclohexylcarboxylic acid, 4-pyrrolidinopyridine, 4-hydroxybutyl acrylate, and sodium dodecylbenzenesulfonate were purchased from TCI America. Standard poly(*p*-phenyleneethynylene)s (PPEs) were synthesized and characterized based on literature.^{64,65} Purified HiPco-SWNTs were purchased from Carbon Nanotechnologies, Inc. Polydimethylsiloxane (PDMS) precursors (Sylgard 184) were purchased from Dow Corning. Hexamethyldisiloxane was purchased from Acros Organics.

2.2.2. Preparation and Characterization of liquid crystalline monomers

(4"-Acryloyloxybutyl) 2,5-di(4'-butyloxybenzoyloxy) benzoate (monomer A) and (4"-acryloyloxybutyl)2,5-di(4'-pentylcyclohexylcarboxyloxy) benzoate (monomer B), were synthesized, purified, and characterized according to literature (schemes 2.1, and 2.2).⁶⁶ The 300 MHz ¹H NMR spectra were recorded on a Bruker DPX-300 spectrometer. All spectra were run in CDCl₃ solution.



Scheme 2.1. Liquid crystal monomer synthesis, (4''-Acryloyloxybutyl) 2,5-di(4'-butyloxybenzoyloxy) benzoate (monomer A).⁶⁶



Scheme 2.2. Liquid crystal monomer synthesis, (4''-acryloyloxybutyl)2,5-di(4'-pentylcyclohexylcarboxyloxy) benzoate (monomer B).⁶⁶

Typical procedures of the synthesis of compounds 1, 2a, 3a, 4a, 2b, 3b, and 4b are described below, respectively. ¹H-NMR spectra of these compounds can be found in Appendix.

Benzyl 2,5-Dihydroxybenzoate (1). 2,5-dihydroxybenzoic acid (10 g, 65 mmol), NaHCO₃ (15.8 g, 188.5 mmol) and DMF (97 mL) were added to a three-necked flask equipped with a reflux condenser. The mixture was stirred and heated at 70 °C for 1 h using a heating oil bath. Subsequently, benzyl bromide (11.12 g, 65 mmol) was added,

and the mixture was heated for 7 h. The reaction mixture was then cooled, diluted with deionized water (300 mL), followed by extraction twice with 150 mL of a 50:50 hexane/ethyl acetate mixture. The organic phases were collected and washed twice with deionized water (150 mL) and dried over Na₂SO₄. After evaporation of the solvents, the residue was recrystallized from hexane (3x) to yield 10.2 g (64%). ¹H NMR (CDCl₃) δ (ppm): 4.7 (s, 1H, OH), 5.39 (s, 2H, CH₂-O), 6.89-7.10 (m, 2H, ArH), 7.4 (s, 1H, ArH), 7.42-7.5 (m, 5H, ArH), 10.35 (s, 1H, OH).

Benzyl 2,5-Di(4'-butyloxybenzoyloxy) benzoate (2a). Benzyl 2,5-dihydroxybenzoate (1) (10 g, 41 mmol), 4-butyloxybenzoic acid (17.5 g, 90.2 mmol), *N,N*-dicyclohexylcarbodiimide (18.61 g, 90.2 mmol), and 4-pyrrolidinopyridine (1.3 g, 9 mmol) and dichloromethane (667 mL) were added to a three-necked flask and stirred at room temperature for 12 h. Subsequently, the *N,N*-dicyclohexyl urea was filtered and the filtrate was washed with water (250 mL), 5% acetic acid solution (250 mL), and water (250 mL) and dried over Na₂SO₄. After evaporation of the solvent, it was recrystallized (3x) from ethanol to yield 17.8 g (73%). ¹H NMR (CDCl₃) δ (ppm): 1.0 (t, 6H, -CH₃), 1.5 (m, 4H, -CH₂-), 1.8 (m, 4H, -CH₂-), 4.01 (t, 4H, -CH₂-O), 5.2 (s, 2H, -CH₂-O), 7.0-7.1 (m, 4H, ArH), 7.3-7.45 (m, 7H, ArH), 7.9 (s, 1H, ArH), 8.14-8.18 (m, 4, ArH).

2,5-Di(4'-butyloxybenzoyloxy) benzoic Acid (3a). 5% palladium on carbon (3.5 g) and 475 mL of dichloromethane were added to a three-necked flask, and the hydrogen was allowed to bubble through the suspension at room temperature. After 15 min, 7.3 g (12 mmol) of the benzyl ether **2a** was added to the reaction flask, and the mixture was stirred

overnight under hydrogen. The progress of the reaction was monitored by TLC (50:50 hexane/ethyl acetate). Subsequently, the reaction mixture was filtered on Celite pad, and then solvent was evaporated to yield 5.6 g (90%) of the product. $^1\text{H NMR}$ (CDCl_3) δ (ppm): 1.02 (t, 6H, $-\text{CH}_3$), 1.52 (m, 4H, $-\text{CH}_2$), 1.84 (m, 4H, $-\text{CH}_2-$), 4.02 (m, 4H, $-\text{O}-\text{CH}_2$), 7.0-7.2 (m, 4H, ArH), 7.3-7.5 (m, 2H, ArH), 7.9 (s, 1H, ArH), 8.12-8.17 (m, 4H, ArH).

(4''-Acryloyloxybutyl) 2,5-Di(4'-butyloxybenzoyloxy) benzoate (4a). A solution of 2,5-di(4'-butyloxybenzoyloxy) benzoic acid (**3a**) (7.6 g, 15 mmol), 4-hydroxybutyl acrylate (2.4 g, 16.5 mmol), *N,N*-dicyclohexylcarbodiimide (3.4 g, 16.5 mmol), and 4-pyrrolidinopyridine (0.2 g, 1.6 mmol) and 238 mL of dichloromethane were added to a three-necked flask and stirred overnight at room temperature. After the *N,N*-dicyclohexylurea was filtered, the filtrate was washed with water (80 mL), 5% acetic acid solution (80 mL), and water (80 mL) and dried over Na_2SO_4 . After solvent evaporation, the crude product was recrystallized (3x) from ethanol. Yield: 6.9 g, 73%. $^1\text{H NMR}$ (CDCl_3) δ (ppm): 1.0 (t, 6H, $-\text{CH}_3$), 1.5-1.7 (m, 8H, $-\text{CH}_2-$), 1.82 (m, 4H, $-\text{CH}_2-$), 4.02-4.15 (m, 6H, $-\text{OCH}_2$), 4.2 (t, 2H, $\text{OCO}-\text{CH}_2$), 5.8 (m, 1H, $\text{CH}_2=\text{C}$), 6.1 (m, 1H, $\text{C}=\text{CH}-$), 6.35 (m, 1H, $\text{CH}_2=\text{C}$), 7.0-7.2 (m, 4H, ArH), 7.3-7.5 (m, 2H, ArH), 7.9 (s, 1H, ArH), 8.15-8.2 (m, 4H, ArH).

Benzyl 2,5-Di(4'-pentylcyclohexylcarboxyloxy) benzoate (2b). Benzyl 2,5-dihydroxybenzoate (**1**) (9.68 g, 39 mmol), 4-pentylcyclohexylcarboxylic acid (17 g, 86 mmol), *N,N*-dicyclohexylcarbodiimide (17.7 g, 86 mmol), and 4-pyrrolidinopyridine (1.27 g, 8.6 mmol) and 390 mL of dichloromethane were added to a three-necked flask and

stirred for 12 h at room temperature. After the *N,N*-dicyclohexylurea was filtered, the filtrate was washed with deionized water (250 mL), 5% acetic acid solution (250 mL), and deionized water (250 mL) and dried over Na₂SO₄. After the solvent evaporation, the crude product was recrystallized (2x) from ethanol. Yield: 14.1 g, 60%. ¹H NMR (CDCl₃) δ (ppm): 0.93 (t, 6H, -CH₃), 1.05 (m, 4H, -CH (EQ)), 1.19 (m, 16H, -CH₂), 1.2 (m, 2H, -CH (AX)), 1.3 (m, 4H, -CH (EQ)), 1.95 (m, 4H, -CH (EQ)), 2.2 (m, 4H, -CH (AX)), 2.51 (m, 2H, -CH (AX)), 5.3 (s, 2H, -OCH₂), 7.1 (m, 1H, ArH), 7.28 (m, 1H, ArH), 7.4 (m, 5H, ArH), 7.72 (s, 1H, ArH).

2,5-Di(4'-pentylcyclohexylcarboxyloxy) benzoic Acid (3b). 5% palladium on carbon (1.36 g) and 409 mL of dichloromethane were added to a three-necked flask, and the hydrogen was allowed to bubble through the suspension at room temperature. After 15 min, 6.55 g (10.8 mmol) of the benzyl ether **2b** was added to the reaction flask, and the mixture was stirred overnight under hydrogen. The progress of the reaction was monitored by TLC (50:50 hexane/ethyl acetate). Subsequently, the reaction mixture was filtered on Celite pad, and then solvent was evaporated to yield 5.4 g (97%) of the product. ¹H NMR (CDCl₃) δ (ppm): 0.9 (t, 6H, -CH₃), 1.0 (m, 4H, -CH (EQ)), 1.18 (m, 16H, -CH₂), 1.2 (m, 2H, -CH (AX)), 1.3 (m, 4H, -CH (EQ)), 1.9 (m, 4H, -CH (EQ)), 2.2 (m, 4H, -CH (AX)), 2.52 (m, 2H, -CH (AX)), 7.1 (m, 1H, ArH), 7.3 (m, 1H, ArH), 7.8 (s, 1H, ArH).

(4''-Acryloyloxybutyl) 2,5-Di(4'-pentylcyclohexylcarboxyloxy) benzoate (4b). A solution of **3b** (10.7 g, 20.8 mmol), 4-hydroxybutyl acrylate (3.17 g, 22 mmol), *N,N*-dicyclohexylcarbodiimide (4.54 g, 22 mmol), and 4-pyrrolidinopyridine (0.33 g, 2.2 mmol)

and 425 mL of dichloromethane were added to a three-necked flask and stirred overnight at room temperature. Subsequently, the *N,N*-dicyclohexylurea was filtered, and the filtrate was then washed with deionized water (300 mL), 5% acetic acid solution (300 mL), and deionized water (300 mL) and dried over Na₂SO₄. After solvent evaporation, the residue was a very viscous oil. Finally, the crude product was purified by crystallization from ethanol (3x) to yield 4.2 g (33%) of the product. ¹H NMR (CDCl₃) δ (ppm): 0.93-1.1 (m, 10H, -CH (EQ)), -CH₃), 1.2-1.4 (m, 14H, -CH (AX)), -CH₂-), 1.5-1.6 (m, 8H, -CH₂-), 1.75-1.9 (m, 8H, -CH (AX, EQ)), 2.1 (m, 4H, -CH (AX)), 2.18 (m, 4H, -CH (AX)), 2.51 (m, 2H, -CH (AX)), 4.2 (t, 2H, -CH₂-OCO), 4.3 (t, 2H, OCOCH₂), 5.8 (m, 1H, CH₂=C), 6.12 (m, 1H, C=CH-), 6.4 (m, 1H, CH₂=C), 7.1 (m, 1H, ArH), 7.3 (m, 1H, ArH), 7.67 (s, 1H, ArH).

2.2.3. Preparation and Characterization of 0.1 wt% SWNT-LCE Nanocomposite Films

The preparation of 0.1 wt% SWNT-LCE nanocomposite films was based on our previous report.⁶³ A 0.25 mg/mL solution of PPE-SWNTs in chloroform was prepared according to literature. The SWNT solution concentration and nanotube loading-level in the film were based only on purified SWNT material and excluded the PPE material. Monomer A (45.5 mg, 0.072 mmol), monomer B (69.1 mg, 0.108 mmol), 1,6-hexanediol diacrylate (3.3 mg, 0.0146 mmol) and Irgacure 369 (0.33 mg, 0.00090 mmol) were transferred into a vial, mixed together. Next, 0.46 mL of 0.25 mg/mL PPE-SWNT solution in chloroform was added. After most of the chloroform was removed by evaporation, the

resulting viscous solution was cast onto a PTFE dish and was heated on a hot plate at 90 °C to remove solvent and air bubbles and then cooled down.

The resulting film was dried under vacuum at 40 °C for 10 min, followed by 10 min of N₂ purging at 40 °C. A Long Wave (365 nm) Ultraviolet (UV) Lamp was used for photopolymerization. The top side of the film was first partially photopolymerized at 40 °C under N₂ with 8 min of 0.97 mW/cm² UV light irradiation. The film was peeled from the PTFE dish and flipped upside down. The film was vacuum-dried at 40 °C for 10 min, followed by 10 min of N₂ purging at 40 °C. The previous bottom side (now top side) of the film was then partially photopolymerized at 40 °C under N₂ with 8 min of 0.97 mW/cm² UV light irradiation. The partially cured film was clamped on both ends with clips and placed in an oven. The film was stretched to a certain length in oven at ~ 40 °C by hanging a weight of 70 g onto the bottom clip. The film was then cooled down and left overnight at room temperature while under tension. Final curing was done by subjecting each side of the film to 10 min of 21 mW/cm² UV light irradiation. After final curing, the film was annealed at 40 °C for 2h to reach an equilibrated state. The stretching ratio of the annealed films for this study was approximately 150%. The stretching ratio of the film is defined by Equation 2.2.⁶³

$$\textit{Stretching Ratio} = (L/L_o)(100\%) \quad (2.2)$$

Where L_o is the initial length of the film and L is the final length of the film after annealing. The intensity of UV irradiation for photopolymerization was measured using a Newport power meter (model 1918-C) with a UV detector (918D-UV-OD3). The nematic-

isotropic (N-I) phase transition temperature of a representative 0.1 wt% SWNT-LCE film is ~ 64.6 °C, which was acquired using a TA Instrument differential scanning calorimeter Q10 under Ar.⁶³ The film thickness was measured with a Mitutoyo Digital Micrometer. Scanning electron microscopy (SEM) was performed using a Hitachi S-4800 field emission scanning electron microscope.

2.2.4. Preparation and Characterization of Crosslinked Polystyrene (PS) Nanospheres

Monodisperse crosslinked PS nanospheres were synthesized by emulsion polymerization, according to a modified literature procedure.⁶⁷ Divinylbenzene, potassium persulfate, and sodium dodecylbenzenesulfonate were used for emulsion polymerization of crosslinked PS particles as crosslinker, initiator and emulsifier, respectively. Initially, styrene monomer (10.0 g) was magnetically stirred with a mixture of divinylbenzene (0.50 g), sodium dodecylbenzenesulfonate (0.084 g) in 120 mL of deionized water at 300 rpm for 15 min in a 250 mL three-necked flask equipped with a reflux condenser. Subsequently, the reaction flask was purged by nitrogen bubbling at room temperature for 15 min, followed by increasing the reaction temperature to 80 °C using a heated oil bath. After keeping the reaction temperature stable for 45 min, potassium persulfate (0.10 g) was introduced into the reaction mixture. The polymerization was terminated after 5 h, followed by cooling down to room temperature. Finally, the residual styrene and sodium dodecylbenzenesulfonate were removed by repeated cycles of washing, centrifugation, and redispersing in deionized water.

The morphology, diameter, and monodispersity of the synthesized PS nanospheres were characterized by SEM. The average diameter (D_n) and the coefficient of variation (C_v) of the particles were determined from SEM observations of 100 particles to ensure the accuracy of measurements according to Equations 2.3 and 2.4, respectively.

$$D_n = (\sum n_i d_i) / (\sum n_i) \quad (2.3)$$

$$C_v = \frac{(\sum (d_i - \frac{\sum n_i d_i}{\sum n_i})^2 / \sum n_i)^{\frac{1}{2}}}{(\frac{\sum n_i d_i}{\sum n_i})} (100\%) \quad (2.4)$$

Where n_i is the number of nanospheres with a diameter of d_i .⁶⁸

2.2.5. Preparation and Characterization of Elastomeric Photonic Crystal Films

First, a thin film of PDMS precursors (base to curing agent ratio = 10:1) was spin-coated on a clean glass substrate, followed by curing at 80 °C for 4 h. Subsequently, the surface of PDMS thin film was rendered hydrophilic by treating with oxygen plasma for 1 min (Zepto, Diener Electronic). To obtain a well-ordered close-packed crystal structure of the PS nanospheres on the plasma-treated PDMS substrate, the silicone oil-covering self-assembly technique was employed.^{69,70} After self-assembly, the silicone oil was carefully removed using Kim wipe, followed by rinsing the film with isopropyl alcohol. Subsequently, the interstitial voids among the PS particles were infiltrated with the PDMS

precursors diluted with hexamethyldisiloxane to reduce the viscosity. The ratio of base:curing agent:hexamethyl disiloxane is 10:1:10. The PDMS precursors were then partially cured at room temperature overnight, followed by removing the excess PDMS precursors, and then fully cured at 70 °C for 3 h. The resulting elastomeric photonic crystal film was then carefully peeled off the substrate using a razor.

Both PS photonic crystal assemblies and corresponding elastomeric photonic crystal films were characterized by SEM and reflection spectroscopy. The reflection spectra were acquired using a fiber optic VIS-NIR spectrometer (USB2000, Ocean Optics).

2.2.6. Preparation and IR Actuation of the Laminated Films

The preparation procedure for the laminated films is schematically illustrated in Figure 2.1. First, a thin layer of PDMS precursors (base:curing agent mixing ratio = 10:1) was applied to a 0.1 wt% SWNT-LCE nanocomposite film as glue, and the resulting film was then placed onto the elastomeric photonic crystal film. The silicone glue was allowed to fully cure at room temperature for 48 h. The thickness of silicone glue layer was measured by digital optical microscopy. Mechanical properties of the 0.1 wt% SWNT-LCE and laminated films were characterized using a Shimadzu Autograph AGS-J universal tester with a 500 N cell load and pneumatic side-action grips. Tensile tests were carried out along the strain direction of SWNT-LCE films at a strain rate of 0.5 mm/min at room temperature.

For global IR actuation, where the whole film was exposed to IR irradiation, the Torch flashlight (Wicked Lasers), which provides >90% of the light in the NIR region, was used as a NIR light source at a light intensity of 11 mW mm⁻². For localized IR actuation, where only selected film region was exposed to IR irradiation, the 808 nm IR laser was used as a NIR light source at a light intensity of 45 mW mm⁻². The light intensities of NIR light sources were measured using a Newport power meter (model 1918-C) with an IR detector (918D-IR-OD3). Temperatures of the laminated films during IR actuation experiments were measured with a non-contact infrared thermometer (MICRO-EPSILON thermoMETER LS), which was found to be in good agreement (within ± 2 °C) with a traditional thermometer.

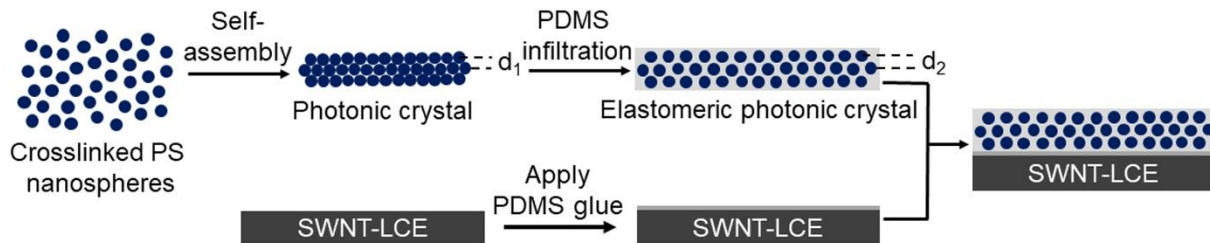


Figure 2.1. Schematic illustration of the preparation of the laminated film.

2.2.7. Conversion of Image Signals to Audio Signals

To demonstrate the feasibility of audio communications, the photographs of cyan unbent and blue bent configurations of the laminated film excluding backgrounds were

converted to audio signals. The sound waves were generated using an image-to-sound converter software (AudioPaint, version 3.0). The software employs a frequency-time grid to process a picture, in which each line of an image correlates with an oscillator. The frequency and amplitude of this oscillator at a given time are determined by the vertical position and color of each pixel, respectively. Fast Fourier transforms of the synthesized sounds on a logarithmic scale were obtained using a sound analyzer software (Sonic Visualiser, version 3.0).

2.3. Results and Discussion

2.3.1. SWNT-LCE Nanocomposite Films

The effective use of SWNTs in polymer-composite applications strongly depends on the ability to disperse them homogeneously throughout a polymer matrix without destroying their integrity. Pristine SWNTs are incompatible with most solvents and polymers, which leads to poor dispersion of the nanotubes in solvents and polymer matrices. Rigid, conjugated macromolecules such as PPE can be used to non-covalently functionalize and solubilize carbon nanotubes while preserving their intrinsic properties and disperse carbon nanotubes uniformly in polymer matrices.^{62-65,71}

The 0.1 wt% SWNT-LCE nanocomposite films were prepared from a mixture of PPE-SWNTs and LCE precursors through a two-stage photopolymerization process coupled with a hot-drawing technique.^{62,63} This method allows us to make relatively thick films where the mesogenic units in the nanocomposite film are well aligned along the hot-

drawing direction.⁶² The typical thickness of a 0.1 wt% SWNT-LCE film used in this study is around 252 μm . The SWNT loading value is based on purified SWNT material only, and excludes the PPE material. Chemical structures of the monomers, crosslinker, and UV initiator that were used to synthesize the side-on LCE matrix are shown in Figure 2.2. We chose this particular type of LCE with side-on mesogenic units because it exhibits muscle-like physical properties; and its N-I phase transition temperature is tunable by controlling the monomer ratio.

The coupling between liquid crystal side chain and backbone is critical to the thermoresponsive behavior of LCE materials. This coupling is strong when the length of the spacer between the liquid crystalline mesogen and the polymer backbone is short. In LCEs, the orientational order of the mesogens induces backbone anisotropy. The radius of gyration has a prolate extended shape in the nematic phase. In contrast, the radius of gyration is spherical in the isotropic phase. The polymer chains between cross-links in an elastomer can undergo similar conformational changes, leading to a shape change that is thermally reversible.⁶⁶

The excellent dispersion of SWNTs in the LCE matrix was confirmed by photography (Figure 2.3a) and SEM (Figure 2.3b). In addition, SEM shows that SWNTs are partially orientated along the hot-drawing direction. The diameters of SWNTs shown in Figure 2.3b are significantly inflated because the SEM image contrast stems from local potential differences between conductive nanotubes and insulating polymer matrix.⁶²

Upon IR irradiation, well-dispersed SWNTs can efficiently absorb and transform IR light into thermal energy, thereby serving as numerous nanoscale heaters uniformly

embedded in the LCE matrix. The absorbed thermal energy, if sufficient, then induces the LCE N-I phase transition, leading to a shape change of the SWNT-LCE nanocomposite film.^{62,63}

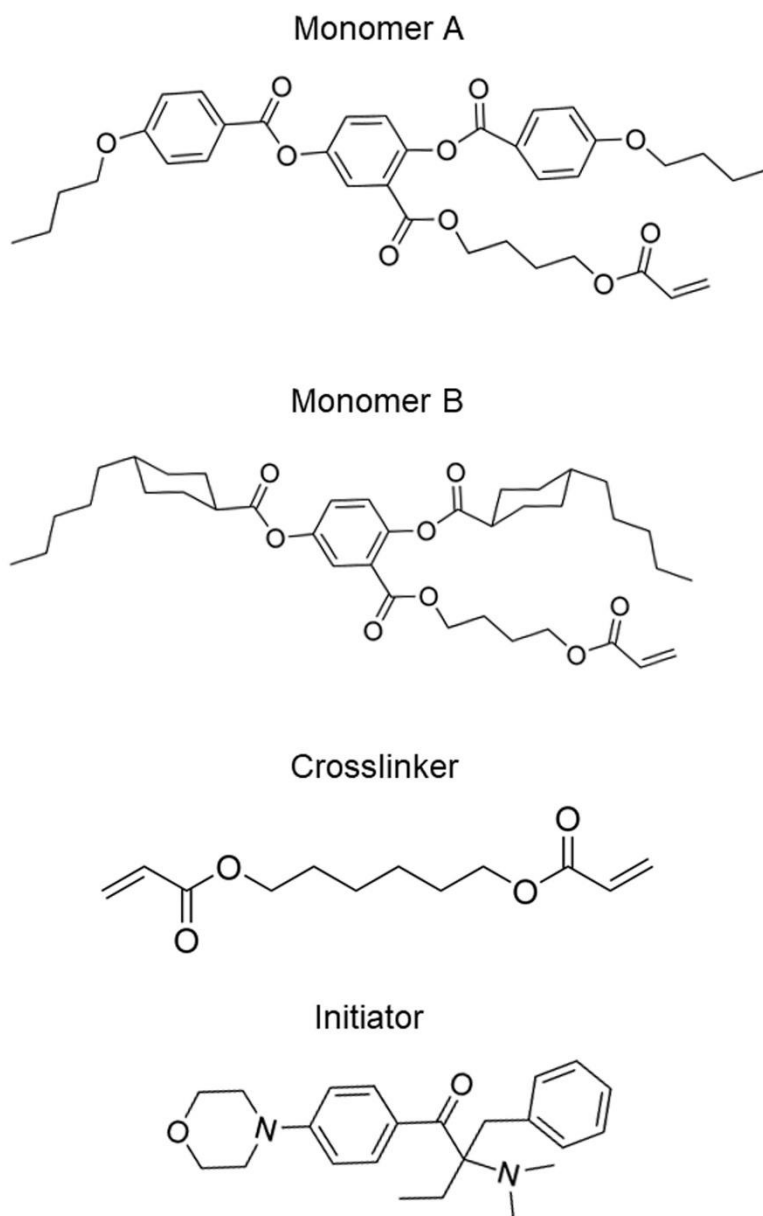


Figure 2.2. Chemical structures of monomers, crosslinker, and initiator used in the preparation of LCE composites.

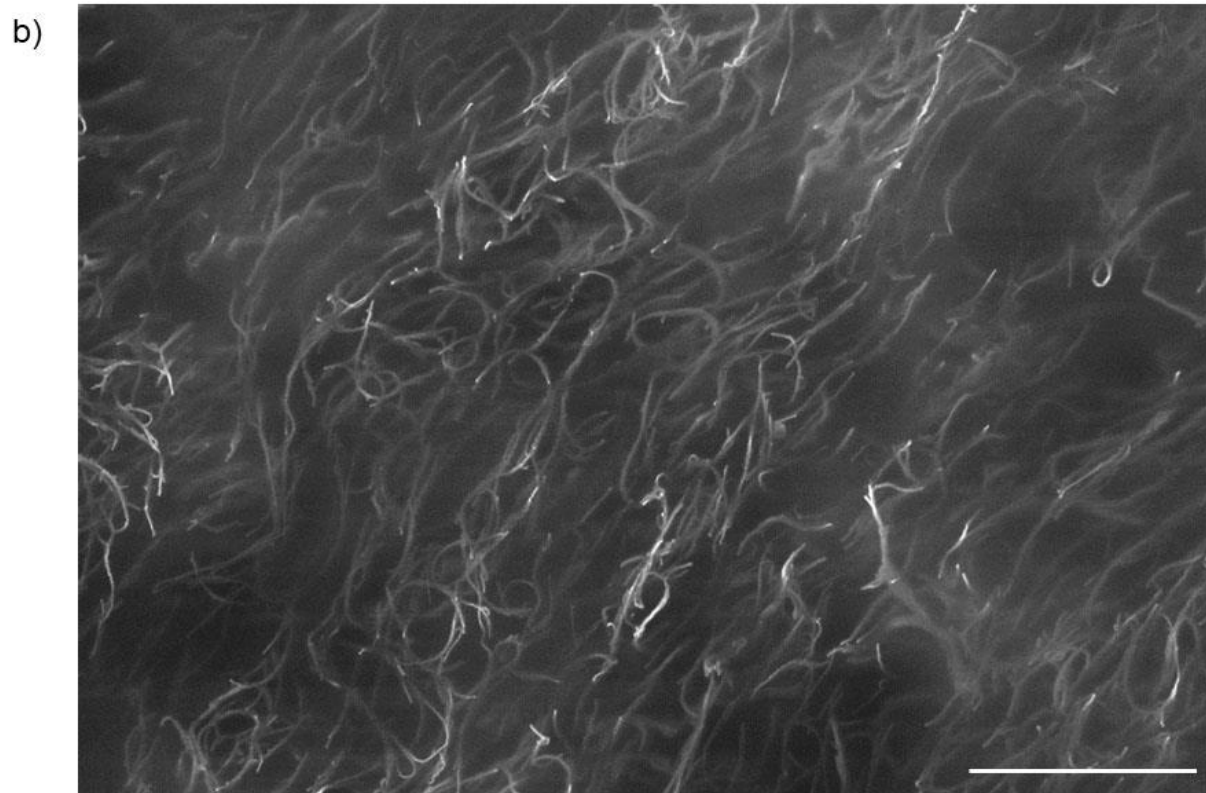


Figure 2.3. (a) Photograph of the 0.1 wt% SWNT-LCE film. Scale bar: 5 mm. (b) SEM image of SWNTs in the 0.1 wt% SWNT-LCE film. The hot-drawing direction is roughly 50° relative to the scale bar. Scale bar: 5 μm .

2.3.2. Elastomeric Photonic Crystal Films

Crosslinked PS nanospheres were prepared using emulsion polymerization, as described in the experimental section. The D_n and C_v of synthesized PS particles are approximately 180 nm and 3.5%, respectively, and the latter clearly indicates highly monodisperse nature of these nanospheres (Figure 2.4).

In all emulsion polymerizations, there are three stages (I, II, III) based on the number of particles and the existence of monomer droplets.⁷² Initially, monomers and surfactants dispersed in water creates relatively large droplets of monomers, and excess surfactants form micelles. During phase I, small amounts of monomers diffuse into the micelles through the water. Subsequently, a water-soluble initiator reacts with monomers in the micelles. In phase II, monomers inside the micelles rapidly undergo polymerization to form polymer particles. At this stage, both monomer droplets and polymer particles exist in the system. As the monomer droplets decrease, the size of polymer particles increases. Eventually the monomer droplets disappear. In stage III, the polymer particles become monomer-starved and the concentration of monomers in the system decrease continuously till the end of polymerization reaction.

The size of the polymer particles can be adjusted by controlling the amounts of emulsifier, initiator, monomer or reaction temperature.⁷³ The polymer particle size is greatly affected by the number of primary nuclei formed in the early stage of emulsion polymerization. The higher amounts of primary nuclei lead to smaller polymer particles. For instance, when the reaction temperature increases, many free radicals are created in a short amount of time resulting in more primary nuclei compared to lower temperatures,

which leads to smaller polymer particles. Emulsifier has also a key role in the emulsion stability and controlling the size of particles. A higher concentration of emulsifier results in a large number of primary nuclei, which leads to smaller polymer particles.

In the past decade, fabrication methods of 3D photonic crystal films have been extensively investigated. Dipping and vertical deposition methods are the common techniques for forming a photonic crystal film on a solid substrate. However, the difficulty in developing a photonic crystal film with a large area is an important issue from an industrial aspect.⁷⁴ In conventional drying, photonic crystal films are self-assembled on a substrate through drying a colloidal suspension covering on a hydrophilic substrate. A ring-shaped film forms at the contact line of the suspension on the substrate, due to the capillary flow from the inner to the outer region of the suspension. To form high quality photonic crystal films from the colloidal suspension on the hydrophilic substrate, silicon oil-covering self-assembly method was used.^{69,70} The surface of the aqueous colloidal suspension was fully covered with a thin layer of hydrophobic silicone oil. In the crystallization process, the capillary flow of the water from the center to the edge was suppressed; therefore, the nanospheres self-assembled into a close-packed colloidal crystal due to the electrostatic interactions between the spheres.

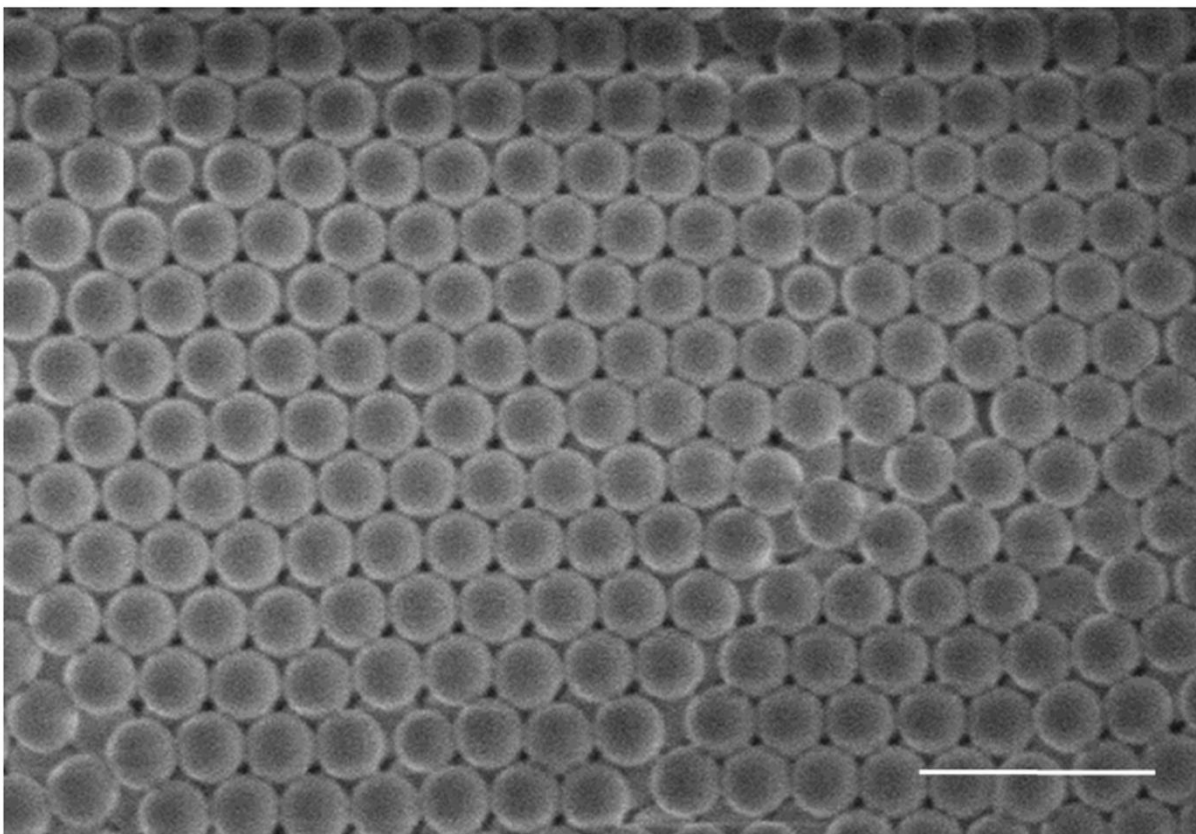


Figure 2.4. SEM image of crosslinked PS nanospheres with diameter ~ 180 nm. Scale bar: 500 nm.

The 180 nm particles formed close-packed photonic crystal assembly (Figure 2.4), which has a bright blue color under normal light incidence ($\theta = 90^\circ$) (Figure 2.5a). As shown in Figure 2.5b, the photonic bandgap corresponding to (111)-crystalline planes generates a Bragg reflection peak at $\lambda = 429$ nm, which was in reasonable agreement with the calculated peak wavelength of 423 nm for 180 nm nanospheres in a face-centered cubic structure using Equation 2.1.

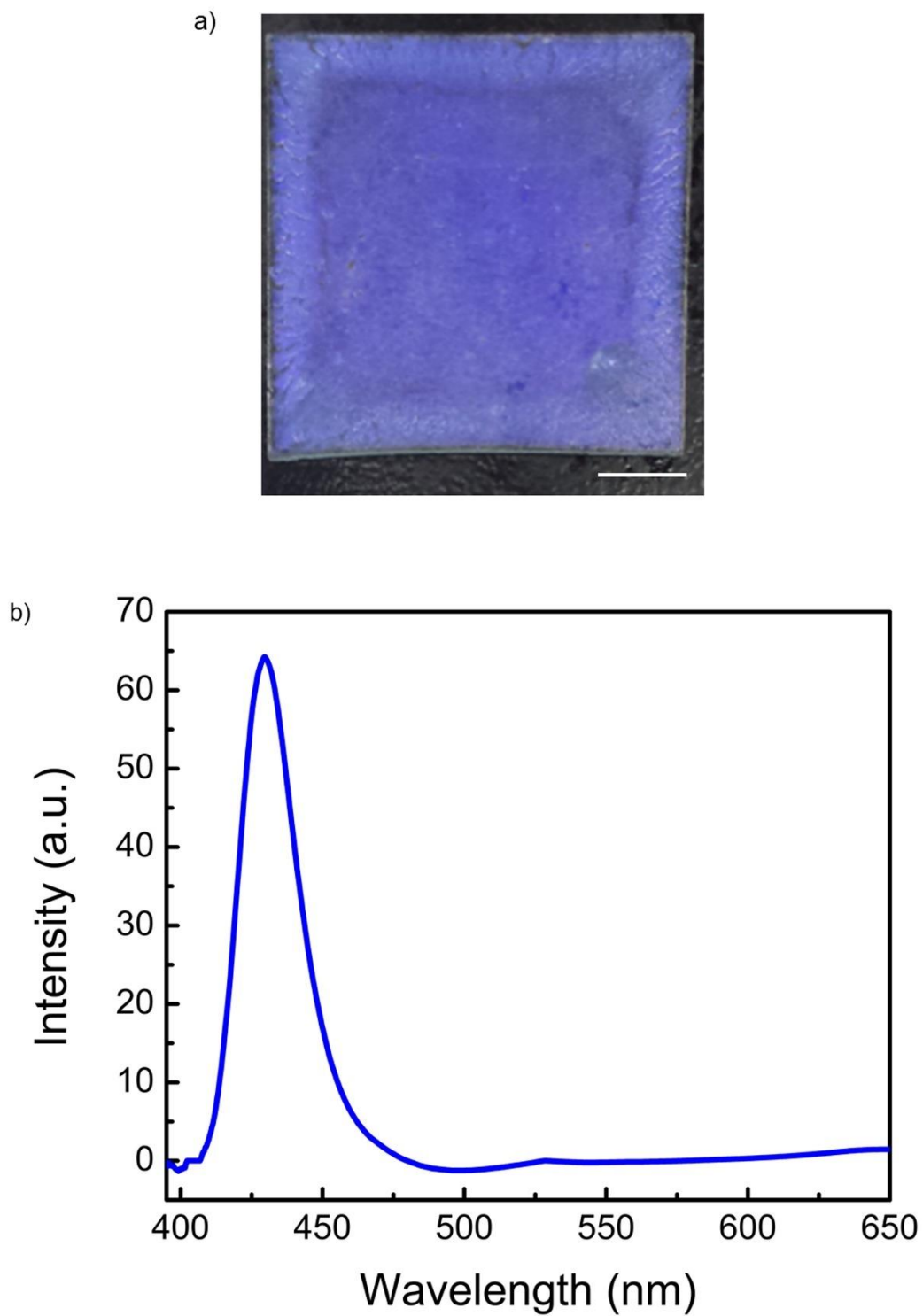


Figure 2.5. (a) Photograph and (b) Reflection spectrum ($\theta = 90^\circ$) of the self-assembled photonic crystal film. Scale bar: 1 cm.

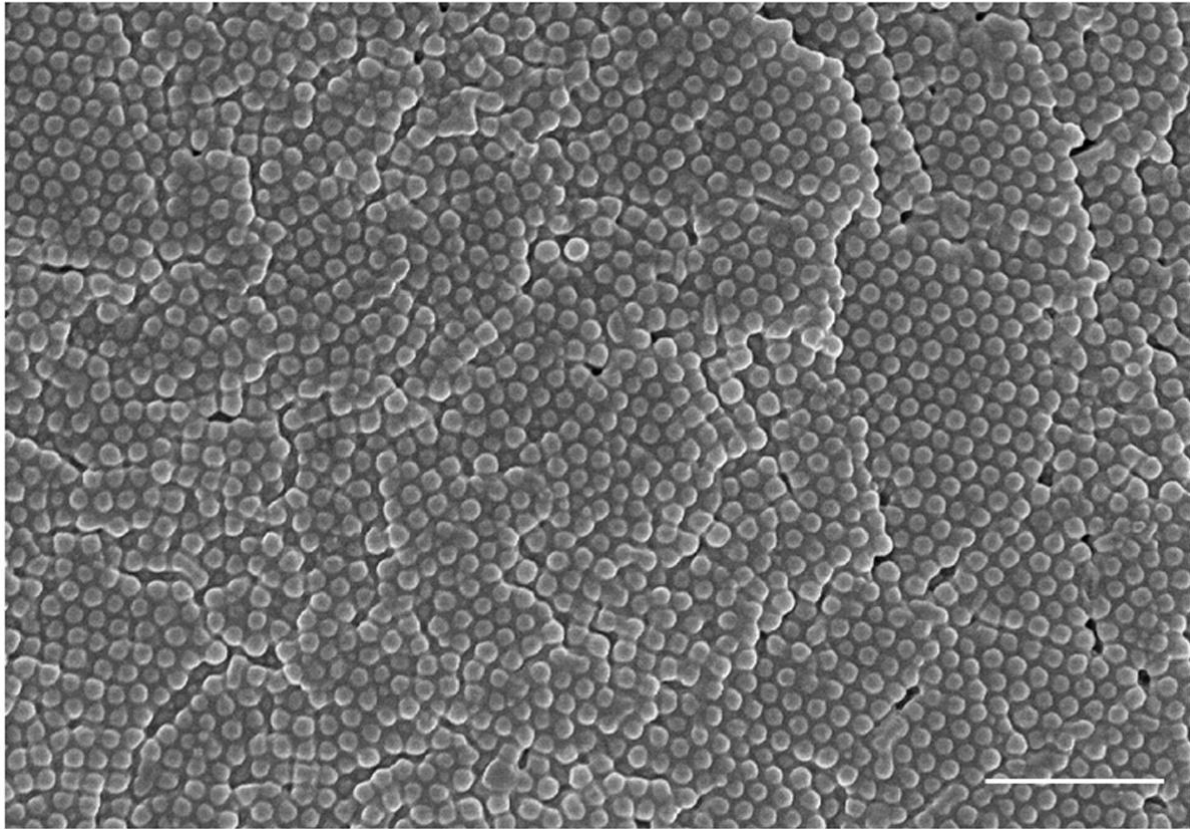


Figure 2.6. SEM image of crosslinked PS nanospheres embedded in PDMS matrix. Scale bar: 2 μm .

The elastomeric photonic crystal film was produced by infiltrating the aforementioned PS photonic crystal assembly with diluted PDMS precursors followed by curing, which leads to a change in the structural color of the film from blue to cyan (Figure 2.7a). The typical thickness of the elastomeric photonic crystal film used in this study is around 23 μm . SEM reveals that the interstitial voids among the PS nanospheres are filled with PDMS (Figure 2.6). Reflection spectroscopy ($\theta = 90^\circ$) confirms that the PDMS infiltration results in a redshift in the photonic bandgap from 429 nm to 507 nm (Figure 2.7b), which is mainly due to an increase in the lattice constant d , as defined in Figure 2.1, from $d_1 = 149$ nm in the PS photonic crystal assembly to $d_2 = 164$ nm in the

elastomeric photonic crystal film. This nanoscale increment in the lattice constant, calculated from the reflection spectra of the films using Equation 2.1, is basically in agreement with the measurements from their corresponding SEM images. The observed increment in distance between the colloidal nanospheres allows the reversible color change of the film.

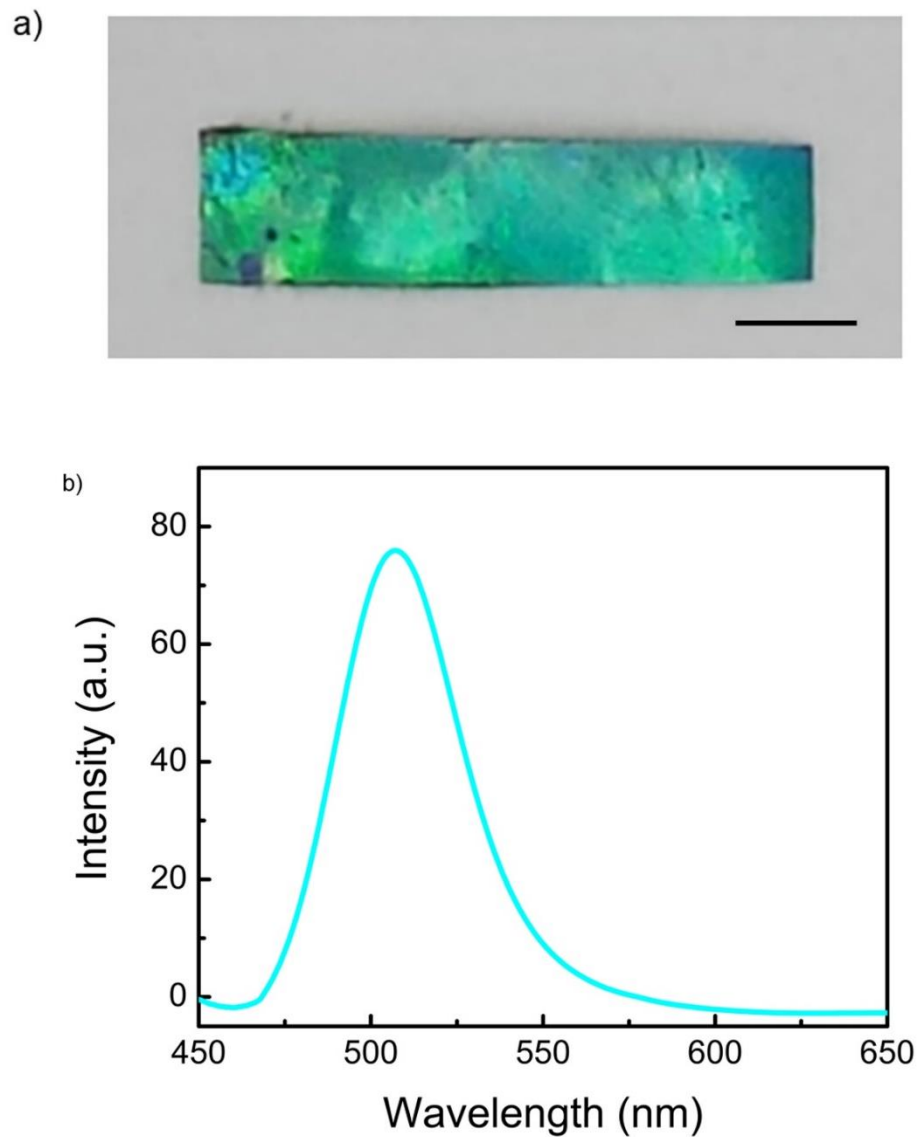


Figure 2.7. (a) Photograph and (b) Reflection spectrum ($\theta = 90^\circ$) of the elastomeric photonic crystal film. Scale bar: 5 mm.

As with other 3D photonic crystals, our elastomeric photonic crystal film exhibits the iridescent reflection color that depends on the viewing angle. The top view, and side view photographs of the elastomeric opal film are shown in Figure 2.8a and 2.8b, respectively.

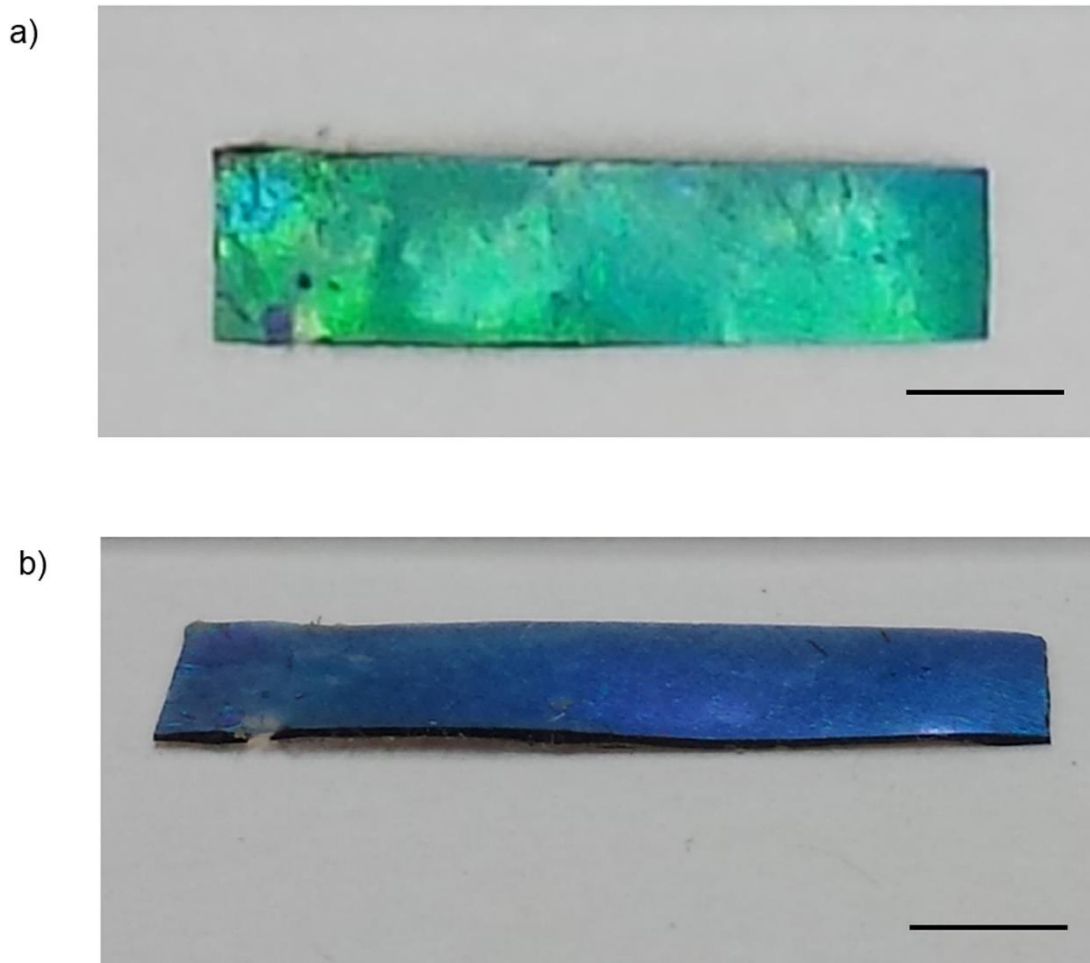


Figure 2.8. Photographs of (a) top view and (b) side view of the elastomeric photonic crystal film. Scale bar: 1 cm.

Furthermore, when the elastomeric photonic crystal film is sufficiently deformed by mechanical stress, the reflected color shifts to a shorter wavelength. Such mechanical deformation and color change are fully reversible. Figures 2.9a and 2.9b show that the structural color of the elastomeric photonic crystal film changes from cyan to blue upon in-plane and out-of-plane mechanical deformations, respectively.

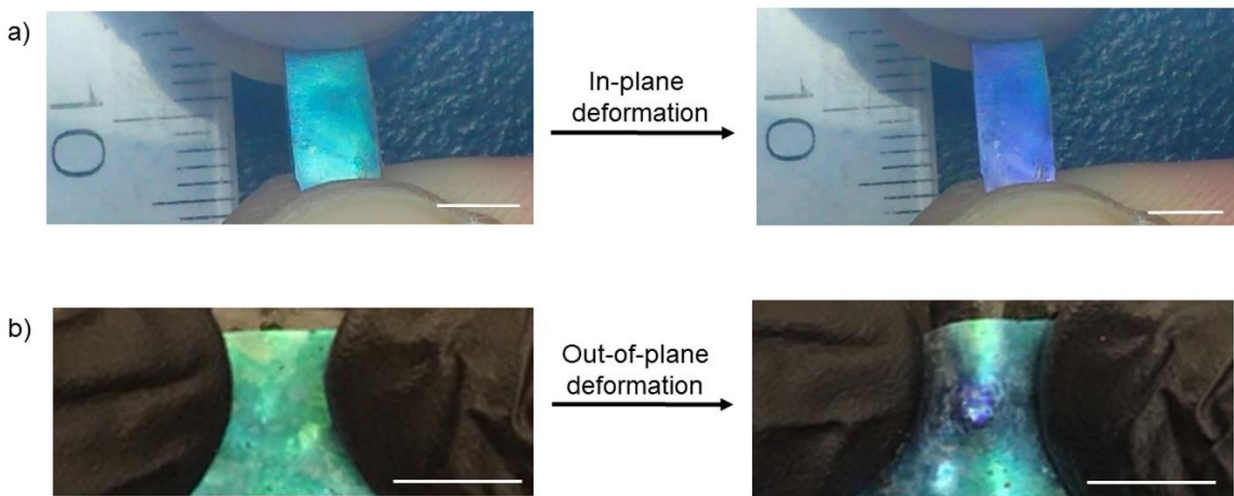


Figure 2.9. (a) Photographs of the elastomeric photonic crystal film before and after being stretched. Scale bar: 5 mm. (b) Photographs of the elastomeric photonic crystal film before and after being deformed with a wooden stick. Scale bar: 1 cm.

There are three color-changing mechanisms in the elastomeric photonic crystal film upon mechanical deformations: i) Decrease in the lattice constant d of the elastomeric opal film, which causes a blueshift in the reflection color of the film; ii) Change in the angle of observation θ , originating from intrinsic viewing-angle dependence of 3D photonic crystal structures; iii) A combination of a decrease in d and θ , which occurs when the elastomeric photonic crystal film experiences out-of-plane mechanical deformation.

2.3.3. The Laminated Films

Mechanical properties of the 0.1 wt% SWNT-LCE and laminated films at room temperature are shown in Table 2.1. These values of Young's moduli are characteristic of elastomers. Compared with the 0.1 wt% SWNT-LCE film, the laminated film exhibits roughly comparable Young's modulus and tensile strength but nearly 40% increase in elongation at break.

In the laminated films, good adhesion between the actuator and structural color layers is crucial for the reversible and steady actuation. Herein, the PDMS silicone resin with a thickness of $\sim 15 \mu\text{m}$ has been employed as the adhesive interlayer to supply sufficient bond strength for restricting the negative in-plane strain-induced contraction of the SWNT-LCE layer. We have never observed any delamination of well-cured laminated films during IR actuation experiments. One additional advantage of using the PDMS silicone glue is that it allows for the disassembly of the laminated film with appropriate tools. We have found that the SWNT-LCE layer can be peeled off intact with tweezers. There is no visible silicone glue residue left on the SWNT-LCE film. Moreover, most of the silicone glue residue left on the elastomeric photonic crystal film can be readily removed using a razor. The facile disassembly of the laminated films with appropriate tools not only allows for full recovery of SWNT-LCE and elastomeric photonic crystal films, but also enables the reconfiguration of laminated films by, for example, recoupling the SWNT-LCE film with another elastomeric photonic crystal film that has different color, or pairing the elastomeric photonic crystal film with another SWNT-LCE film that has different nematic director orientation.

Table 2.1. Mechanical properties of the 0.1 wt% SWNT-LCE and laminated films at room temperature.

Materials	Tensile modulus (MPa)	Tensile strength (MPa)	Elongation at break (%)
0.1 wt% SWNT-LCE film	0.68 ± 0.04	5.5 ± 1.0	41.0 ± 4.9
Laminated film	0.70 ± 0.09	6.3 ± 1.3	57.3 ± 4.9

2.3.4. IR Actuation of the Laminated Films

A schematic diagram of the laminated film is illustrated in Figure 2.10. Upon global IR irradiation using a Torch NIR light source, the SWNT-LCE layer in the laminated film undergoes a significant in-plane negative strain, originating from the bulk N-I phase transition. Due to the PDMS glue-mediated strong mechanical coupling of the SWNT-LCE layer with the elastomeric photonic crystal layer, the in-plane contraction of the SWNT-LCE layer is impossible and instead the in-plane negative strain bends the elastomeric photonic crystal layer towards the SWNT-LCE side (Figure 2.10). The IR-induced bending actuation of the laminated film is large, fast, and reversible, which causes a simultaneous color change of the elastomeric photonic crystal film from cyan to blue (Figure 2.11a). Figure 2.11b shows the side-view image of the IR-induced bent laminated film, which indicates the curvature of the film reaches 0.28 mm^{-1} only after 15 seconds of global IR irradiation. The IR-induced bending curvature of the laminated film can be controlled by tuning the IR light intensity or the film thickness.⁶² The IR-induced

curvature of a laminated film increases with higher IR light intensity and thinner mechanochromic layer.

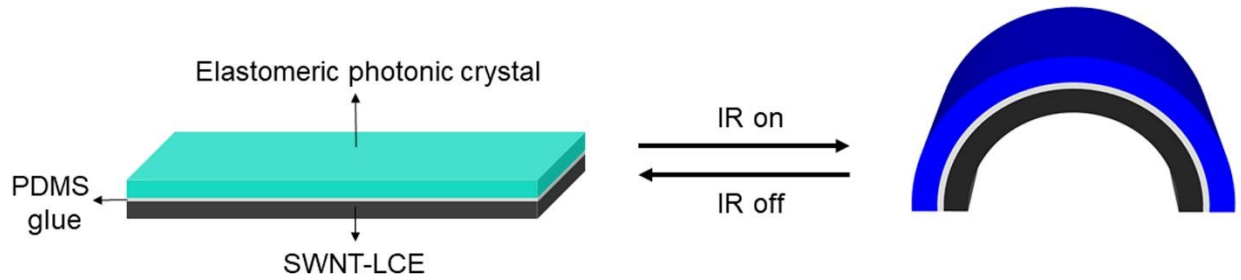


Figure 2.10. Scheme of the laminated film undergoing bending towards the SWNT-LCE side upon IR irradiation.

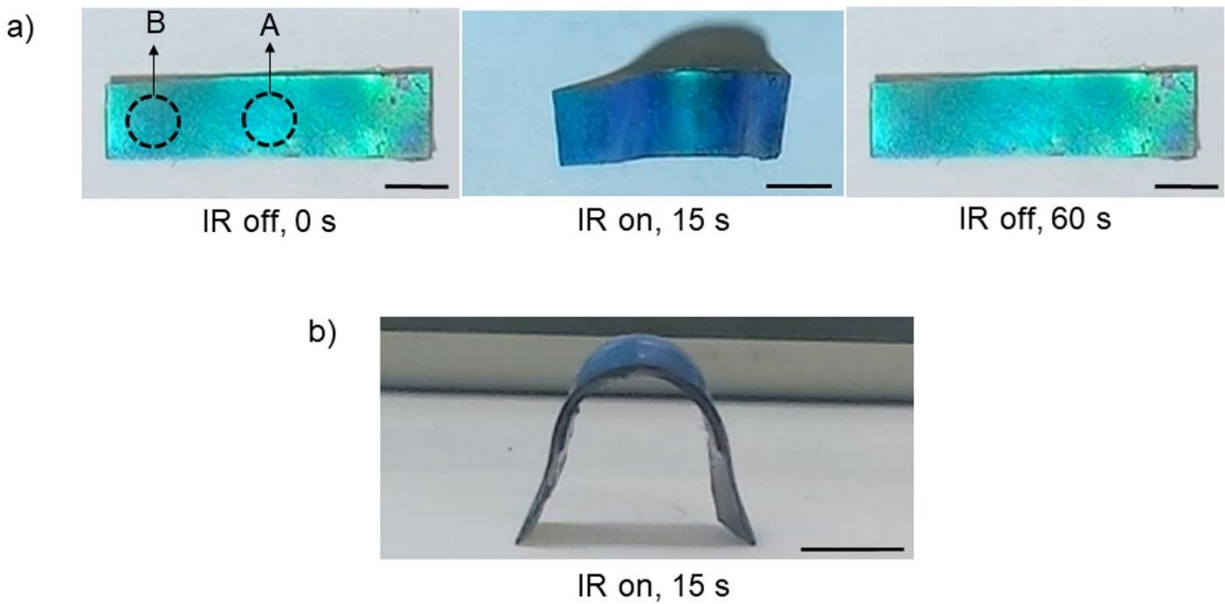


Figure 2.11. (a) Photographs (top view) of reversible bending and unbending of the laminated film in response to global IR irradiation. **(b)** Photograph (side view) of bent laminated film upon global IR irradiation. Scale bar: 5 mm.

In the LCE nanocomposite, the IR-active fillers can efficiently absorb and transform IR light into thermal energy, thereby serving as nanoscale heaters uniformly embedded in the LCE matrix. The absorbed thermal energy, if sufficient, leads to a shape change of the nanocomposite film. As shown in Figure 2.12, the temperature of the laminated film reaches about 70 °C soon after the IR light is turned on, which is well above the N-I phase transition temperature of the SWNT-LCE layer (~ 64.6 °C).

The maximum temperature of the LCE layer can be tuned by adjusting the loading level of SWNTs or IR light intensity.^{62,63} SWNTs, due to their high thermal conductivity, can serve as nanoscale heaters to increase the temperature of the LCE matrix uniformly and rapidly. In our previous work, we reported that SWNTs can form a percolation network in a polymer matrix at loading levels of 0.05-0.1 wt% SWNT.⁷¹ The absorbed thermal energy then induces the LCE N-I phase transition and the shape change in the nanocomposite film.

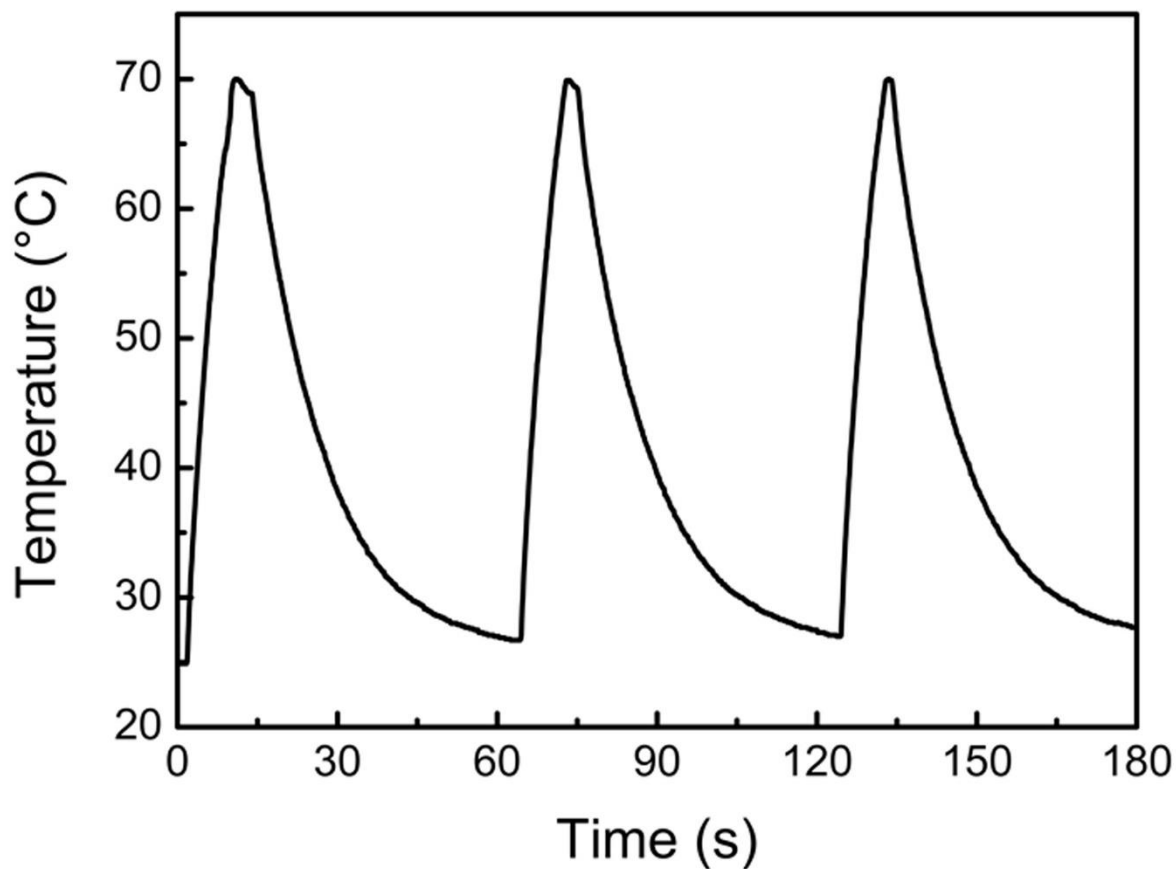
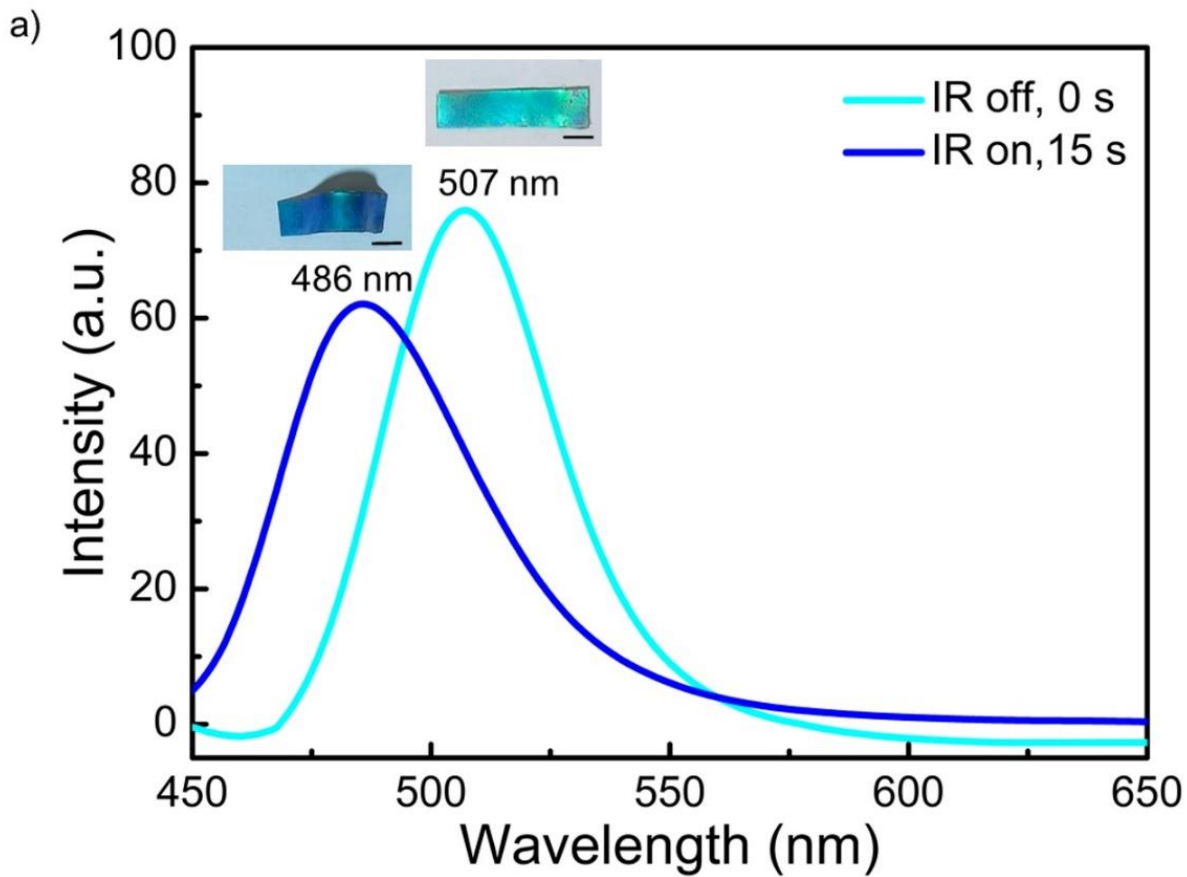


Figure 2.12. Temperature of the laminated film as a function of on and off cycles of global IR irradiation.

The observed color change of the laminated film is due to a combination of a decrease in lattice constant d of the elastomeric photonic crystal layer in the highly deformed region, represented by encircled area A, and a change of viewing angle θ in the less deformed regions, represented by encircled area B (Figure 2.11).

Upon IR-induced bending of the laminated film, the photonic bandgap of highly deformed area A of the mechanochromic layer undergoes a blueshift from 507 nm to 486 nm ($\theta = 90^\circ$) due to a decrease of d in the vertical direction, while the reflectance intensity in the same area only decreases slightly (Figure 2.13a). In contrast, the photonic bandgap

of area B remains unchanged at 504 nm ($\theta = 90^\circ$) upon IR irradiation (Figure 2.13b). Since the laminated film is elastomeric by nature, it can rapidly revert to its original shape and color upon turning off the IR light (Figure 2.14).



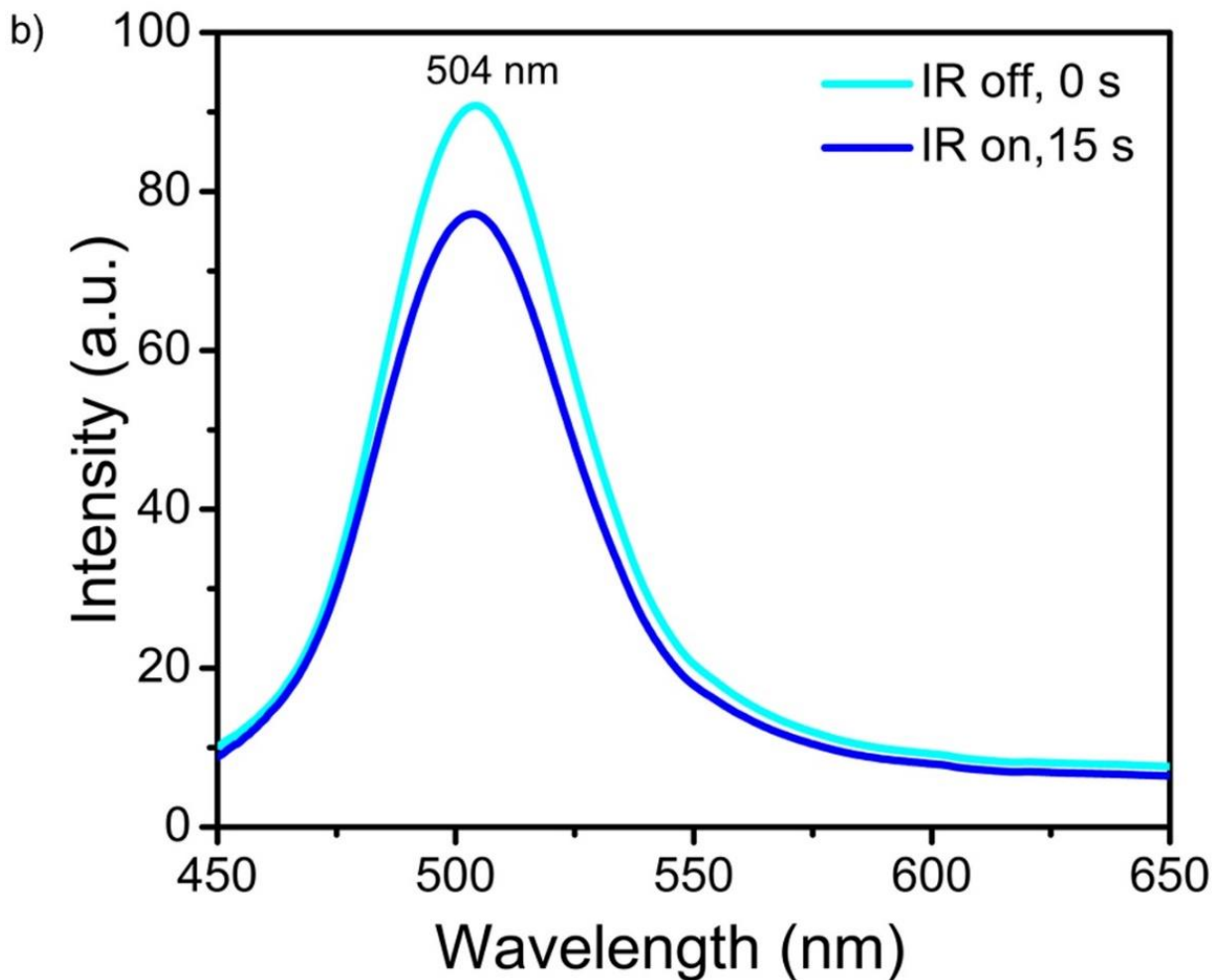


Figure 2.13. (a) Reflection spectra ($\theta = 90^\circ$) of the highly deformed region of the laminated film, represented by the encircled area A in Figure 2.11a, before and upon global IR irradiation, respectively. Inset images are corresponding photographs. **(b)** Reflection spectra ($\theta = 90^\circ$) of the less deformed region of the laminated film, represented by the encircled area B in Figure 2.11a, before and upon global IR irradiation, respectively. Scale bar: 5 mm.

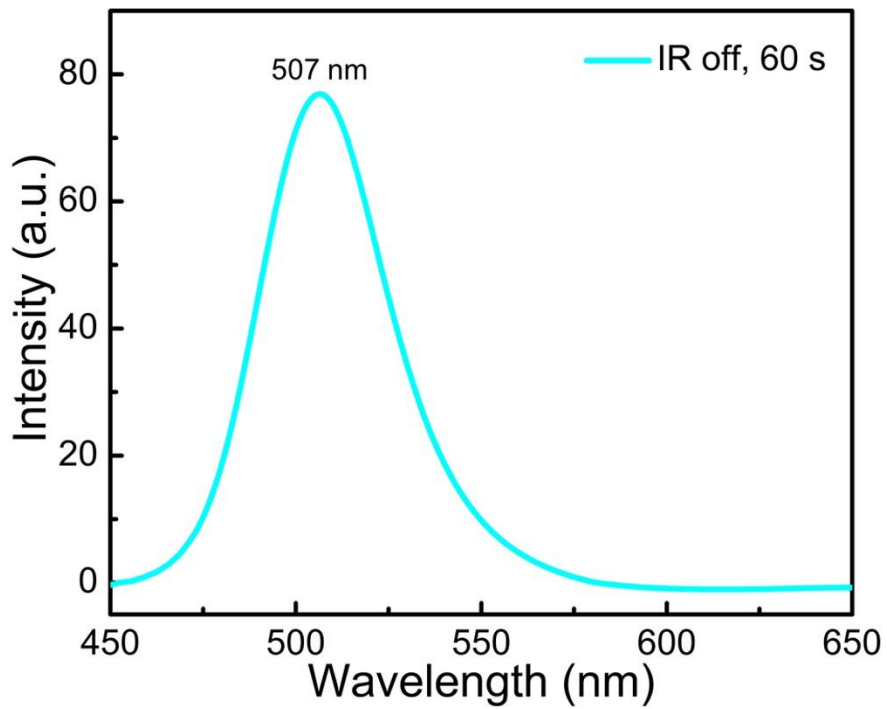
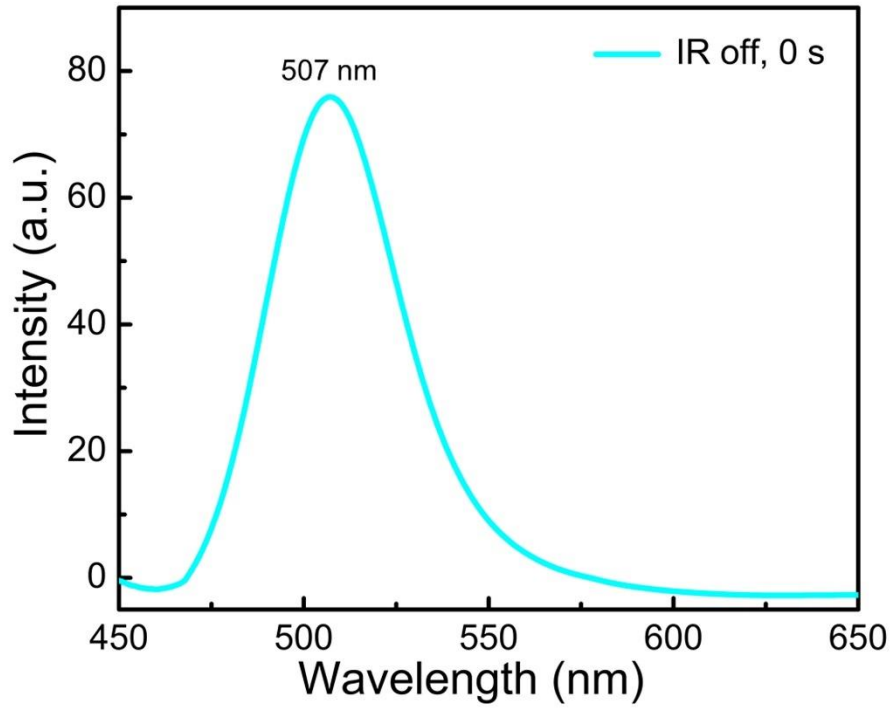


Figure 2.14. Reflection spectra ($\theta = 90^\circ$) of the unbent laminated film before (IR off, 0 s) and after (IR off, 60 s) global IR irradiation.

IR light-induced actuation brings together four important features: i) remote actuation through introducing IR-active fillers into the matrix; ii) wavelength selectivity which could enable precise and independent tuning of each individual active layer using a predetermined specific IR laser wavelength within a single system; iii) localized actuation, in contrast to global actuation, induced by IR light lasers owing to IR-active fillers; and iv) pattern generation through structured light systems, such as digital light processing (DLP) devices. Therefore, selective IR laser irradiation offers the localized actuation capability, which is particularly useful for generation of different patterns of surface color and morphology in the same laminated film.

To demonstrate the feasibility of localized bending actuation, the 808 nm IR laser was pointed to a selected region such as area A or B one at a time (Figure 2.15). The pattern of irradiation and no irradiation intervals was exactly the same as that for the IR actuation test shown in global irradiation. As a result of localized heating, the laminated film can exhibit coupled bending and color change at a desired region. Similar to global IR actuation (Figure 2.11), the photonic bandgap of highly deformed region in the laminated film undergoes a blueshift of 15-17 nm ($\theta = 90^\circ$) in localized IR actuation (Figure 2.16). These observations indicate that the laminated films have large, fast, and reversible response to IR stimuli, both global and localized irradiation.

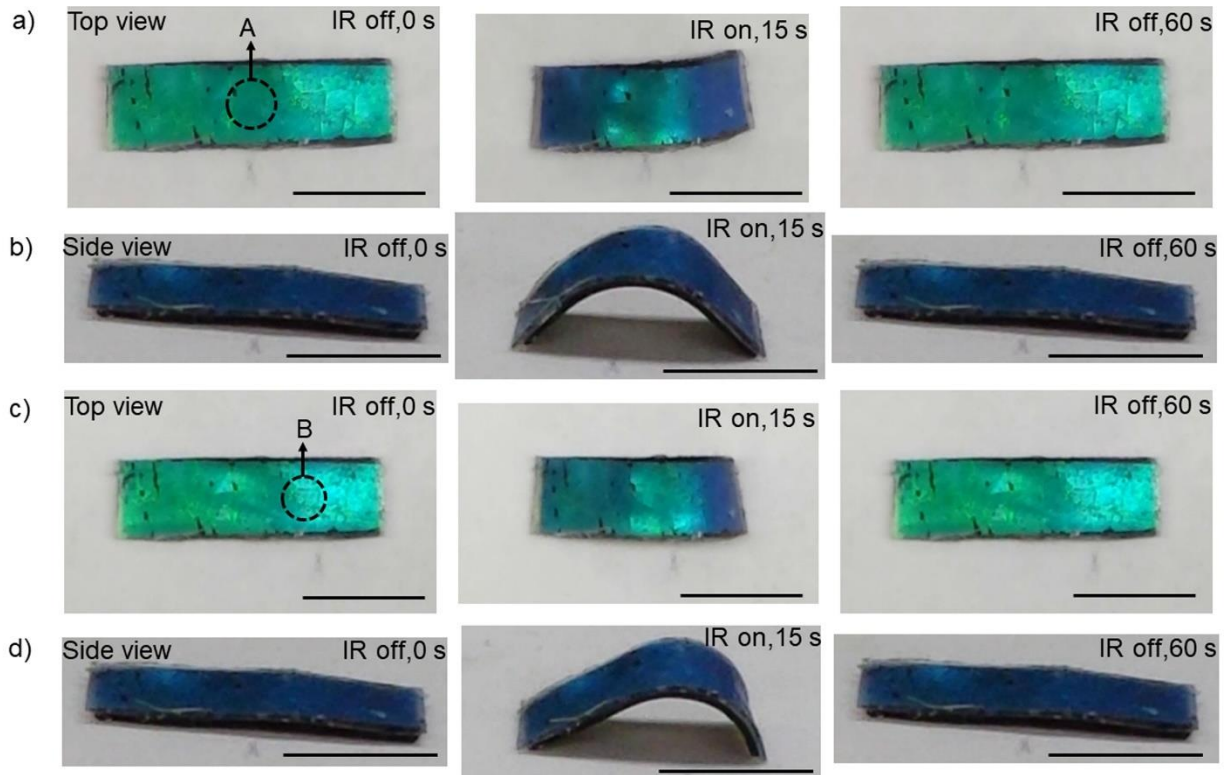


Figure 2.15. Photographs of localized IR actuation in the encircled area A of the laminated film at **(a)** top view and **(b)** side view, respectively. Photographs of localized IR actuation in the encircled area B of the laminated film at **(c)** top view and **(d)** side view, respectively. Scale bar: 5 mm.

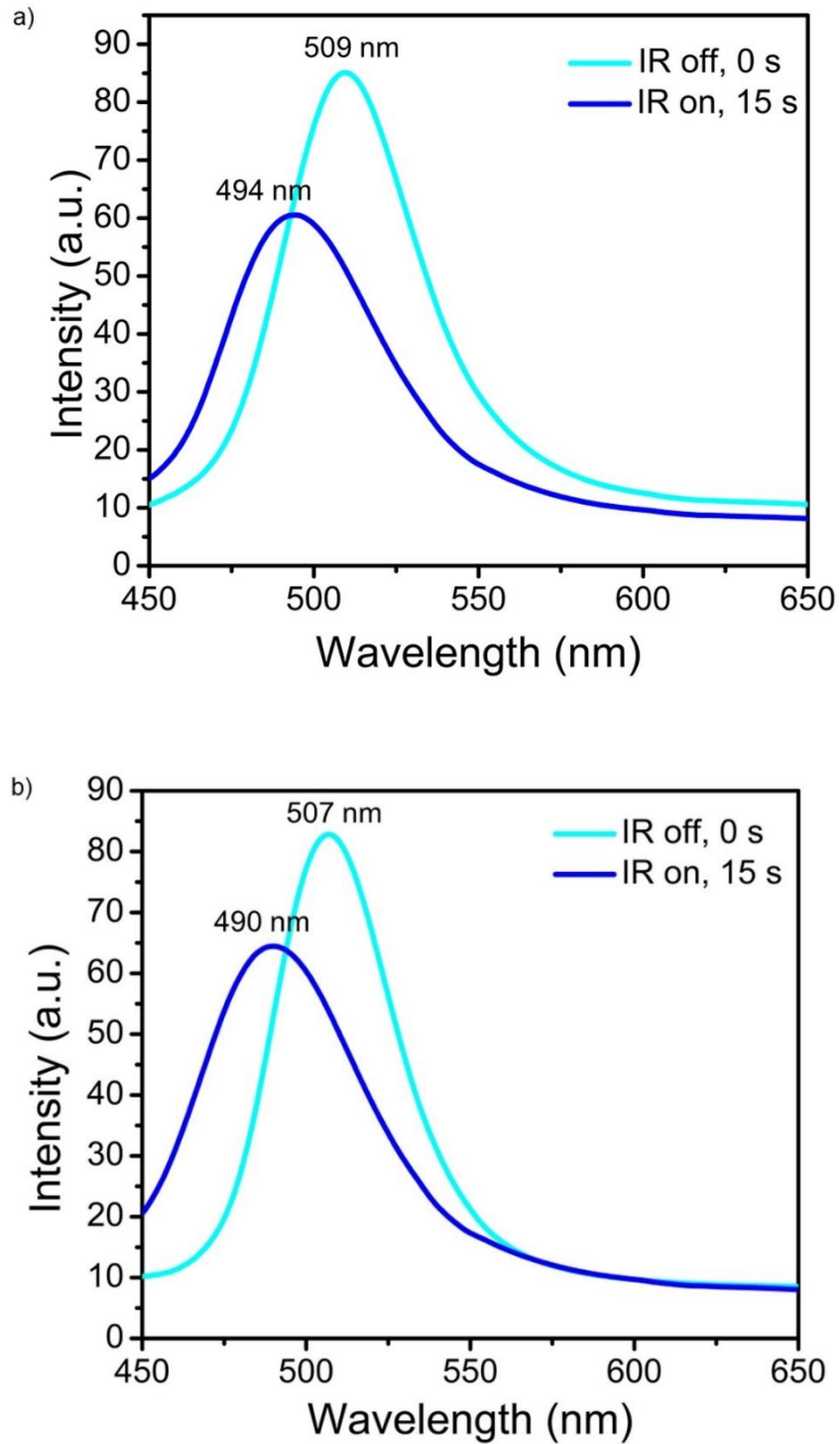


Figure 2.16. (a) Reflection spectra ($\theta = 90^\circ$) of the encircled area A (Figure 2.15a) of the laminated film before and upon localized IR irradiation, respectively. **(b)** Reflection spectra ($\theta = 90^\circ$) of the encircled area B (Figure 2.15c) of the laminated film before and upon localized IR irradiation, respectively.

In aforementioned laminated films, both the mesogenic units and IR-induced negative strain are oriented along the long axis of the SWNT-LCE film, which leads to bending actuation. In contrast, a twisted actuation can be achieved by cutting the SWNT-LCE nanocomposite film at 45° angle relative to the nematic director (i.e. the hot-drawing direction) (Figure 2.17a). In response to global IR irradiation, the generated negative strain is 45° relative to the long axis of the SWNT-LCE film, which produces the twisting deformation of the laminated film when its temperature reaches above the N-I phase transition temperature (Figure 2.17b).

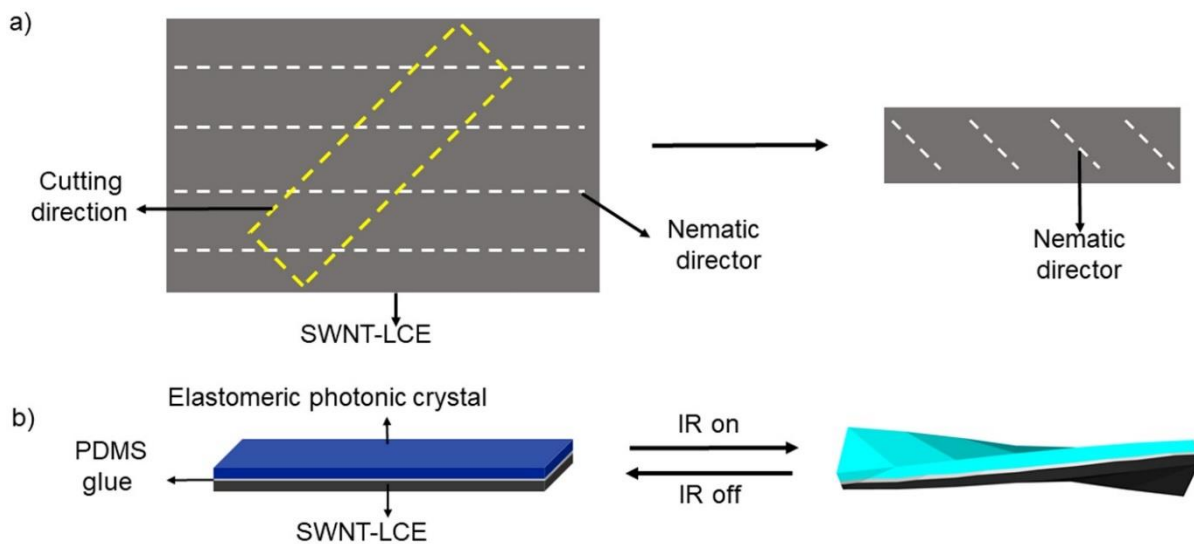


Figure 2.17. (a) Schematic illustration of the SWNT-LCE film subjected to a cutting angle of 45° relative to the nematic director. (b) Scheme of the laminated film undergoing twisting upon IR irradiation.

This twisting deformation causes a change in the side-view reflection color of the laminated film from blue to cyan, which is mainly attributed to the change of viewing angle (Figure 2.18a). As shown in Figure 2.18b, the photonic bandgap of area A remains unchanged at 510 nm ($\theta = 90^\circ$) upon global IR irradiation. Like the bending deformation, the twisted laminated film returns to its original shape upon turning off the IR light (Figure 2.18a).

To clearly show the twisted deformation behavior, both top-view and side-view photo images are recorded. The top view photographs of the laminated film before and upon twisting deformation are shown in Figure 2.19. These photographs demonstrate the color change upon twisting deformation, mainly due to the change of viewing angle originating from the twisting. Although, we demonstrated bending and twisting deformations in this study, other complex out-of-plane deformations can be created by simply altering the cutting angle of the SWNT-LCE films.

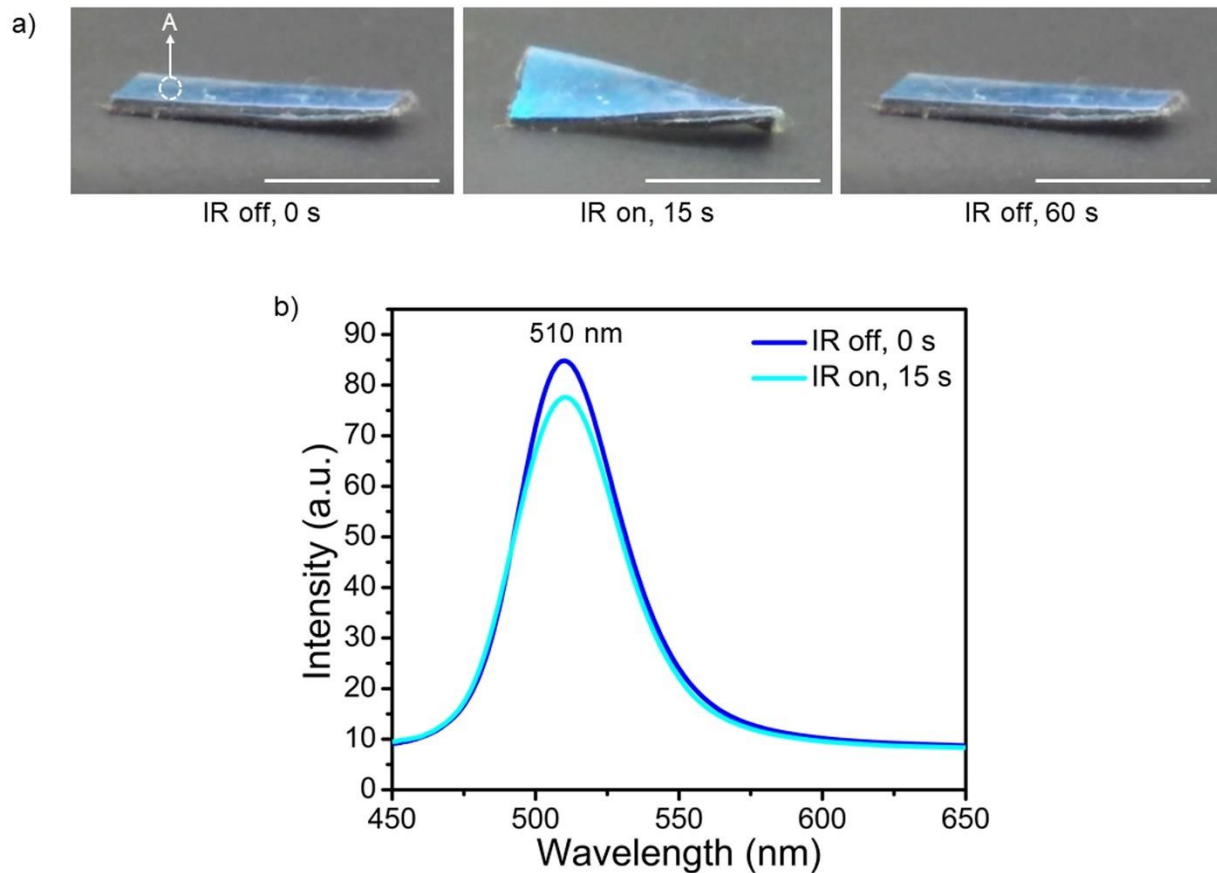


Figure 2.18. (a) Photographs (side view) of reversible twisting and untwisting of the laminated film in response to global IR irradiation. Scale bar: 5 mm. **(b)** Reflection spectra ($\theta = 90^\circ$) of the encircled area A (Figure 2.18a) of the laminated film before and upon global IR irradiation, respectively. In order to acquire the reflection spectra ($\theta = 90^\circ$) of the laminated film, the fiber optic probe is oriented perpendicular to the plane of the area A of the laminated film for both untwisted and twisted shapes.



Figure 2.19. Photographs (top view) of reversible twisting and untwisting of the laminated film in response to global IR irradiation. The top-view photographs are taken at the fixed angle that is perpendicular to the substrate. Scale bar: 5 mm.

Despite recent growing interests in bio-inspired soft robotics, soft robotic devices that can exhibit synergistic coupling of color change and out-of-plane deformation in motion are still very rare and require air pressure tubings.^{11,12} In this study, we show that the laminated film-based inchworm walkers are capable of IR-induced simultaneous reconfiguration of surface color and morphology during the movement.

As seen in Figure 2.20a, the laminated film moves on glass from left to right like an inchworm in response to on and off cycles of Torch NIR light. In the beginning of each actuation cycle (*i.e.*, IR is turned on), the front part of the film forms the stationary point on glass while the back part of the film slides forward. In the end of each actuation cycle (*i.e.*, IR is turned off), the back part of the film forms the stationary point on glass while the front part of the film pushes forward. The directional inchworm-like movements of the laminated film are due to the asymmetric bending of the film under global IR irradiation, which is evident from close inspection of the side view image of the bent film (Figure 2.20b). The front part (Thickness: $\sim 290 \mu\text{m}$) of the laminated film is slightly thinner than

the back part (Thickness: $\sim 302 \mu\text{m}$). As a result, the front part of the film bends more than the back part upon global IR irradiation (Figure 2.20b). We have previously found that the bending curvature of a bilayer film decreases with increase in film thickness.⁶³ We have also discovered that the same laminated film changes the moving direction to the opposite when it is turned 180° horizontally along the long axis. This observation further confirms that the thinner end of the film always serves as the front moving end during the IR actuation cycles.

The friction between the laminated film and substrate is crucial for inchworm walker's movements. We have found that the same laminated film moves much faster with more constant speed on glass (0.036 mms^{-1}) than on paper (0.022 mms^{-1}) under same global IR actuation conditions. Since the paper substrate provides lower friction for the laminated film than the glass substrate, it is difficult for one end of the asymmetrically bent laminated film to form an effective stationary point on paper during some actuation cycles. Therefore, the moving speed of the laminated film on paper is considerably lower and fluctuating compared with that on glass, while the moving direction remains the same as on glass due to the formation of similar asymmetric bending upon global IR irradiation (Figure 2.20b). The walking velocity of the inchworm walker could be significantly enhanced by further optimization of the thicknesses at front and back parts of the laminated film, and friction between the film and substrate. The fact that the inchworm walker exhibits reversible and coupled reconfiguration of color and shape for repeated actuation cycles confirms the flexibility and durability of the laminated films, which are highly desirable for soft robotics applications. We have conducted over 60 IR actuation cycles for each laminated film and ~ 250 IR actuation cycles for all laminated films in total,

and we have never observed any delamination of the laminated films during these experiments.

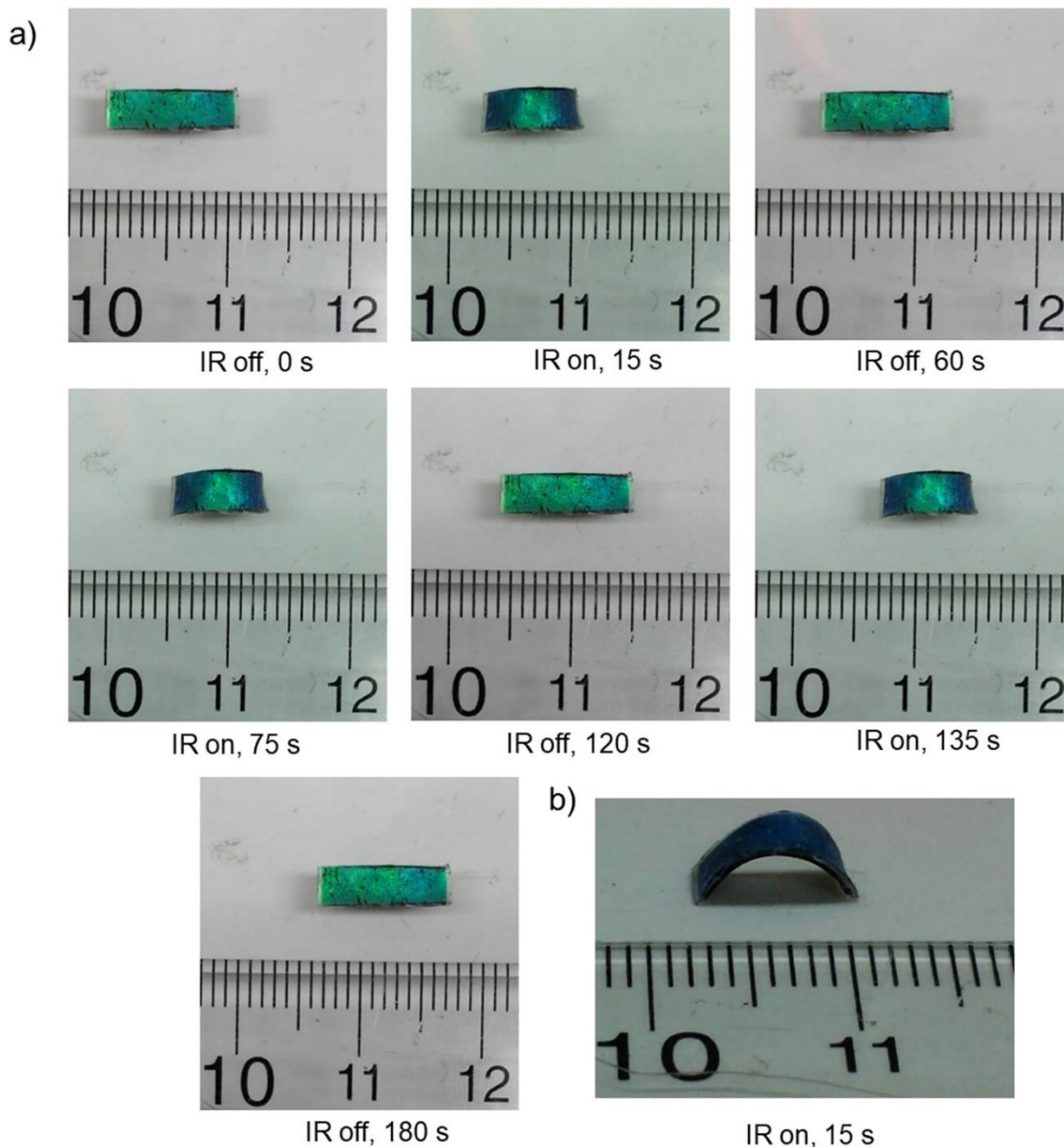


Figure 2.20. (a) Photographs (top view) of the laminated film-based inchworm walker movements on glass in response to on and off cycles of global IR irradiation. **(b)** Photograph (side view) of the laminated film-based inchworm walker movement from left to right on paper in response to global IR irradiation during the first on and off cycle.

How teams of multiple robots and multiple humans can interact and collaborate effectively represents a great challenge. Lessons from nature could help researchers to address such technical challenge. Mäthger and coworkers have recently illustrated how change of skin color and pattern plays a crucial role during cephalopods' intra- and interspecific behavioral interactions such as signaling and communication.³ For example, viewing angle-dependent iridescence provides swimming location and direction information of an individual squid, which may be used by squid to coordinate the movements of individuals of a school. Smart artificial skins such as the laminated films presented in this study offer a new communication approach, which is based on change of skin color, morphology, and pattern, for interactions and collaborations among teams of robots and humans. Direct recognition of image patterns, however, could be challenging in environments with low visibility conditions, or among teams of robots and humans who sometimes do not always see everyone else for various reasons. To address these limitations, we demonstrate the feasibility of converting image signals to audio signals, which provides an alternative way of interactions among robots and humans. In addition, audio-based communications may help humans/robots identify hidden patterns in their image data that are otherwise too delicate or fast to be recognized by vision. Furthermore, the audio files are more compact compared with image files, which allow for faster transmission and sharing of information.

The photo images of cyan unbent and blue bent films excluding backgrounds were first converted to sound waves using commercial software AudioPaint, which were then transformed into audio frequency spectra by fast Fourier transform (Figure 2.21). Most of sound frequencies are within the range of human hearing, which is 20 Hz to 20 kHz,

indicating the audibility of the generated sounds. Upon close inspection of audio spectra (Figure 2.21 b,d), we have noticed that the frequencies corresponding to the bent configuration are significantly different from those of the unbent configuration. Therefore, the differences in the observed frequencies of the generated sound waves can be utilized to differentiate between the relaxed and actuated configurations of the laminated film. Further selection and optimization of image-to-sound software could maximize the sound differences corresponding to different configurations of surface color and morphology.

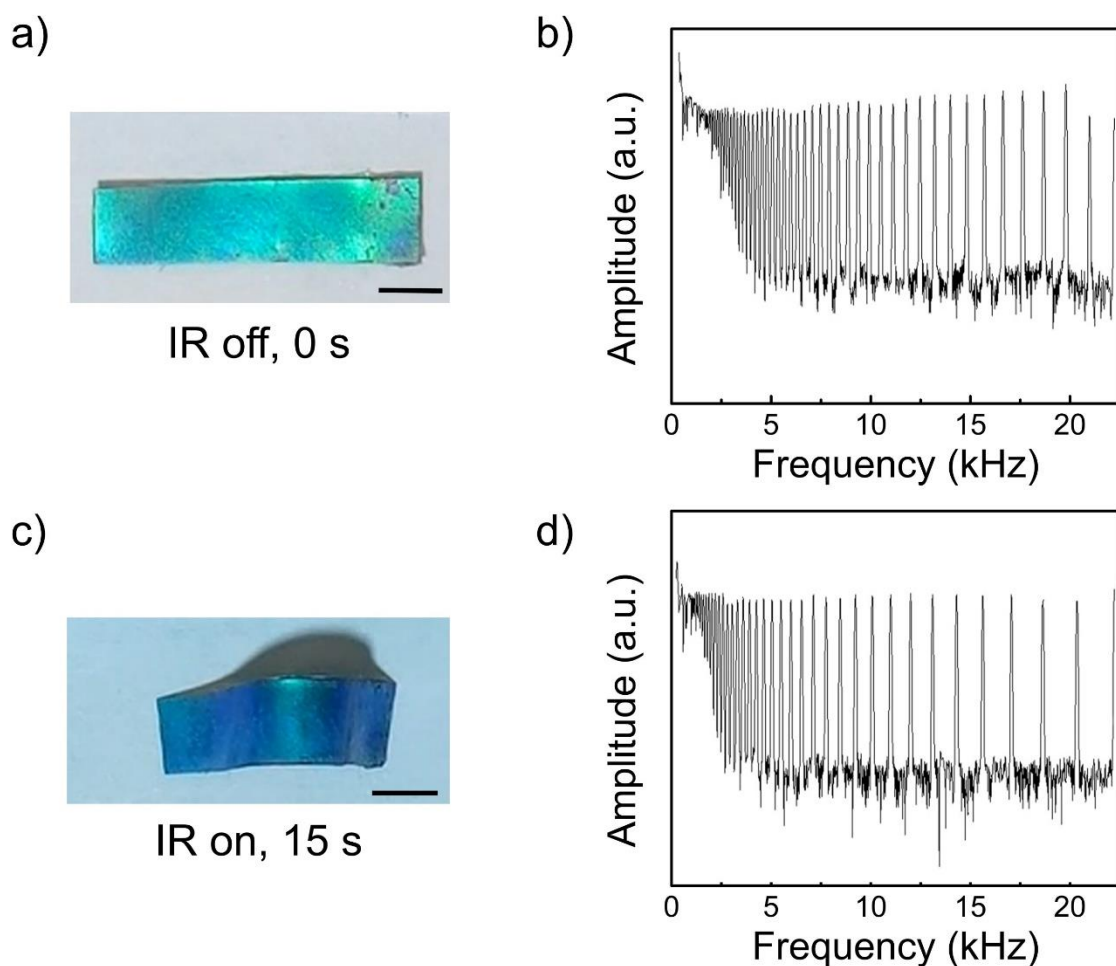


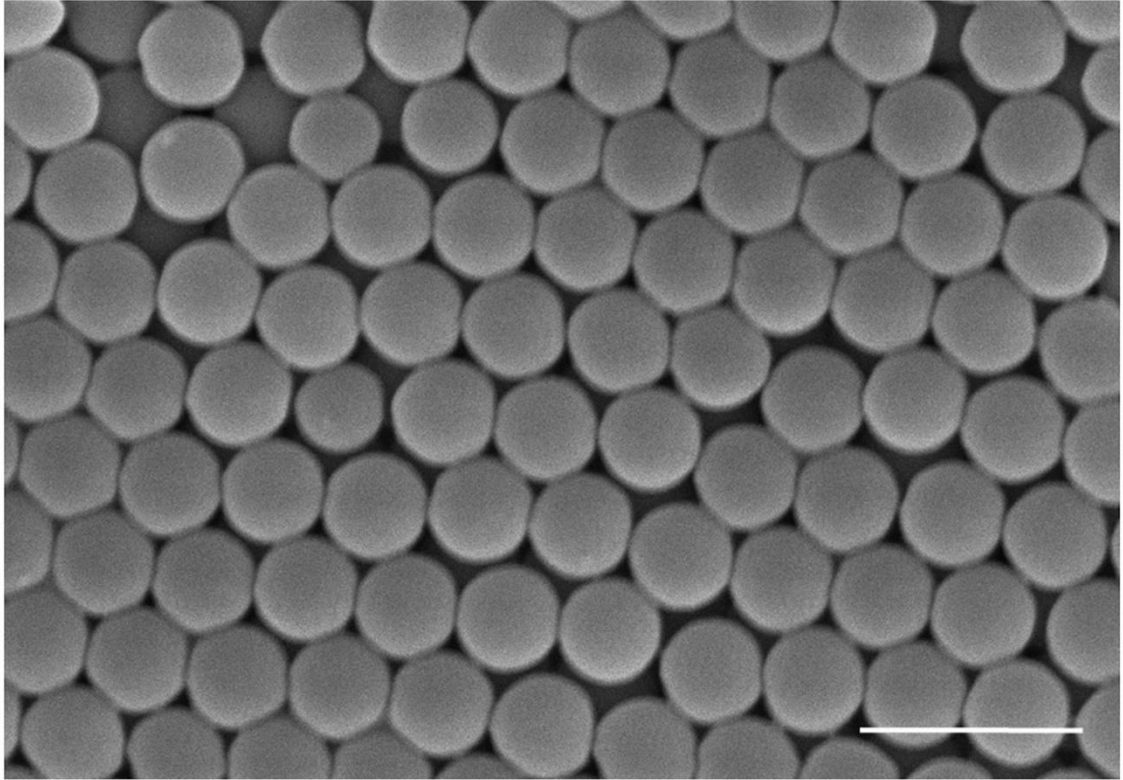
Figure 2.21. (a) Photograph and (b) audio frequency spectrum of cyan unbent laminated film. (c) Photograph and (d) audio frequency spectrum of blue bent laminated film upon global IR irradiation. Scale bar: 5 mm.

As mentioned earlier, one advantage of using the PDMS glue in our laminated structure is that it allows for the disassembly of the laminated film with appropriate tools. This feature enables us to reconfigure the laminated films by, for example, recoupling the SWNT-LCE film with another elastomeric photonic crystal film that has a different color. The color of elastomeric photonic crystal films can be readily tuned by controlling a number of parameters such as the size of the nanospheres, refractive index contrast between the nanospheres and the surrounding medium, and lattice constant. Although we chose elastomeric photonic crystal films with cyan color in this report, our approach can be easily extended to elastomeric films having a different color.

To prepare elastomeric photonic crystal films having red color, crosslinked PS nanospheres with larger diameter have been synthesized. As mentioned earlier, one way to control the diameter of nanospheres in emulsion polymerization is to adjust the concentration of emulsifier. As the amount of emulsifier decreases, the size of crosslinked PS nanospheres tends to increase due to a decreased number of primary nuclei formed in the early stage of polymerization.

The D_n and C_v of newly synthesized crosslinked PS nanospheres are approximately 236 nm and 3.8%, respectively. The C_v had a slight increase with decreasing the amount of emulsifier. The 236 nm nanospheres were highly monodisperse and formed close-packed photonic crystal assembly (Figure 2.22a), which has a bright green structural color under normal light incidence (Figure 2.22b).

a)



b)

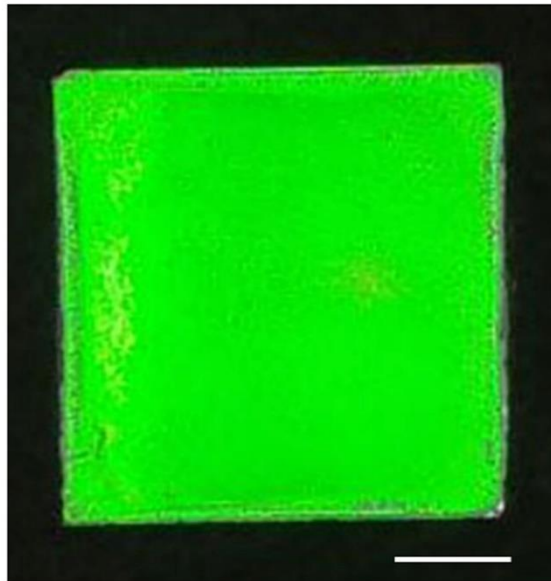


Figure 2.22. (a) SEM image of crosslinked PS nanospheres with diameter ~ 236 nm. Scale bar: 500 nm, and (b) photograph of the self-assembled photonic crystal film. Scale bar: 1 cm.

Similar to the previous elastomeric photonic crystal film with cyan color, the self-assembled film of crosslinked PS nanospheres with diameter of 236 nm was infiltrated with diluted PDMS precursors followed by curing. The PDMS infiltration results in a change in the structural color of the film from green to red. Similar to other 3D photonic crystal films, our elastomeric photonic crystal film displays the iridescent color that varies with the viewing angle. The top view, and side view photographs of the elastomeric photonic crystal film are shown in Figure 2.23a and 2.23b, respectively.

As shown in Figure 2.23c, the photonic bandgap corresponding to (111)-crystalline planes exhibits a Bragg reflection peak at $\lambda = 548$ nm, which was in reasonable agreement with the calculated peak wavelength of 555 nm for 236 nm nanospheres in a face-centered cubic structure using Equation 2.1. Reflection spectrum in Figure 2.23d shows that the PDMS infiltration results in a redshift in the photonic bandgap from 548 nm to 617 nm, which is mainly due to an increase in the lattice constant d .

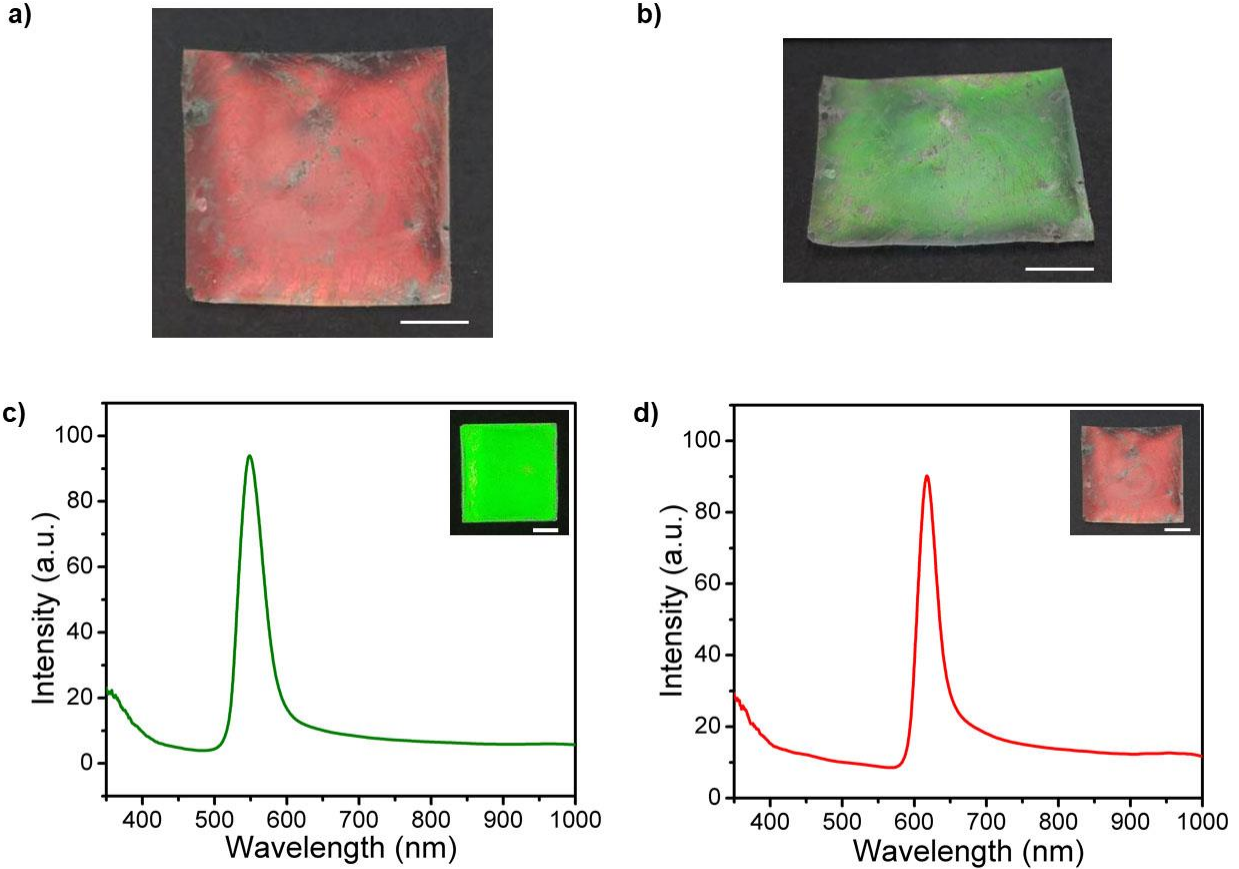


Figure 2.23. Photographs of (a) top view and (b) side view of the elastomeric photonic crystal film comprising crosslinked PS nanospheres with diameter of 236 nm embedded in PDMS matrix. Reflection spectra ($\theta = 90^\circ$) of (c) self-assembled photonic crystal film and (d) elastomeric photonic crystal film, respectively. Inset images are the corresponding photographs. Scale bar: 1 cm.

2.4. Conclusion

In conclusion, we have demonstrated the first remote-controlled soft robot that exhibits coupled sensing and actuation. In this study, we have developed a bio-inspired general approach to remote-controlled, smart films that undergo simultaneous changes of surface color and morphology upon IR actuation. Our approach is based on a laminated structure that directly couples an IR-responsive nanocomposite actuator layer with a

mechanochromic elastomeric photonic crystal layer. The facile disassembly of the laminated films with appropriate tools not only allows for full recovery of actuator and mechanochromic films, but also enables the reconfiguration of laminated films by reassembly of different layers.

Upon global or localized IR irradiation, the actuator layer displays fast, large, and reversible strain in the irradiated region, which causes a synergistically coupled change in the shape of the laminated film and color of the mechanochromic layer in the same region. Out-of-plane deformations, such as bending and twisting, can be induced under IR irradiation, via modulating the strain direction in the actuator layer of the laminated film. We have shown that the laminated films can be incorporated into soft robotic devices such as inchworm walkers, which are capable of remote-controlled coupled reconfiguration of surface color and morphology during the movement. The flexibility and durability of the laminated films are essential for repeated IR actuation cycles that enable soft robotic motion. We have also demonstrated the feasibility of converting image signals of the laminated film in motion into corresponding distinct audio signals, which could lead to audio-based interactions and collaborations among teams of robots and humans.

Although we have focused on using SWNT-LCE nanocomposites as IR-responsive actuators and elastomeric photonic crystals as mechanochromic materials in this study, our approach can be easily extended to other types of IR-absorbing fillers, thermo-responsive shape-changing polymers, and mechanochromic elastomers. Such IR-actuated, reconfigurable films could enable new functions in soft robots and wearable devices.

2.5. References

- (1) Hanlon, R. *Curr. Biol.* **2007**, 17, R400-R404.
- (2) Kreit, E; Mäthger, L. M.; Hanlon, R. T.; Dennis, P. B.; Naik, R. R.; Forsythe, E.; Heikenfeld, J. *J. R. Soc. Interface* **2013**, 10, 20120601.
- (3) Mäthger, L. M.; Denton, E. J.; Marshall, N. J.; Hanlon, R. T. *J. R. Soc. Interface* **2009**, 6, S149-S163.
- (4) Deravi, L. F.; Magyar, A. P.; Sheehy, S. P.; Bell, G. R. R.; Mäthger, L. M.; Senft, S. L.; Wardill, T. J.; Lane, W. S.; Kuzirian, A. M.; Hanlon, R. T.; Hu E. L.; Parker, K. K. *J. R. Soc. Interface* **2014**, 11, 20130942.
- (5) Allen, J. J.; Bell, G. R. R.; Kuzirian, A. M.; Hanlon, R. T. *J. Morphol.* **2013**, 274, 645-656.
- (6) Morin, S. A.; Shepherd, R. F.; Kwok, S. W.; Stokes, A. A.; Nemiroski, A.; Whitesides, G. M. *Science* **2012**, 337, 828-832.
- (7) Yu, C.; Li, Y.; Zhang, X.; Huang, X.; Malyarchuk, V.; Wang, S.; Shi, Y.; Gao, L.; Su, Y.; Zhang, Y.; Xu, H.; Hanlon, R. T.; Huang, Y.; Rogers, J. A. *Proc. Natl. Acad. Sci. USA* **2014**, 111, 12998-13003.
- (8) Wang, Q.; Gossweiler, G. R.; Craig, S. L.; Zhao, X. *Nat. Commun.* **2014**, 5, 4899.
- (9) Chou, H. H.; Nguyen, A.; Chortos, A.; To, J. W. F.; Lu, C.; Mei, J.; Kurosawa, T.; Bae, W. G.; Tok, J. B. H.; Bao, Z. A. *Nat. Commun.* **2015**, 6, 8011.
- (10) Chen, Z.; Li, S.; Arkebauer, A.; Gogos, G.; Tan, L. *ACS Appl. Mater. Interfaces* **2015**, 7, 10125-10131.
- (11) Gossweiler, G. R.; Brown, C. L.; Hewage, G. B.; Sapiro-Gheiler, E.; Trautman, W. J.; Welshofer, G. W.; Craig, S. L. *ACS Appl. Mater. Interfaces* **2015**, 7, 22431-22435.
- (12) Larson, C.; Peele, B.; Li, S.; Robinson, S.; Totaro, M.; Beccai, L.; Mazzolai, B.; Shepherd, R. *Science* **2016**, 351, 1071-1074.
- (13) Phan, L.; Kautz, R.; Leung, E. M.; Naughton, K. L.; Van Dyke, Y.; Gorodetsky, A. A. *Chem. Mater.* **2016**, 28, 6804-6816.
- (14) Zeng, S.; Zhang, D.; Huang, W.; Wang, Z.; Freire, S. G.; Yu X.; Smith, A. T.; Huang, E. Y.; Nguon, H.; Sun, L. *Nat. Commun.* **2016**, 7, 11802.
- (15) Chortos, A.; Liu, J.; Bao, Z. *Nature Mater.* **2016**, 15, 937-950.

- (16) Kim, S.; Laschi, C.; Trimmer, B. *Trends Biotechnol.* **2013**, 31, 287-294.
- (17) Rus, D.; Tolley, M. T. *Nature* **2015**, 521, 467-475.
- (18) Rogers, J. A.; Someya, T.; Huang, Y. *Science* **2010**, 327, 1603-1607.
- (19) Someya, T.; Bao, Z.; Malliaras, G. G. *Nature* **2016**, 540, 379-385.
- (20) Zhao, Y.; Xie, Z.; Gu, H.; Zhu, C.; Gu, Z. *Chem. Soc. Rev.* **2012**, 41, 3297-3317.
- (21) Sun, J.; Bhushan, B.; Tonga, J. *RSC Adv.* **2013**, 3, 14862-14889.
- (22) Fu, Y.; Tippetts, C. A.; Donev, E. U.; Lopez, R. *WIREs Nanomed. Nanobiotechnol* **2016**, 8, 758-775.
- (23) Ge, J.; Yin, Y. *Angew. Chem. Int. Ed.* **2011**, 50, 1492-1522.
- (24) Burgess, I. B.; Loncar, M.; Aizenberg, J. *J. Mater. Chem. C* **2013**, 1, 6075-6086.
- (25) Chan, E. P.; Walish, J. J.; Urbas, A. M.; Thomas, E. L. *Adv. Mater.* **2013**, 25, 3934-3947.
- (26) Nucara, L.; Greco, F.; Mattoli, V. *J. Mater. Chem. C* **2015**, 3, 8449-8467.
- (27) Holtz, J. H.; Asher, S. A. *Nature* **1997**, 389, 829-832.
- (28) Fudouzi, H.; Xia, Y. *Langmuir* **2003**, 19, 9653-9660.
- (29) Fudouzi, H.; Sawada, T. *Langmuir* **2006**, 22, 1365-1368.
- (30) Viel, B.; Ruhl, T.; Hellmann, G. P. *Chem. Mater.* **2007**, 19, 5673-5679.
- (31) Arsenault, A. C.; Puzzo, D. P.; Manners, I.; Ozin, G. A. *Nat. Photonics* **2007**, 1, 468-472.

- (32) Jiang, Y.; Xu, D.; Li, X.; Lin, C.; Li, W.; An, Q.; Tao, C. -A.; Tang, H.; Li, G. *J. Mater. Chem.* **2012**, 22, 11943-11949.
- (33) Schäfer, C. G.; Viel, B.; Hellmann, G. P.; Rehahn, M.; Gallei, M. *ACS Appl. Mater. Interfaces* **2013**, 5, 10623-10632.
- (34) Schäfer, C. G.; Gallei, M.; Zahn, J. T.; Engelhardt, J.; Hellmann, G. P.; Rehahn, M. *Chem. Mater.* **2013**, 25, 2309-2318.
- (35) Schäfer, C. G.; Smolin, D. A.; Hellmann, G. P.; Gallei, M. *Langmuir* **2013**, 29, 11275-11283.
- (36) Ito, T.; Katsura, C.; Sugimoto, H.; Nakanishi, E.; Inomata, K. *Langmuir* **2013**, 29, 13951-13957.
- (37) Scheid, D.; Lederle, C.; Vowinkel, S.; Schäfer, C. G.; Stühn, B.; Gallei, M. *J. Mater. Chem. C* **2014**, 2, 2583-2590.
- (38) Schäfer, C. G.; Lederle, C.; Zentel, K.; Stühn, B.; Gallei, M. *Macromol. Rapid Commun.* **2014**, 35, 1852-1860.
- (39) Cho, Y.; Lee, S. Y.; Ellerthorpe, L.; Feng, G.; Lin, G.; Wu, G.; Yin, J.; Yang, S. *Adv. Funct. Mater.* **2015**, 25, 6041-6049.
- (40) Lin, C.; Jiang, Y.; Tao, C. -A.; Yin, X.; Lan, Y.; Wang, C.; Wang, S.; Liu, X.; Li, G. *ACS Appl. Mater. Interfaces* **2017**, 9, 11770-11779.
- (41) Behl, M.; Zotzmann, J.; Lendlein, A. *Adv. Polym. Sci.* **2010**, 226, 1-40.
- (42) Oliver, K.; Seddon, A.; Trask, R. S. *J. Mater. Sci.* **2016**, 51, 10663-10689.
- (43) Han, D. -D.; Zhang, Y. -L.; Ma, J. -N.; Liu, Y. -Q.; Han, B.; Sun, H. -B. *Adv. Mater.* **2016**, 28, 8328-8343.
- (44) Hu, Y.; Li, Z.; Lan, T.; Chen, W. *Adv. Mater.* **2016**, 28, 10548-10556.
- (45) Finkelmann, H.; Kock, H. J.; Rehage, G. *Makromol. Chem. Rapid Commun.* **1981**, 2, 317-322.
- (46) Assfalg, N.; Finkelmann, H. *KGK, Kautsch. Gummi Kunstst.* **1999**, 52, 677-680.
- (47) Warner, M.; Terentjev, E. M. *Liquid Crystal Elastomers*, Oxford University Press, Oxford, **2007**.
- (48) Ikeda, T.; Mamiya, J.; Yu, Y. *Angew. Chem. Int. Ed.* **2007**, 46, 506-528.

- (49) Ohm, C.; Brehmer, M.; Zentel, R. *Adv. Mater.* **2010**, 22, 3366-3387.
- (50) Jiang, H.; Li, C.; Huang, X. *Nanoscale* **2013**, 5, 5225-5240.
- (51) Fleischmann, E. -K.; Zentel, R. *Angew. Chem. Int. Ed.* **2013**, 52, 8810-8827.
- (52) Ube, T.; Ikeda, T. *Angew. Chem. Int. Ed.* **2014**, 53, 10290-10299.
- (53) White, T. J.; Broer, D. J. *Nat. Mater.* **2015**, 14, 1087-1098.
- (54) Bisoyi, H. K.; Li, Q. *Chem. Rev.* **2016**, 116, 15089-15166.
- (55) Kularatne, R. S.; Kim, H.; Boothby, J. M.; Ware, T. H. *J. Polym. Sci. Part B: Polym. Phys.* **2017**, 55, 395-411.
- (56) Sawa, Y.; Ye, F.; Urayama, K.; Takigawa, T.; Gimenez-Pinto, V.; Selinger, R. L.; Selinger, J. V. *Proc. Natl. Acad. Sci. USA* **2011**, 108, 6364-6368.
- (57) Liu, L.; Geng, B.; Sayed, S. M.; Lin, B. -P.; Keller, P.; Zhang, X. -Q.; Sun, Y.; Yang, H. *Chem. Commun.* **2017**, 53, 1844-1847.
- (58) Ahir, S. V.; Terentjev, E. M.; Lu, S. X.; Panchapakesan, B. *Phys. Rev. B* **2007**, 76, 165437.
- (59) Lu, S. X.; Ahir, S. V.; Terentjev, E. M.; Panchapakesan, B. *Appl. Phys. Lett.* **2007**, 91, 103106.
- (60) Hamon, M. A.; Itkis, M. E.; Niyogi, S.; Alvaraez, T.; Kuper, C.; Menon, M.; Haddon, R. C. *J. Am. Chem. Soc.* **2001**, 123, 11292.
- (61) Kohlmeyer, R. R.; Lor, M.; Chen, J. *Nano Lett.* **2012**, 12, 2757-2762.
- (62) Yang, L.; Setyowati, K.; Li, A.; Gong, S.; Chen, J. *Adv. Mater.* **2008**, 20, 2271-2275.
- (63) Kohlmeyer, R. R.; Chen, J. *Angew. Chem. Int. Ed.* **2013**, 52, 9234-9237.
- (64) Chen, J.; Liu, H.; Weimer, W. A.; Halls, M. D.; Waldeck, D. H.; Walker, G. C. *J. Am. Chem. Soc.* **2002**, 124, 9034-9035.

- (65) Chen, J.; Ramasubramaniam, R.; Xue, C.; Liu, H. *Adv. Funct. Mater.* **2006**, 16, 114-119.
- (66) Thomsen III, D. L.; Keller, P.; Naciri, J.; Pink, R.; Jeon, H.; Shenoy, D.; Ratna, B. R. *Macromolecules* **2001**, 34, 5868-5875.
- (67) Tang, B.; Zheng, X.; Lin, T.; Zhang, S. *Dyes and Pigments* **2014**, 104, 146-150.
- (68) Nagao, D.; Anzai, N.; Kobayashi, Y.; Gu, S.; Konno, M. *J. Colloid Interface Sci.* **2006**, 298, 232-237.
- (69) Fudouzi, H. *J. Colloid Interf. Sci.* **2004**, 275, 277-283.
- (70) Fudouzi, H. *Colloids and Surfaces A: Physicochem. Eng. Aspects* **2007**, 311, 11-15.
- (71) Ramasubramaniam, R.; Chen, J.; Liu, H. *Appl. Phys. Lett.* **2003**, 83, 2928-2930.
- (72) Odian, G. *Principles of Polymerization*, Wiley, Hoboken, NJ, USA, **2004**.
- (73) Du, X.; He, J. *J. Appl. Polym. Sci.* **2008**, 108, 1755-1760.
- (74) Ko, Y. G.; Shin, D. H. *J. Phys. Chem. B* **2007**, 111, 1545-1551.

Chapter 3: Soft Films for Responsive Interference Coloration

3.1. Introduction

A crucial aspect of soft robotics is the ability of robots to sense their environments. In comparison with other sensing mechanisms, colorimetric sensing provides a simple yet powerful detection tool for development of low-power and low-cost sensors. The optical signal from a colorimetric sensor can be readily monitored by the naked eye without the need of complicated and expensive tools to read the outputs.

Recently, there has been a growing interest in utilizing structural colors to create stimuli-responsive color-changing materials.¹⁻⁴ As mentioned in Chapter 2, structural colors are produced by micro- or nano-structures, therefore they are non-fading colors in contrast to conventional chemical dyes. Structural colors can be found in species of birds, butterflies, insects, and marine organisms. Many natural species can tune their structural colors in response to their surroundings for camouflage, or signal communication. Inspired by the natural creatures, many photonic materials with structural colors have been developed. These materials have found applications ranging from switches and display devices to sensors.⁵⁻⁸ The structural color-based sensors are responsive to external stimuli such as solvents, vapors, heat, pH, biomolecules, and mechanical force.⁷⁻

19

Most of the structural colors found in nature are considered to stem from the following five fundamental optical processes and their combinations: i) thin-film

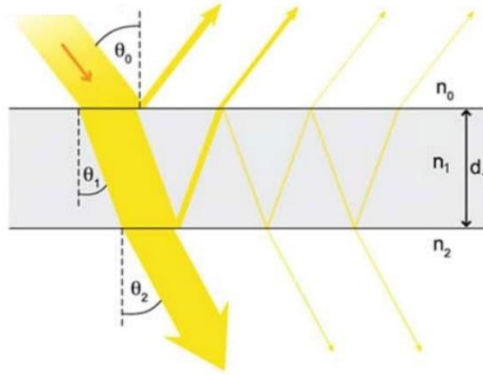
interference; ii) multilayer interference; iii) a diffraction grating effect; iv) photonic crystals; and v) light scattering.² There has been great interest in responsive photonic crystals due to their many potential applications.⁷⁻⁹ A major challenge is overcoming the problems of limited scalability and time-consuming fabrication process, which affect the real-world applications of the photonic crystals.^{20,21} It is therefore highly desirable to investigate new approaches that can transform these initial breakthroughs into real-world applications. Herein, we report a new scalable and affordable platform technology for fabrication of stimuli-responsive structural colored films. The coloration in our system is based on thin-film interference, the most common cause of structural color in nature.

Thin-film interference is one of the simplest structural colors, responsible for the colorful, iridescent reflections that can be seen in oil films on water, and soap bubbles.²²⁻²⁶ This optical process occurs in structures composed of one or more transparent thin films, whose typical thickness is comparable to the wavelength of light.²⁴ The reflectivity of a thin, non-absorbing layer of thickness d_1 with refractive index n_1 , bound by two semi-infinite media with refractive indices of n_0 and n_2 , can be determined by addition of the amplitudes of all the light beams which leave the thin layer in reflection, and those beams which might have been subjected to multiple reflections within the thin layer (scheme 3.1).^{2,4,24} The conditions for constructive interference of a thin film are determined by Equation 3.1:

$$m\lambda = 2n_1d_1 \cos\theta_1 \quad (3.1)$$

where λ is the wavelength giving the maximum reflectivity, m is a positive integer, d_1 is the thin-film thickness, n_1 is the refractive index of the thin film and θ_1 is the angle of

refraction.² Therefore, the interference colors depend on the refractive indices of the film and surrounding regions, the thin-film thickness, and the viewing angle.



Scheme 3.1. Physical mechanism of the thin-film interference.²

Most thin-film optical coatings have two important characteristics: i) they utilize low-loss dielectric materials; and ii) their film thicknesses are similar to the wavelength of light.²⁴ The quarter-wave thickness ($\lambda/4n$, where λ and n are maximum reflection wavelength and refractive index of the material, respectively) is often considered to be the thinnest useful interference coating. The optical losses in these dielectrics are usually small, and therefore the reflection and transmission phase changes at the interfaces between the dielectric films can be assumed to be either 0 or π depending on the refractive index contrast.^{4,24}

A well-known example of the thin-film coatings on metals is the metal anodization, an electrolytic method that forms a thin layer of metal oxide with controllable thickness on a metal substrate.²⁴ For instance, anodizing titanium forms a thin film of titanium oxide (a

transparent dielectric) on the surface of the titanium metal. By controlling the thickness of the titanium oxide layer, different interference colors will emerge.²⁷

Recently, Kats *et al.* presented a new technique based on thin-film interference in ultrathin, highly absorbing dielectrics on metals.^{28,29} A combination of a large absorption in the dielectric film and the non-trivial phase-shift at the interface between metal and dielectric allows the significant reduction of the film thickness. A non-trivial phase-shift is not limited to 0 or π as for transparent thin-films. The resulting strong absorption resonance generates various colors depending on the thickness of the film. However, these thin-film coatings lack sensing capabilities which renders them impractical for colorimetric sensing applications.

The materials used for thin-film interference colorations in the aforementioned studies, were based on inorganic materials (e.g. Ge, Si). Moreover, the coloration is not responsive to external stimuli and therefore lacks the sensing capability. A promising new strategy towards sensing function in thin-film optical coatings is to employ stimuli-responsive polymeric materials in their design that induce color change in response to environmental stimuli. However, this new strategy for thin-film interference coloration has not been explored so far in the literature.

Compared with most inorganic materials, polymers have many advantages such as flexibility, good processability, excellent corrosion resistance, light-weight, and biocompatibility. Moreover, a new class of polymers known as “smart materials” are able to sense their environment (e.g., humidity, temperature, chemicals, light or mechanical forces), and respond accordingly.^{30,31}

Here, we demonstrate a new platform technology for colorimetric sensing which is based on responsive interference coloration. Our system is composed of a thin film of a transparent polymer deposited on a metal-coated substrate. A full spectrum of bright interference colors can be generated on both rigid and soft substrates through a facile fabrication method. Moreover, our thin-film interference colors exhibit fast and reversible color changes upon variations in the environmental humidity. Such polymer-based, responsive interference coloration could empower colorimetric sensing of various environmental stimuli (*e.g.*, humidity, chemicals, heat, biomolecules, and mechanical forces), which could enable a wide range of applications.

Our responsive interference coloration has brought together several important features: i) scalable and affordable approach to generate polymer-based, responsive interference coloration on both rigid and soft substrates; ii) color-tunability by simply changing the thickness of the polymer layer; iii) fast, and reversible color-change in response to changes in humidity.

3.2. Experimental

3.2.1. Materials

Polyvinylpyrrolidone (PVP) powder was purchased from Alfa Aesar. Polycarbonate (PC) pellets was purchased from Sigma-Aldrich. PVP solutions in ethanol with PVP loadings from 6 to 9 wt%, and PC solutions in chloroform with PC loading of 2 wt% were

prepared. Ethanol (200 proof) was purchased from Koptec. Chloroform was acquired from Sigma-Aldrich.

Glass substrates (Micro Slides), were purchased from Corning. Glass microscopic slides were rinsed with acetone and isopropanol and then dried with nitrogen prior to use. PDMS precursors (Sylgard 184) were purchased from Dow Corning. PDMS films were fabricated based on the manufacturer's recommended base to crosslinker mix ratio of 10:1. Chemical structures of PVP, PC, and PDMS are shown in Figure 3.1.

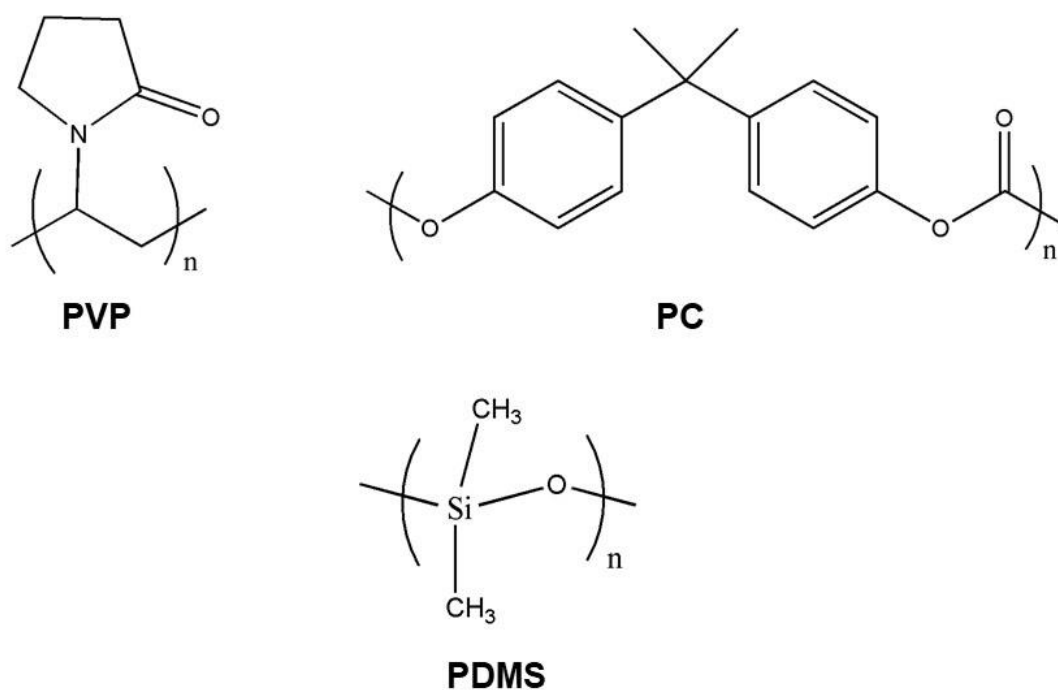


Figure 3.1. Chemical structures of PVP (polyvinylpyrrolidone), PC (polycarbonate), and PDMS (polydimethylsiloxane) used in fabrication of the thin-film interference coloration.

3.2.2. Preparation of Thin Films of Metal

The preparation procedure for thin-films of polymers deposited on metal-coated substrates is schematically illustrated in Figure 3.2. Very thin films of iridium are deposited on the substrates in a sputter coating system (model K150X, Quorum Emitech) using a high purity iridium target (Ted Pella, Inc.). The sputter's chamber pressure is first brought to $\sim 2 \times 10^{-3}$ mbar, then iridium deposition is performed under 2×10^{-3} mbar pressure with a constant Ar flow. 150 mA current is used for sputtering.

3.2.3. Preparation and Characterization of Thin Films of Polymer on Metal-Coated Substrates

Once the thin film of iridium has been deposited on the substrate using sputter coating, an appropriate amount of the polymer solution is placed on top of the iridium coated substrate and then spin-coated at a specific spinning speed (2500-8000 rpm) for 30 seconds using a spin coater (model P6700, Specialty Coating Systems, Inc.). Finally, the polymer film was baked in air at room temperature to evaporate residual solvent.

The generated thin-film interference coloration was characterized by scanning electron microscopy (SEM) and spectrophotometry. The reflection spectra were acquired using a fiber optic Vis-NIR spectrometer (USB2000, Ocean Optics). The absorption spectra were recorded with a Cary 5000 UV-Vis-NIR spectrophotometer. The average thickness of the thin-film was determined from SEM observations of 50 points of the thin-film to ensure the accuracy of measurements. SEM was performed using a Hitachi S-

4800 field emission scanning electron microscope at accelerating voltages of between 1 kV and 2 kV.

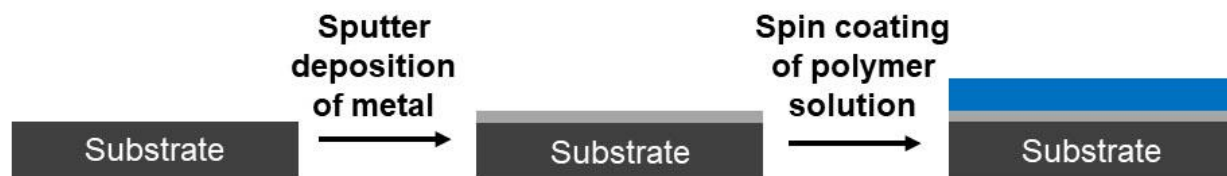


Figure 3.2. Schematic illustration of the preparation of the thin films of polymer on metal-coated substrates.

3.3. Results and Discussion

3.3.1. Metal Coating

In this study, iridium was chosen as the metal to be coated on the desired substrates, mainly due to its availability. The amount of iridium used for a 5 nm-thick coating is $11.3 \mu\text{g per cm}^2$, which results in material cost of around 0.04 € per cm^2 . Thin films of iridium were coated on the substrates using a sputter coating system. Film thickness monitor (FTM) quartz crystals are used to determine the thickness of the coated iridium and terminate the deposition at a pre-set thickness. The FTM controller operates by monitoring the frequency shift of an oscillating quartz crystal as iridium is deposited on the crystal. The frequency shift is related to the mass of the deposited iridium. The quartz crystal is placed in the vacuum chamber. One face of the crystal is exposed towards the iridium target, such that as iridium is deposited, it will coat the crystal. The system functions as an oscillator, whose output is controlled by the frequency of crystal

oscillation. As iridium is deposited on the crystal, so its frequency is modified, and this modification is used to determine the thickness of the deposited iridium.³²

The iridium-coated substrates are silvery-white and appear shiny as mirror (Figure 3.3 a, b). The reflection and absorption spectra of the iridium-coated glass substrates are shown in Figure 3.3c and 3.3d. It should be noted that although iridium was chosen as the metal mirror in this report, this approach can be easily extended to other metal mirrors with appropriate metal thickness.

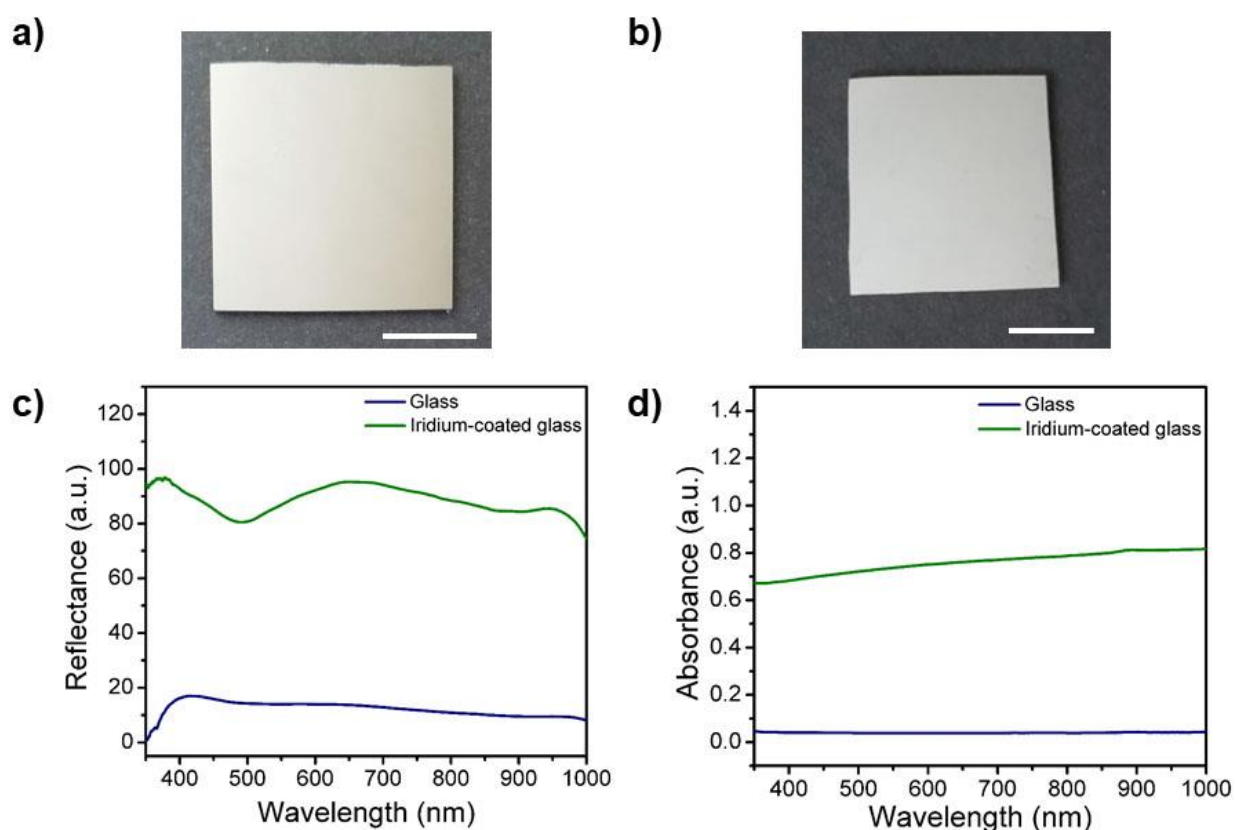


Figure 3.3. (a) Photograph of a glass substrate coated with a thin film of iridium (5 nm thick). (b) Photograph of a PDMS substrate (~750 μm thick) coated with a thin film of iridium (5 nm thick). (c) Reflection spectra of the glass substrate and iridium-coated glass, respectively. (d) Absorption spectra of the glass substrate and iridium-coated glass, respectively. Scale bar: 1 cm.

3.3.2. Polymer Deposition

Both PVP and PC are optically transparent polymers. As for the solubility, PVP can be readily dissolved in alcohols and water, and PC is soluble in chlorinated solvents. As described in the experimental section, small amounts of polymer solution were spin coated on the substrates at high speeds to form thin films of polymer. Spin-coating is one of the simplest and widely used methods to fabricate thin films of polymers.³³ By subjecting the substrate to a particular spinning program, the centrifugal forces drive the polymer solution horizontally and at a controlled rate across the surface of the substrate. These forces will cause the polymer solution to spread to, and eventually off, the edge of the substrate forming a thin film of polymer on the surface. Final film thickness will depend on the nature of the polymer solution (viscosity, drying rate, concentration, surface tension, etc.) and the parameters selected for the spin process such as rotational speed and spinning time. In general, higher spin speeds and longer spin times create thinner films.

Film thickness is mainly a balance between the shear force applied to the polymer solution across the surface of the substrate and the drying rate which affects the viscosity of the polymer. As the thin film of polymer dries, the viscosity increases until the shear force can no longer remarkably move the polymer over the surface. At this point, the thickness of the film will not decrease considerably with increased spin time.

3.3.3. Thin-Film Interference Coloration

Thickness of the thin film of polymer deposited on the iridium-coated substrate determines the reflection color. Appropriate rotational speeds and concentrations of polymer solutions were used in order to achieve the desired thicknesses via spin coating. Figure 3.4 shows photographs of thin films of PVP/iridium coated on glass substrates, creating a spectrum of bright interference colors including purple, blue, green, yellow and red.

Similar to PVP samples, thin films of PC/iridium coated on glass substrates display a range of interference colors as shown in Figure 3.5. As it can be observed from PVP and PC samples, the generated interference coloration is tunable by simply changing the thickness of the polymer layer. It is noteworthy that the current approach for generating interference colors can be readily extended to other transparent polymers.

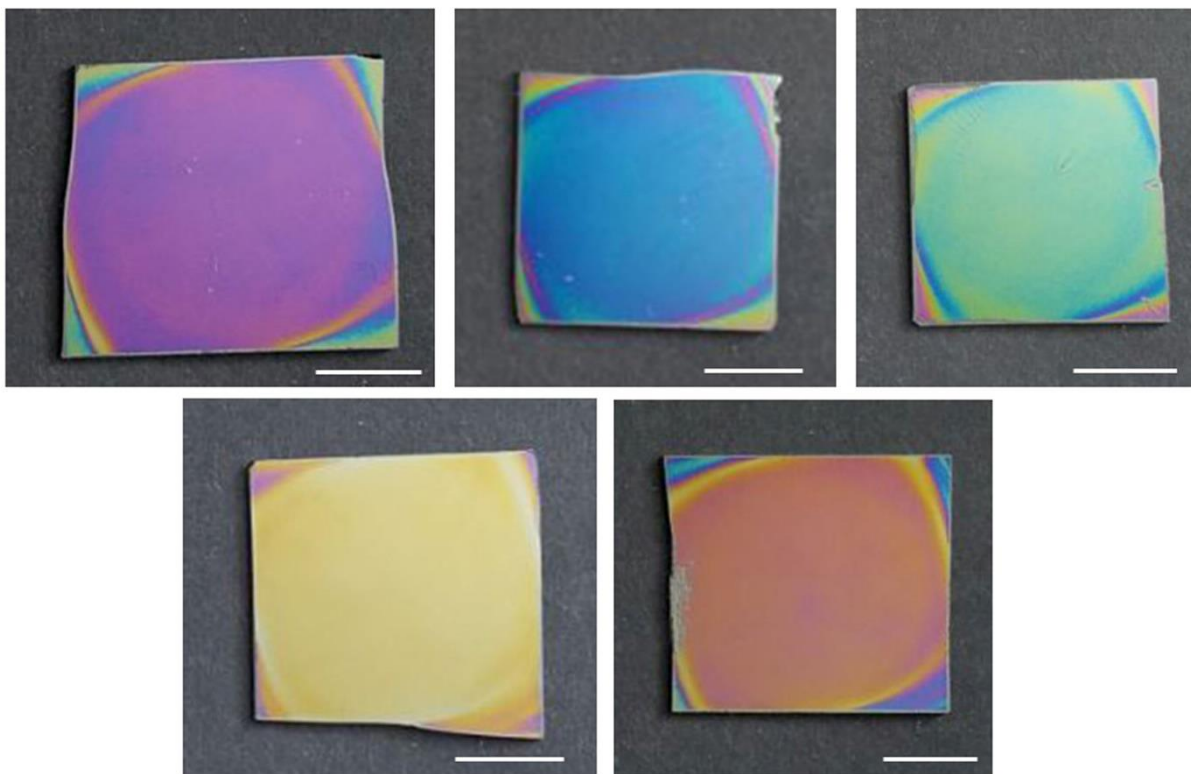


Figure 3.4. Top view photographs of different colors generated by thin films of PVP deposited on iridium-coated glass substrates (thickness of the iridium film= 5 nm). Scale bar: 1 cm.

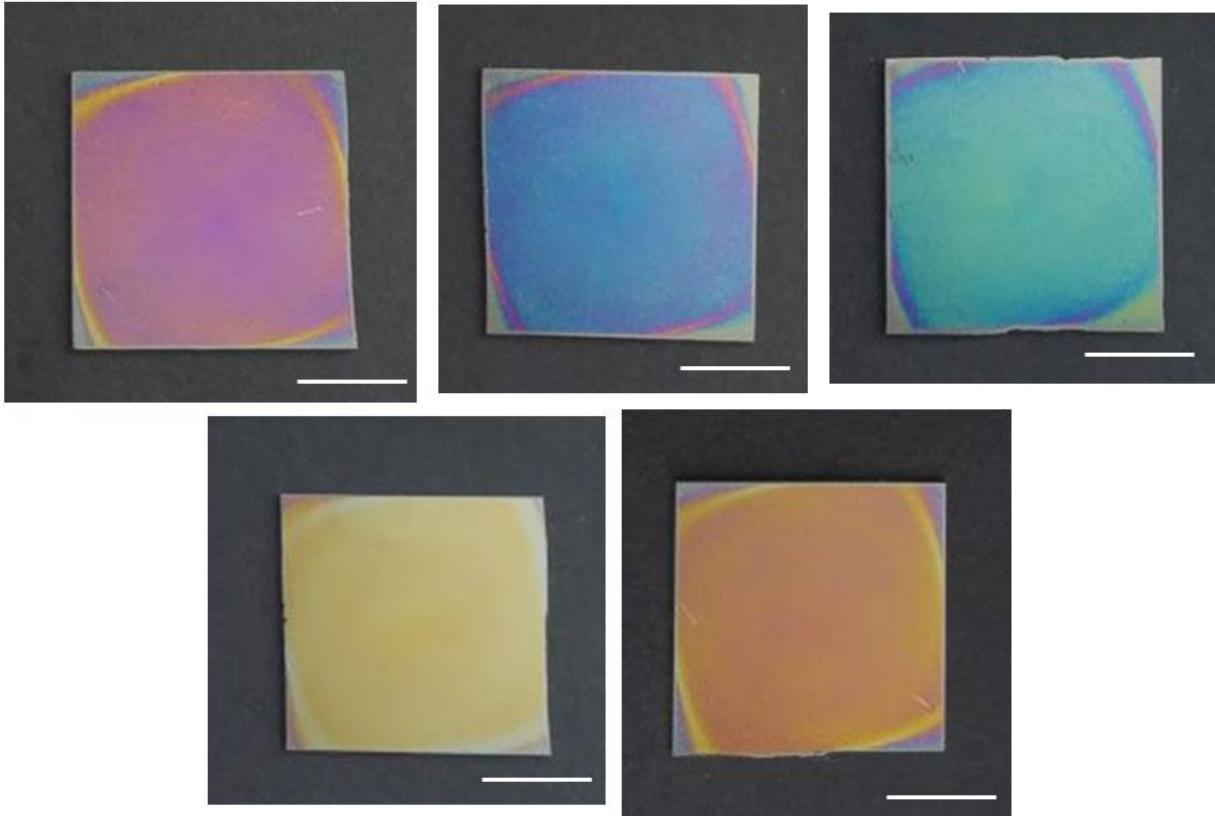


Figure 3.5. Photographs (top view) of different interference colors created by thin films of PC deposited on iridium-coated glass substrates (thickness of the iridium film= 5 nm). Scale bar: 1 cm.

Flexible devices are emerging as important tools for various applications such as wearable electronics, and soft robotics. To demonstrate the feasibility of extending our approach to soft and flexible materials, we fabricated thin films of polymer on top of iridium-coated PDMS substrates in similar fashion. In this study, PDMS was used as the soft and flexible substrate due to its elasticity, transparency and ease of fabrication. PVP was chosen as the polymer layer because its solutions in alcohols do not swell or deform the PDMS substrate during the spin coating stage. In contrast to PVP, the PC solutions in chloroform significantly swell the PDMS substrates and therefore did not lead to high

quality films. Figure 3.6 displays the thin films of PVP deposited on iridium-coated PDMS substrates, creating a spectrum of bright interference colors including purple, blue, green, yellow, and red.

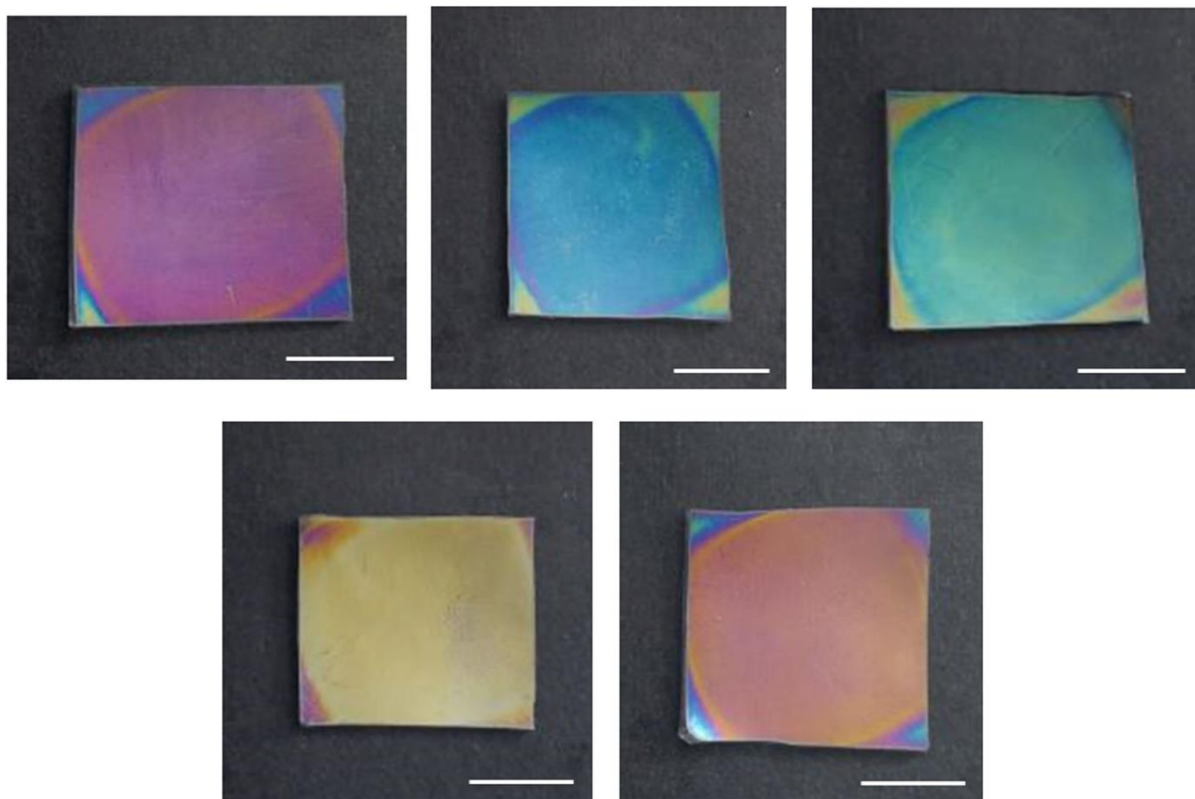


Figure 3.6. Top view images of different colors generated by thin films of PVP deposited on iridium-coated PDMS substrates. Thickness of the iridium film is 5 nm. PDMS substrates are $\sim 750 \mu\text{m}$ thick. Scale bar: 1 cm.

As with other conventional interference colors, our thin films of polymer on iridium-coated substrates exhibit iridescent reflection colors that depend on the viewing angle. The top view, and side view photographs of all generated interference colors are shown in Figure 3.7 (a-f).

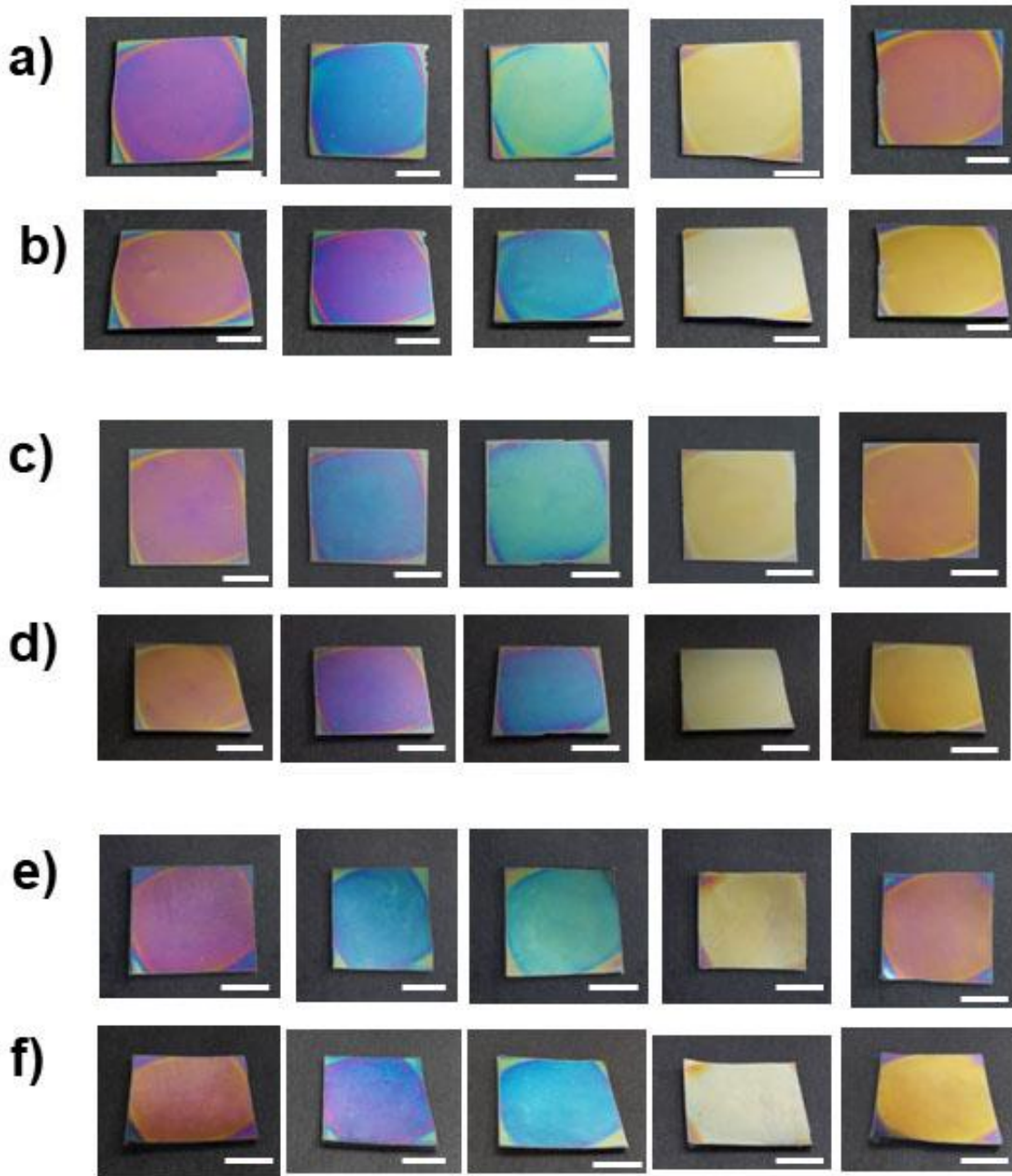


Figure 3.7. Photographs of different interference color coatings generated by thin films of PVP deposited on iridium-coated glass substrates at **(a)** top view **(b)** side view, respectively. Images of various interference colors created by thin films of PC deposited on iridium-coated glass substrates at **(c)** top view **(d)** side view, respectively. Photographs of different interference colors produced by thin films of PVP deposited on iridium-coated PDMS substrates at **(e)** top view **(f)** side view, respectively. Thickness of the iridium film is 5 nm. Scale bar: 1 cm.

To verify the agreement between the thin-film interference theory and our experimental results, we characterized the interference colors generated by thin films of PVP on iridium-coated glass substrates. The reflected light created by thin-film interference is determined by Equation 3.1, where λ is the reflection peak wavelength, m is the order of reflection (a positive integer), d_1 is the thickness of the thin film of PVP, $n_1=1.53$ is the refractive index of PVP and $\theta_1=0^\circ$ is the angle of refraction.

Figure 3.8a shows the cross-sectional SEM image of the thin film of PVP on iridium-coated glass substrate and its corresponding photograph (inset image). The thickness of PVP film measured from the SEM image was 268 nm with a variation in film thickness of 5 nm. According to Equation 3.1, the calculated peak wavelengths for the first- and second-order of reflection were 820, and 410 nm, respectively, which were in reasonable agreement with the experimental peak positions of 801 and 414 nm (Figure 3.8b). This observation reveals that the perceived purple coloration originates from the second-order of reflection.

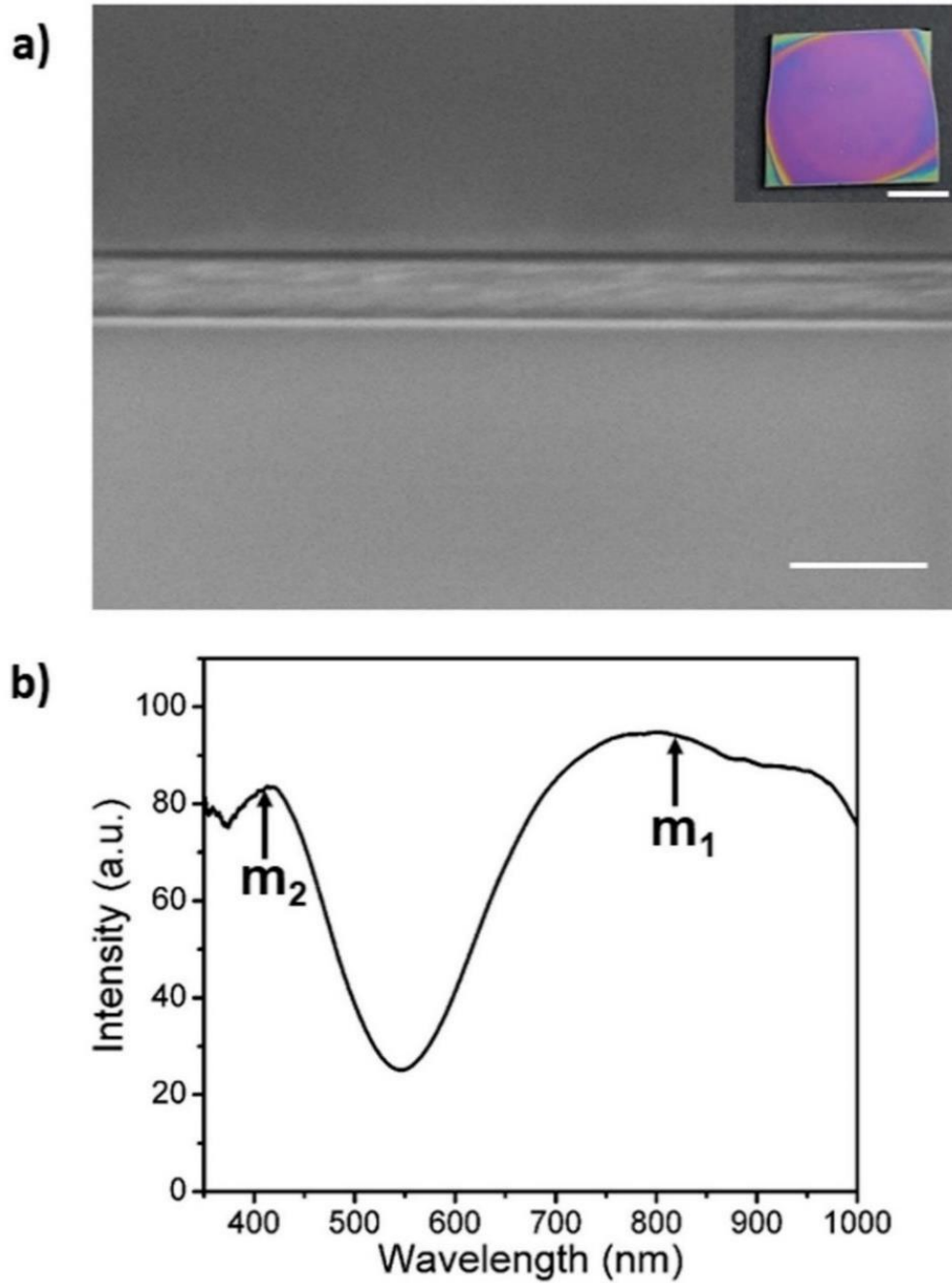


Figure 3.8. (a) Cross-sectional SEM image of the thin film of PVP deposited on iridium-coated glass substrate. Scale bar: 500 nm. Inset image is the corresponding photograph taken at top view. Scale bar: 1 cm. (b) Corresponding reflection spectrum ($\theta_1 = 0^\circ$). The fiber optic is oriented perpendicular to the plane of the glass substrate. The arrows on the spectrum show the calculated peak wavelengths for first-order (m_1) and second-order (m_2) reflections, respectively. Thickness of the iridium film is 5 nm.

In a similar fashion to the purple color, we characterized the other interference colors to confirm the agreement between the theory and experimental measurements. The cross-sectional SEM image of the sample corresponding to the blue interference color is shown in Figure 3.9a. The thickness of the PVP film measured from the SEM image was 303 nm with a variation of 4 nm. According to Equation 3.1, the calculated peak wavelengths for the first- and second-order of reflection were 927, and 464 nm, respectively, which were in good agreement with the experimental peak positions of 954 and 458 nm (Figure 3.9b). This observation indicates that the perceived blue coloration emanates from the second-order of reflection.

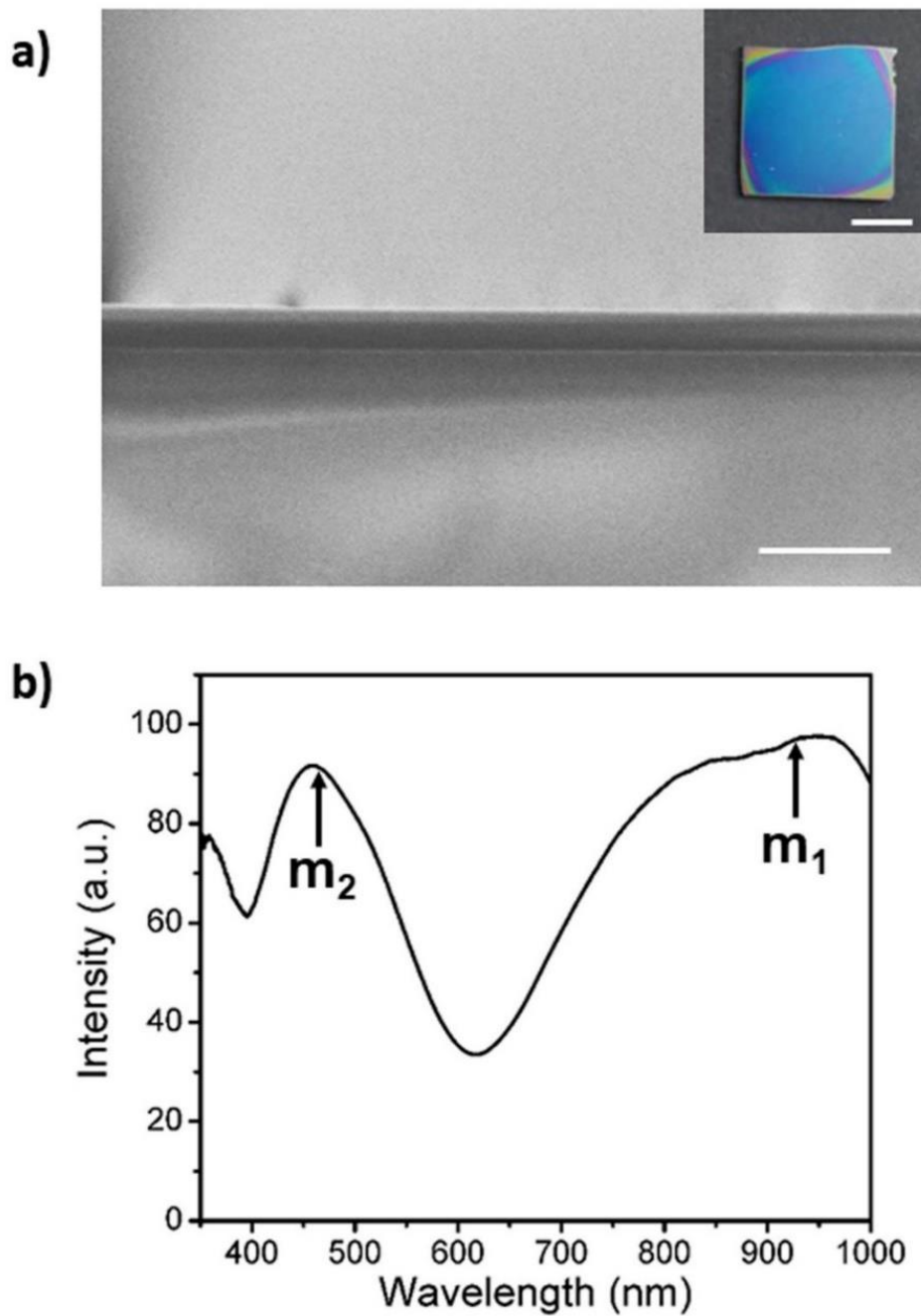


Figure 3.9. (a) Cross-sectional SEM image of the thin film of PVP deposited on iridium-coated glass substrate. Scale bar: 1 μm. Inset image is the corresponding photograph taken at top view. Scale bar: 1 cm. (b) Corresponding reflection spectrum ($\theta_1=0^\circ$). The fiber optic is oriented perpendicular to the plane of the glass substrate. The arrows on the spectrum show the calculated peak wavelengths for first-order (m_1) and second-order (m_2) reflections, respectively. Thickness of the iridium film is 5 nm.

Figure 3.10a shows the cross-sectional SEM image of the sample corresponding to the green interference color. The thickness of the PVP film measured from the SEM image was 342 nm with a film thickness variation of 3 nm. According to Equation 3.1, the calculated peak wavelengths for the first-, second- and third-order of reflection were 1047, 523 and 349 nm, respectively, which were in rough agreement with the experimental peak positions of 967, 518 and 367 nm (Figure 3.10b). This finding reveals that the perceived green coloration stems from the second-order of reflection.

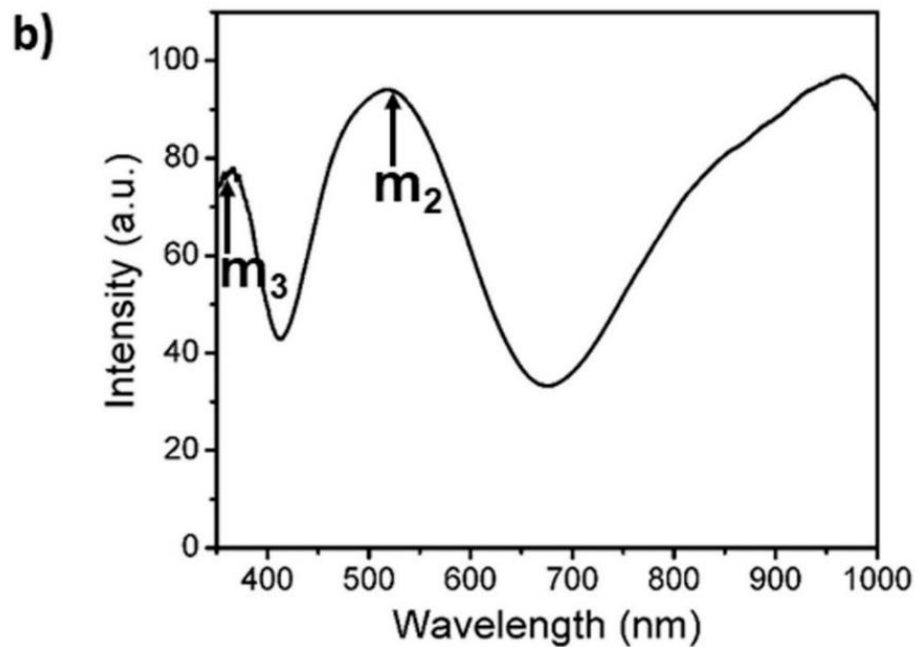
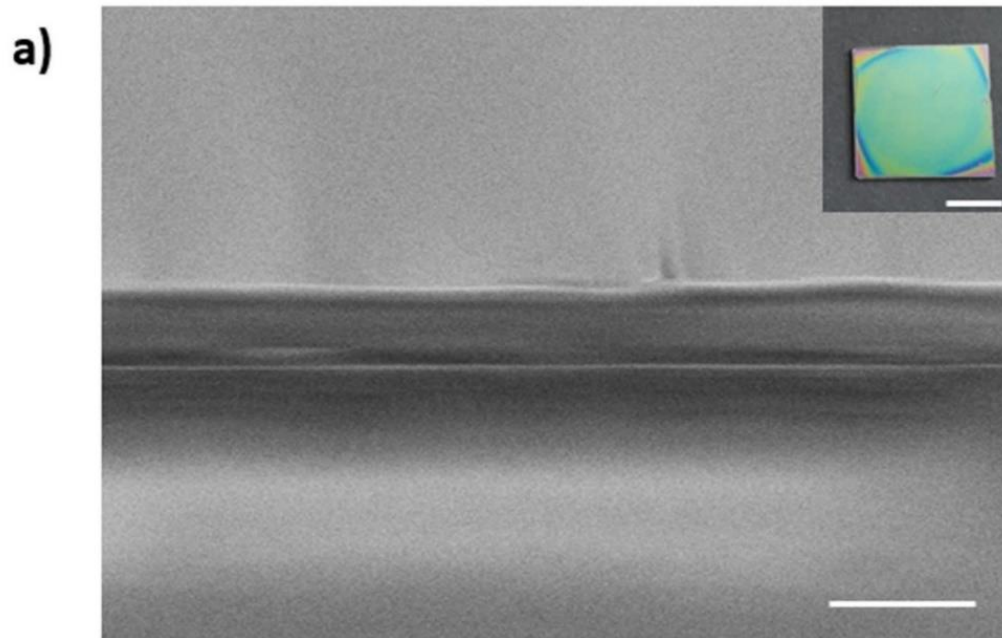


Figure 3.10. (a) Cross-sectional SEM image of the thin film of PVP deposited on iridium-coated glass substrate. Scale bar: 1 μm . Inset image is the corresponding photograph taken at top view. Scale bar: 1 cm. **(b)** Corresponding reflection spectrum ($\theta_1 = 0^\circ$). The fiber optic is oriented perpendicular to the plane of the glass substrate. The arrows on the spectrum show the calculated peak wavelengths for second-order (m_2) and third-order (m_3) reflections, respectively. Thickness of the iridium film is 5 nm.

The cross-sectional SEM image of sample corresponding to the yellow interference color is shown in Figure 3.11a. The thickness of the PVP film measured from the SEM image was 386 nm with a variation of 6 nm. According to Equation 3.1, the calculated peak wavelengths for the second- and third-order of reflection were 591 and 394 nm, respectively, which were in good agreement with the experimental peak positions of 585 and 393 nm (Figure 3.11b). This observation confirms that the perceived yellow coloration originates from the second-order of reflection. The calculated peak for the first-order of reflection at 1181 nm was beyond the detection limits of our spectrometer.

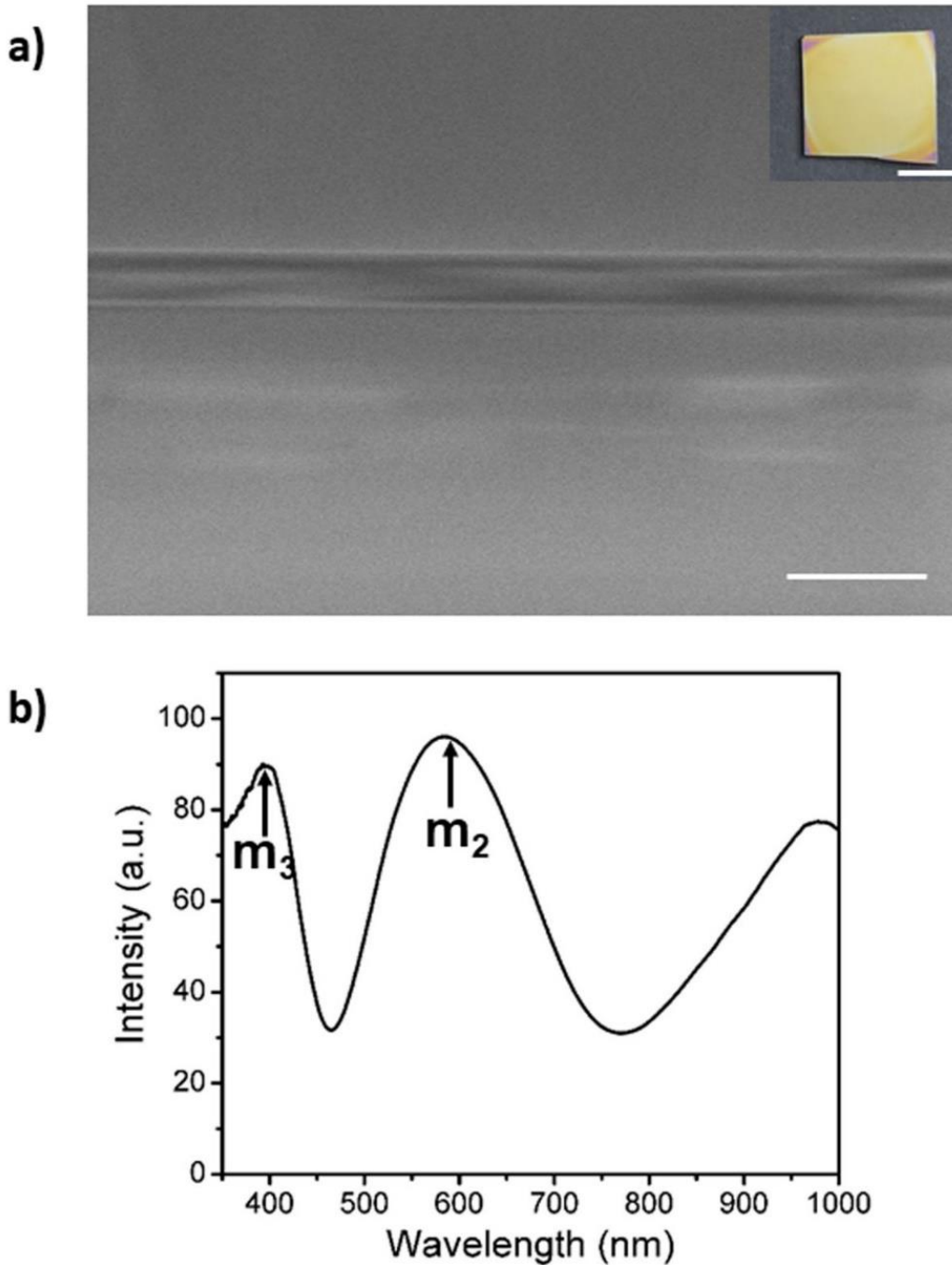


Figure 3.11. (a) Cross-sectional SEM image of the thin film of PVP deposited on iridium-coated glass substrate. Scale bar: 1 μm . Inset image is the corresponding photograph taken at top view. Scale bar: 1 cm. **(b)** Corresponding reflection spectrum ($\theta_1 = 0^\circ$). The fiber optic is oriented perpendicular to the plane of the glass substrate. The arrows on the spectrum show the calculated peak wavelengths for second-order (m_2) and third-order (m_3) reflections, respectively. Thickness of the iridium film is 5 nm.

Figure 3.12a shows the cross-sectional SEM image of the sample corresponding to the red interference color. The thickness of the PVP film measured from the SEM image was 481 nm with a variation in film thickness of 5 nm. According to Equation 3.1, the calculated peak wavelengths for the second-, third- and fourth-order of reflection were 736, 491 and 368 nm, respectively. Similar to the sample with yellow color, the calculated peak for the first-order of reflection at 1471 nm was out of the detection limits of our spectrometer. Although, the calculated second- and fourth-order of reflection were in reasonable agreement with the experimental peaks of 727 and 381 nm, respectively, the third-order of reflection was absent in the spectrum (Figure 3.12b). These observations confirm that the perceived red coloration emanates from the second-order of reflection.

Moreover, absorption spectrum of the red interference color was recorded. As it can be seen in Figure 3.13, the red color does not show any absorption peak in the region of interest (wavelengths of around 491 nm). A deeper understanding of the absence of m_3 reflection peak for the samples having red interference color requires further experimental and theoretical studies.

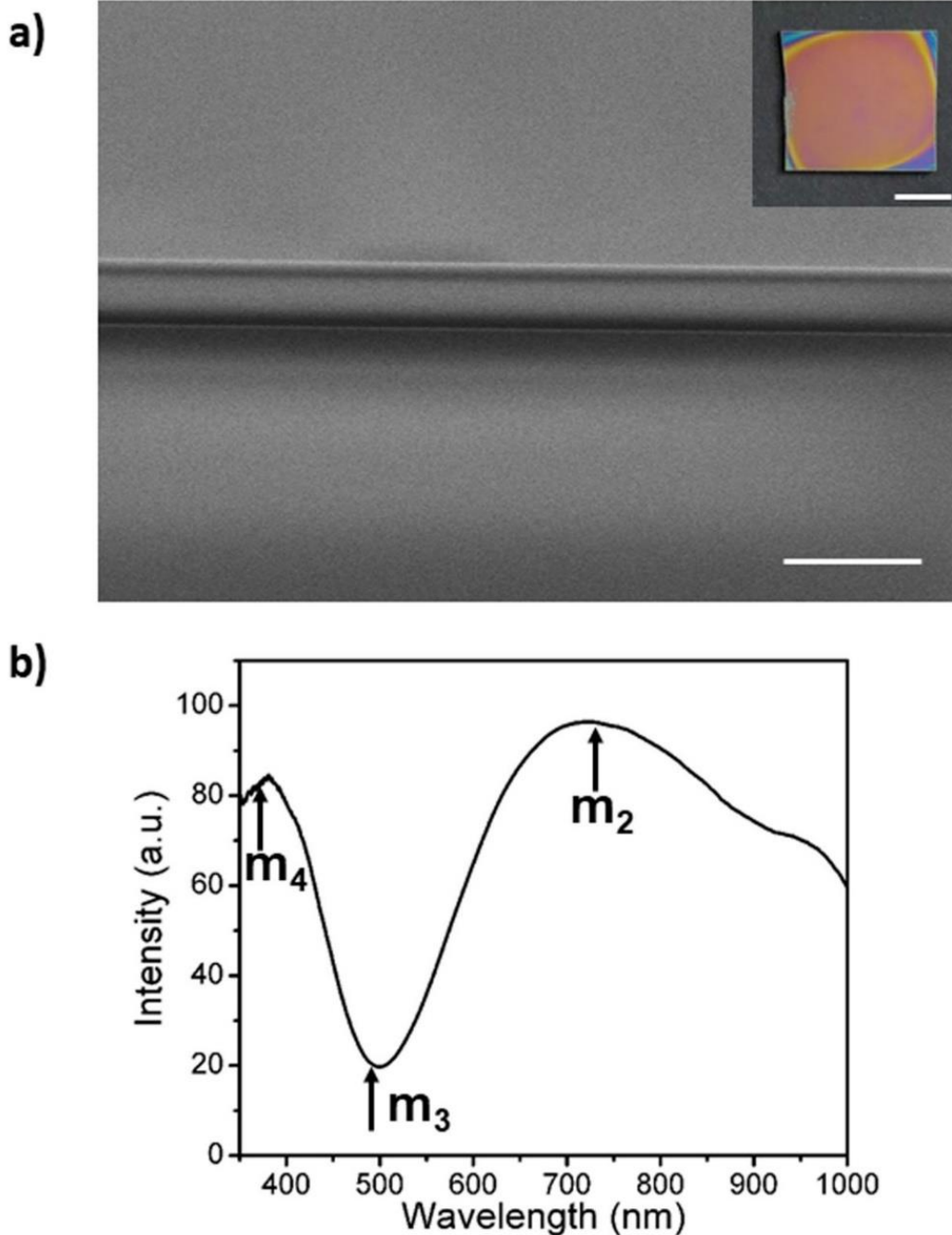


Figure 3.12. (a) Cross-sectional SEM image of the thin film of PVP deposited on iridium-coated glass substrate. Scale bar: $1\mu\text{m}$. Inset image is the corresponding photograph taken at top view. Scale bar: 1 cm . **(b)** Corresponding reflection spectrum ($\theta_1 = 0^\circ$). The fiber optic is oriented perpendicular to the plane of the glass substrate. The arrows on the spectrum show the calculated peak wavelengths for second-order (m_2), third-order (m_3), and fourth-order (m_4) reflections, respectively. Thickness of the iridium film is 5 nm .

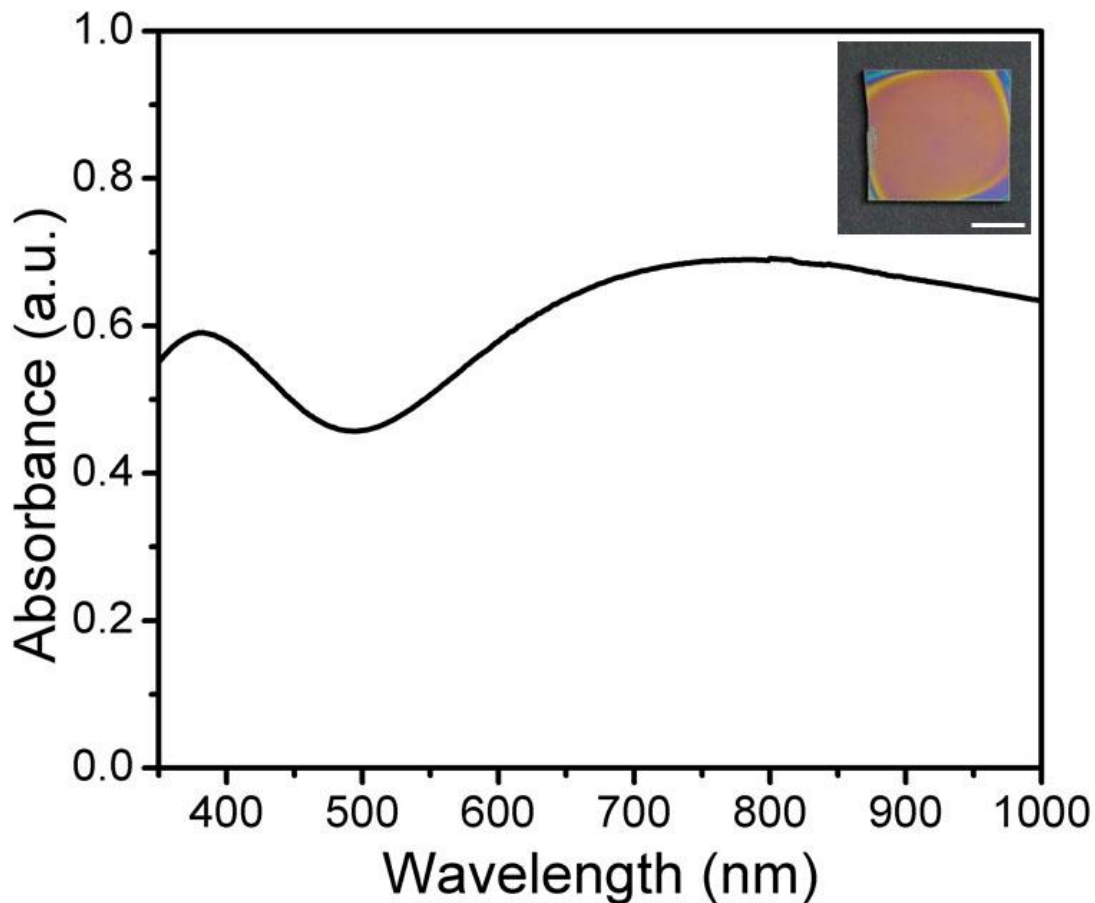


Figure 3.13. Absorption spectrum of the thin film of PVP deposited on iridium-coated glass substrate. Inset image is the corresponding photograph at top view. Thickness of the iridium film is 5 nm. Scale bar: 1 cm.

In addition to continuous coatings, patterned interference coloration can be produced by combining the deposition of thin films of polymer with conventional stenciling techniques. As an example, we generated interference color patterns by placing a pre-cut plastic stencil mask on top of a glass substrate prior to metal deposition. After sputter coating the iridium through the mask, the PVP solution was spin-coated at specific speeds on the substrate. Figure 3.14 shows the three primary color patterns (blue, yellow, and

red) created by varying the spinning speed. Diverse color patterns with versatile size and shape can be produced through careful choice of mask.

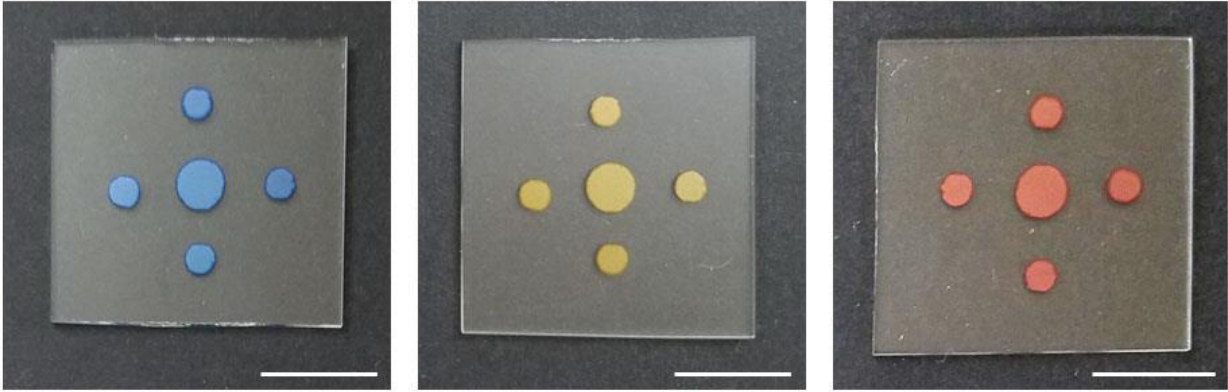


Figure 3.14. Photographs (top view) of the interference color patterns generated by thin films of PVP deposited on iridium-coated glass substrate. To form patterns, a pre-cut plastic stencil mask was used during the sputter coating of iridium. Thickness of the iridium film is 5 nm. Scale bar: 1 cm.

To create bright interference coloration, the metal thickness plays an important role. Figure 3.15 shows the photo images of interference coloration generated by thin films of PVP on glass substrates coated with different thicknesses of iridium. As seen in Figure 3.15, a balance between reflection and transmission has to be struck in order to create bright interference coloration.

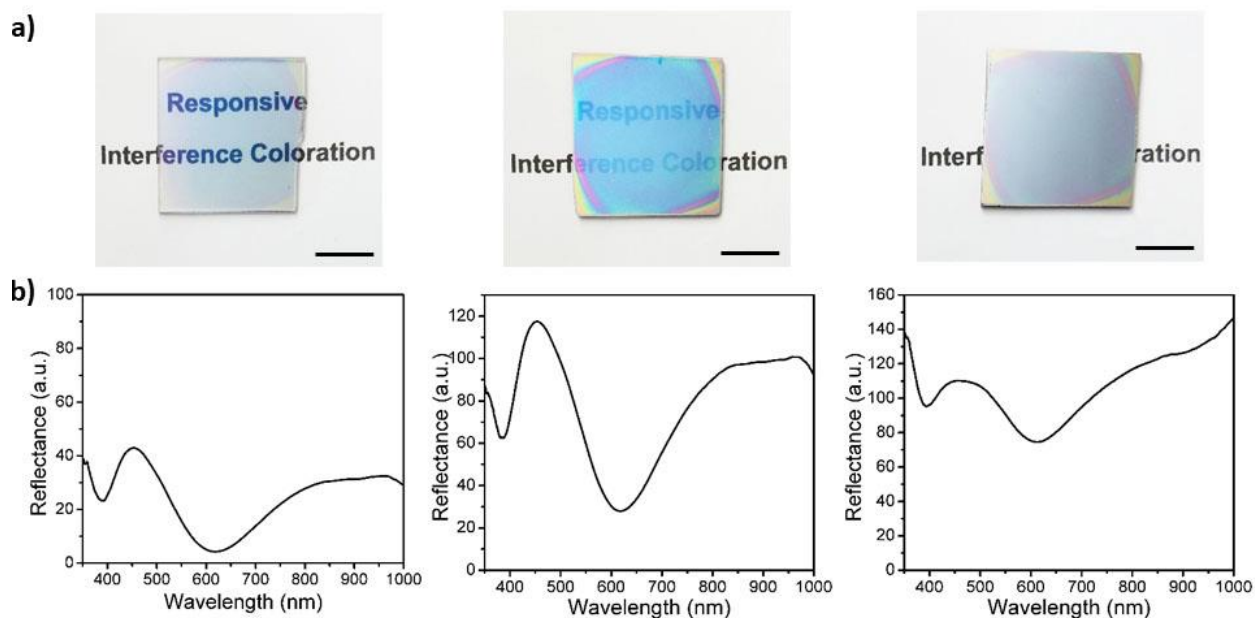


Figure 3.15. Effect of the thickness of metal coating on the interference coloration. **(a)** Photo images (top view), and **(b)** reflection spectra ($\theta_1 = 0^\circ$) of the interference coloration generated by thin films of PVP on the glass substrates coated with various thicknesses of iridium (from left to right: 1 nm, 5 nm, and 50 nm). Scale bar: 1 cm.

3.3.4. Responsive Interference Coloration

Recently, there has been a growing interest in humidity-responsive colorimetric sensors for health, industrial and technological applications.³⁴⁻⁴¹ Although these sensors have realized colorimetric detection of humidity, there is still a great need to develop low-cost and low-power sensors with a fast response time.

Here, we demonstrated a colorimetric sensor that has an excellent sensitivity to humidity, since the PVP will swell in a high humidity environment and shrink in a low humidity environment, which will lead to visual color changes. Our observations show that the thickness of the polymer film is the dominant reason for the color changes of our PVP

samples. Due to using PVP as the stimuli responsive polymer, when the sample is subjected to mist, it will absorb microparticles of water and swell which leads to an increase in the thickness of the PVP film (from d_1 to $d_1 + \Delta d_1$) further resulting in red-shift of the interference color (Figure 3.16a).

Figure 3.16b shows top-view photographs of thin film of PVP deposited on iridium-coated glass slide when it is subjected to mist generated by a commercial humidifier (Radha Beauty Co.). As seen in Figure 3.16b, the interference coloration shifts from blue to red upon exposure to mist. The experiment was performed at room temperature ($23 \pm 1^\circ\text{C}$). When the humidity varies, the color changes from blue to red and returns to its original color upon turning off the humidifier. We have conducted over 30 cycles of humidity test on each sample and have not observed any visible damage to the quality of the thin PVP films. Response time is another important factor to evaluate sensitivity of a sensor. As seen in Figure 3.16c, the initial response of the interference coloration occurs within 0.23 seconds of exposure to mist. This observation indicates that the photonic humidity sensor is very sensitive to the changes in the humidity.

The reason why our humidity sensor has such excellent sensitivity behavior could be explained by the properties of the thin polymeric film used in the preparation of the interference colors. The properties of the polymer are found to be critical to the performance of the humidity sensor. In our system, we select PVP as the stimuli-responsive polymer which is hygroscopic and has a fast response to the changes in humidity. To confirm the role of polymer layer in our humidity sensor, we conducted the humidity test on interference color created by thin film of PC deposited on iridium coated

glass substrate in similar fashion, and we have never observed any color change upon exposure to mist (Figure 3.17).

It is noteworthy that although we have demonstrated the responsiveness of our interference coloration to the humidity changes, the current approach can be easily extended to other environmental stimuli such as chemicals, mechanical forces, biomolecules, and heat by careful choice of polymer.

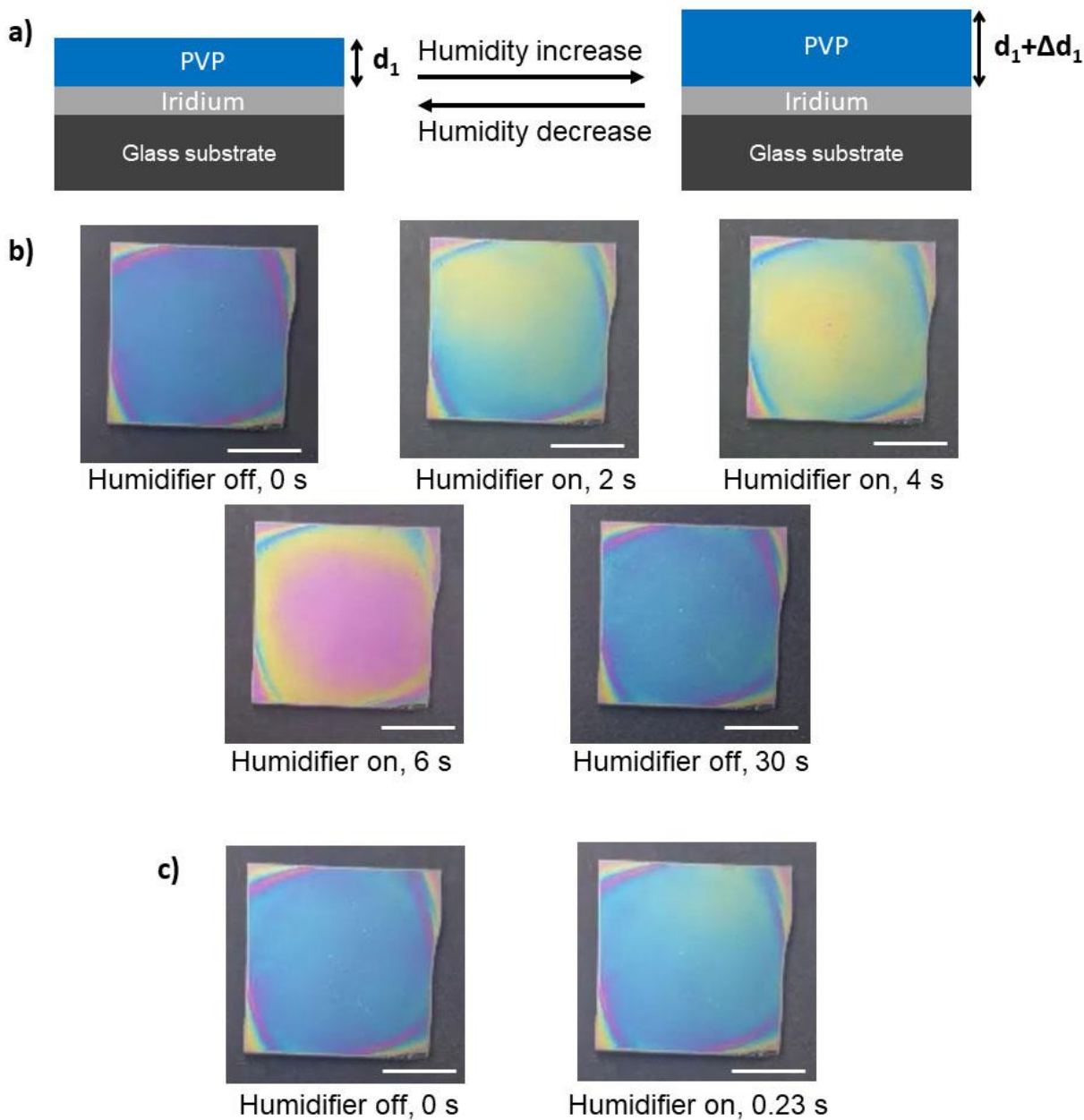


Figure 3.16. (a) A schematic illustration of the mechanism of color change in the thin film of PVP deposited on iridium-coated glass substrate between high and low humidity environments. (b) Photographs (top view) of the thin film of PVP deposited on iridium-coated glass substrate in response to mist created by a humidifier. (c) Photo images (top view) of the initial response of the thin film of PVP deposited on iridium-coated glass substrate to mist generated by a humidifier. Thicknesses of the PVP and iridium films are ~ 300 nm and 5 nm, respectively. Scale bar: 1 cm.

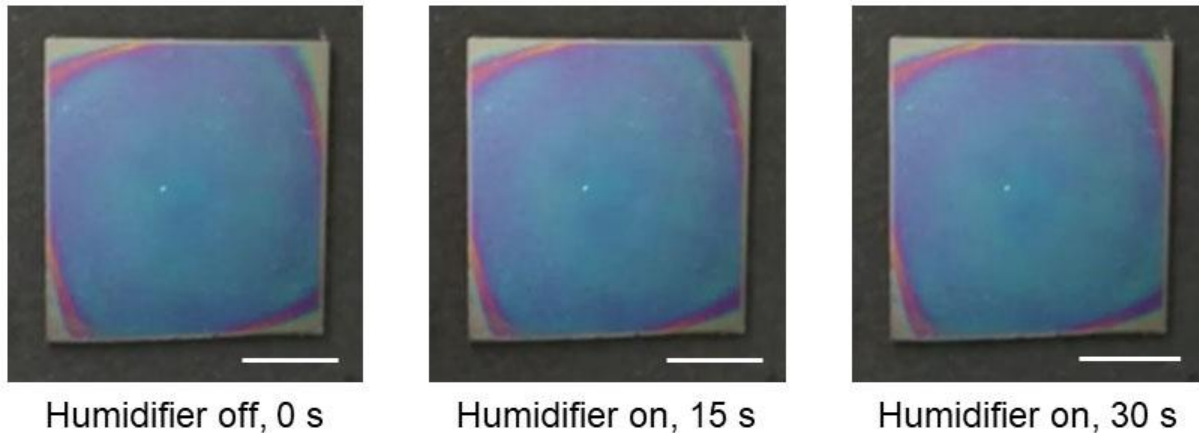


Figure 3.17. Photographs (top view) of the thin film of PC deposited on iridium-coated glass substrate in response to mist created by a humidifier. Thickness of the iridium film is 5 nm. Scale bar: 1 cm.

3.4. Conclusion

In summary, we have developed a new scalable and affordable platform technology for fabrication of polymer-based, stimuli-responsive interference colored films. Our approach is based on a laminated structure in which a thin film of a transparent polymer is deposited on a metal-coated substrate. The facile fabrication process not only allows us to create full spectrum of interference colors on rigid substrates by simply adjusting the thickness of the polymer layer, but also enables us to form a wide range of colors on soft and flexible substrates. The thickness of the transparent polymer layer determines the reflected color, whereas the thickness of the metal layer controls the intensity of the reflected color.

Moreover, various color patterns with different shapes and sizes can be created by choosing the appropriate mask. Furthermore, we have demonstrated the responsiveness of our interference colored films to an environmental stimulus where the

film undergoes fast and reversible changes of surface color upon changes in environmental humidity.

Although we have focused on using spin-coating and sputter deposition methods to form the laminated structures in this study, our approach can be easily extended to other fabrication techniques to create thin films of polymers and metals on desired substrates. Such polymer-based, responsive interference coloration could empower colorimetric sensing of various environmental stimuli (e.g. humidity, chemicals, heat, biomolecules, and mechanical forces), which could enable a wide range of applications.

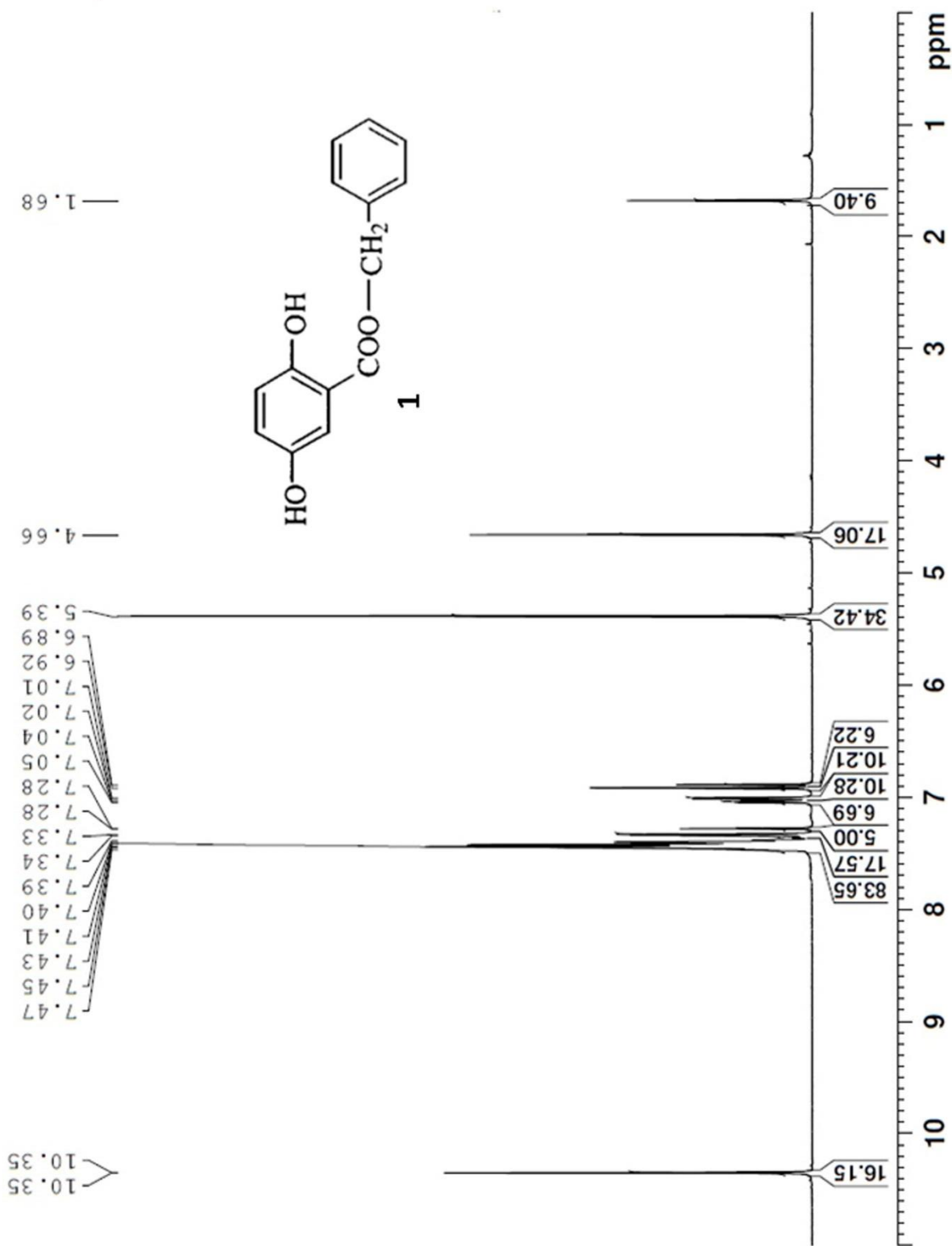
3.5. References

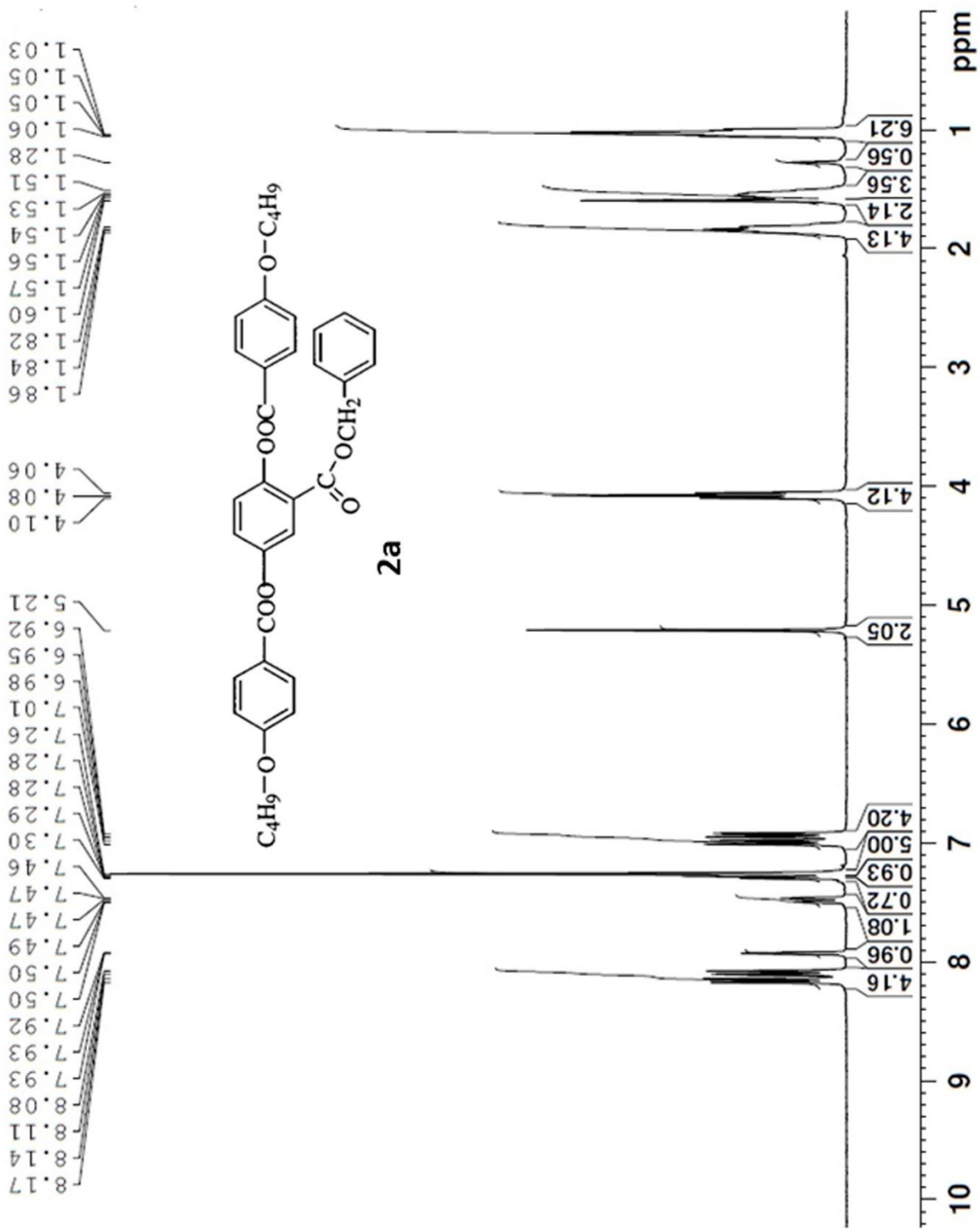
- (1) Zhao, Y.; Xie, Z.; Gu, H.; Zhu, C.; Gu, Z. *Chem. Soc. Rev.* **2012**, 41, 3297-3317.
- (2) Sun, J.; Bhushan, B.; Tonga, J. *RSC Adv.* **2013**, 3, 14862-14889.
- (3) Fu, Y.; Tippets, C. A.; Donev, E. U.; Lopez, R. *WIREs Nanomed. Nanobiotechnol* **2016**, 8, 758-775.
- (4) Kinoshita, S.; Yoshioka, S.; Miyazaki, J. *Rep. Prog. Phys.* **2008**, 71, 076401.
- (5) Burgess, I. B.; Loncar, M.; J. Aizenberg, J. *J. Mater. Chem. C* **2013**, 1, 6075-6086.
- (6) Ji, C.; Lee, K.-T.; Xu, T.; Zhou, J.; Park, H. J.; Guo, L. J. *Adv. Optical Mater.* **2017**, 5, 1700368.
- (7) Ge, J.; Yin, Y. *Angew. Chem. Int. Ed.* **2011**, 50, 1492-1522.
- (8) Wang, H.; Zhang, K., -Q. *Sensors* **2013**, 13, 4192-4213.
- (9) Chan, E. P.; Walish, J. J.; Urbas, A. M.; Thomas, E. L. *Adv. Mater.* **2013**, 25, 3934-3947.

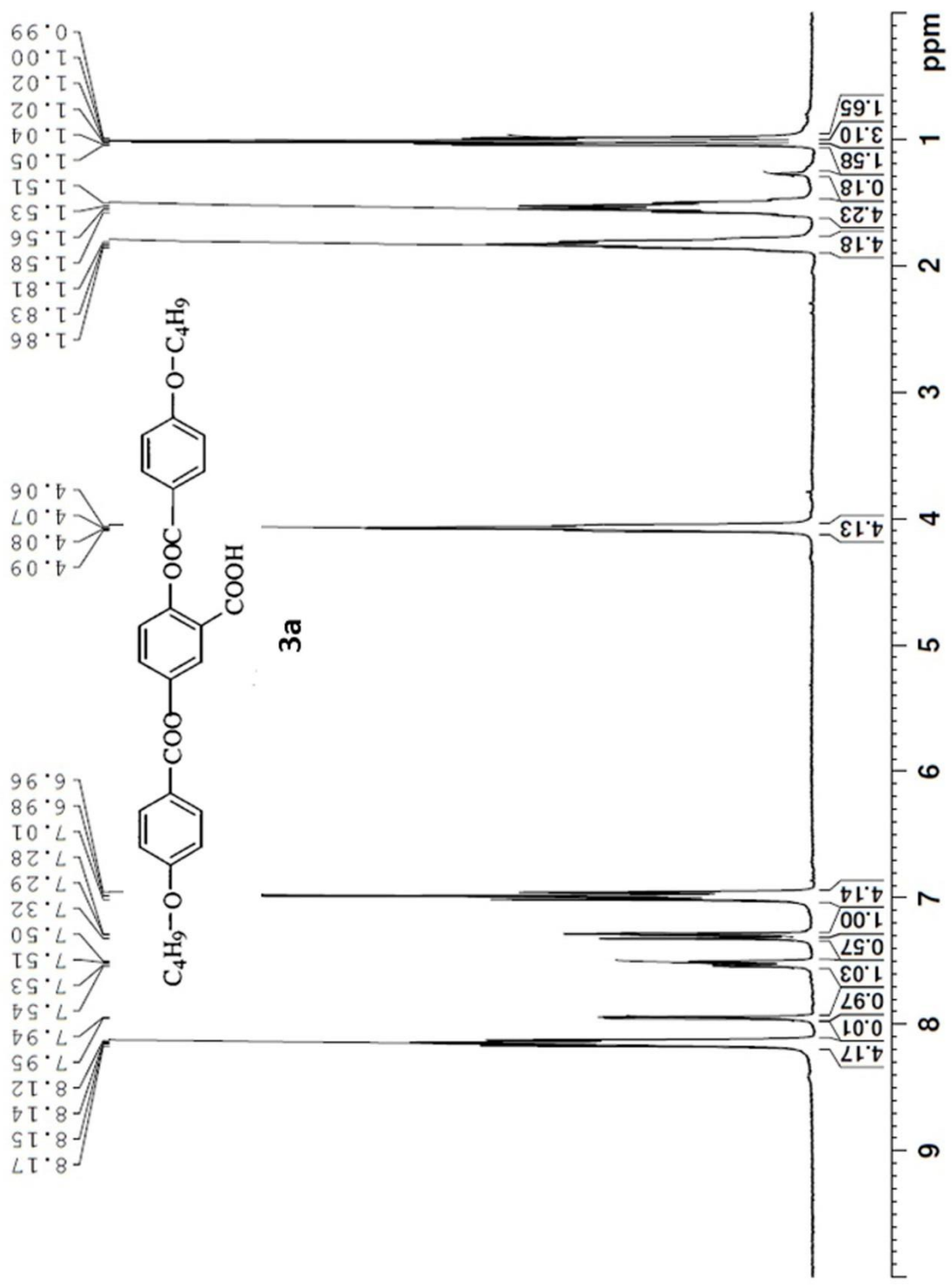
- (10) Fudouzi, H.; Xia, Y. *Langmuir* **2003**, 19, 9653-9660.
- (11) Fudouzi, H.; Sawada, T. *Langmuir* **2006**, 22, 1365-1368.
- (12) Viel, B.; Ruhl, T.; Hellmann, G. P. *Chem. Mater.* **2007**, 19, 5673-5679.
- (13) Arsenault, A. C.; Puzzo, D. P.; Manners, I.; Ozin, G. A. *Nat. Photonics* **2007**, 1, 468-472.
- (14) Schäfer, C. G.; Viel, B.; Hellmann, G. P.; Rehahn, M.; Gallei, M. *ACS Appl. Mater. Interfaces* **2013**, 5, 10623-10632.
- (15) Schäfer, C. G., M. Gallei, M.; Zahn, J. T.; Engelhardt, J.; Hellmann, G. P., Rehahn, M. *Chem. Mater.* **2013**, 25, 2309-2318.
- (16) Ito, T.; Katsura, C.; Sugimoto, H.; Nakanishi, E.; Inomata, K. *Langmuir* **2013**, 29, 13951-13957.
- (17) Schäfer, C. G.; Lederle, C.; Zentel, K.; Stühn, B.; Gallei, M. *Macromol. Rapid Commun.* **2014**, 35, 1852-1860.
- (18) Cho, Y.; Lee, S. Y.; Ellerthorpe, L.; Feng, G.; Lin, G.; Wu, G.; Yin, J.; Yang, S. *Adv. Funct. Mater.* **2015**, 25, 6041-6049.
- (19) Holtz, J. H.; Asher, S. A. *Nature* **1997**, 389, 829-832.
- (20) Arsenault A. C.; Clark, T. J.; von Freymann G.; Cadematiri, L.; Sapienza, R.; Bertolotti, J.; Vekris, E.; Wong, S.; Kitaev, V.; Manners, I.; Wang, R. Z.; John, S.; Wiersma, D.; Ozin, G. A. et al. *Nat. Mater.* **2006**, 5, 179.
- (21) Howell I. R.; Li, C.; Colella, N. S.; Ito, K.; Watkins, J. J. *ACS Appl. Mater. Interfaces* **2015**, 7, 3641-3646.
- (22) Macleod, H. A. *Thin-film Optical Filters*, London Adam Hilger, London, UK, **1986**.
- (23) Stavenga, D. G. *Materials Today: Proceedings* **2014**, 1S, 109-121.
- (24) Kats, M. A.; Blanchard, R.; Ramanathan, S.; Capasso, F. *Optics and Photonics News* **2014**, 25, 40-47.
- (25) Kats, M. A.; Capasso, F. *Laser Photonics Rev.* **2016**, 10, 735-749.
- (26) Lee, K. -T.; Seo, S.; Lee, J. Y.; Guo, L. J. *Appl. Phys. Lett.* **2014**, 104, 231112.
- (27) Gaul, E. J. *Chem. Edu.* **1993**, 70, 176-178.

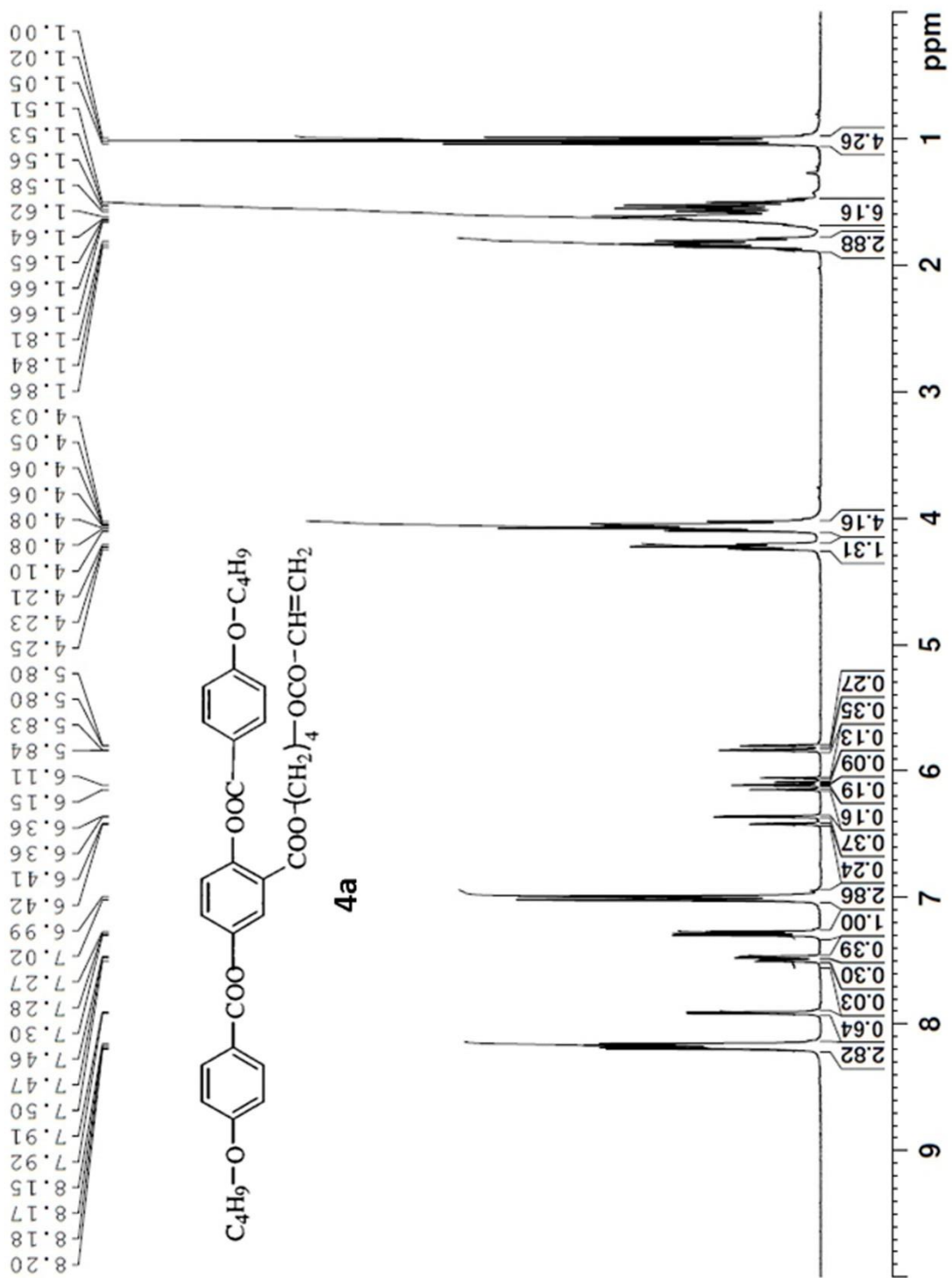
- (28) Kats, M. A.; Blanchard, R.; Genevet, P.; Capasso, F. *Nature Mater.* **2013**, 12, 20-24.
- (29) Kats, M. A.; Capasso, F. *Appl. Phys. Lett.* **2014**, 105, 131108.
- (30) Behl, M.; Zotzmann, J.; Lendlein, A. *Adv. Polym. Sci.* **2010**, 226, 1-40.
- (31) Oliver, K.; Seddon, A.; Trask, R. S. *J. Mater. Sci.* **2016**, 51, 10663-10689.
- (32) Wasa, K.; Hayakawa, S. *Handbook of Sputter Deposition Technology*, Noyes, Park Ridge, USA, **1992**.
- (33) Hall, D. B.; Underhill, P.; Torkelson, J. M. *Polym. Eng. Sci.* **1998**, 38, 2039-2045.
- (34) Shin, B.; Ha, J.; Lee, M.; Park, K.; Park, G. H.; Choi, T. H.; Cho, K. -J.; Kim H. - Y. *Sci. Robot.* **2018**, 3, eaar2629.
- (35) Dai, M.; Picot, O. T.; Verjans, J. M. N.; de Haan, L. T.; Schenning, A. P. H. J.; Peijs, T.; Bastiaansen, C. W. M. *ACS Appl. Mater. Interfaces* **2013**, 5, 4945-4950.
- (36) Huang, J., Tao, C.; An, Q.; Lin, C.; Li, X.; Xu, C.; Wu, Y.; Li, X.; Shen, D.; Li, G. *Chem. Commun.* **2010**, 46, 4103-4105.
- (37) Hu, H.; Chen, Q. -W.; Cheng, K.; Tang J. *J. Mater. Chem.* **2012**, 22, 1021.
- (38) Hawkeye, M. M.; Brett, M. J. *Adv. Funct. Mater.* **2011**, 21, 3652-3658.
- (39) Chi, H.; Liu, Y. J.; Wang, F.; He, C. *ACS Appl. Mater. Interfaces* **2015**, 7, 19882-19886.
- (40) Tian, E.; Wang, J.; Zheng, Y.; Song, Y.; Jianga L.; Zhu D. *J. Mater. Chem.* **2008**, 18, 1116-1122.
- (41) Barry, R. A.; Wiltzius, P. *Langmuir* **2006**, 22, 1369-1374.

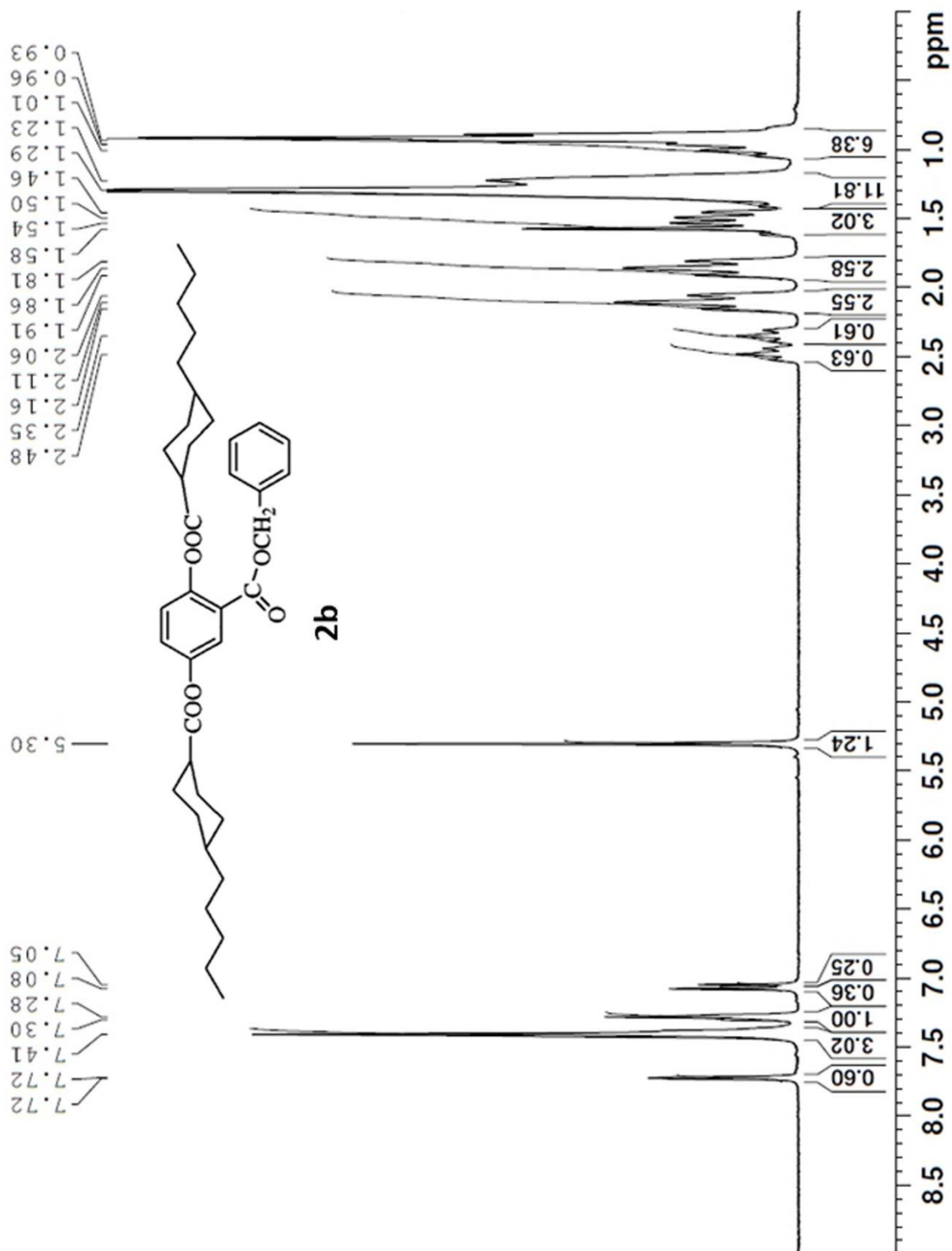
APPENDIX: $^1\text{H-NMR}$ spectra of compounds 1, 2a, 3a, 4a, 2b, 3b, and 4b.

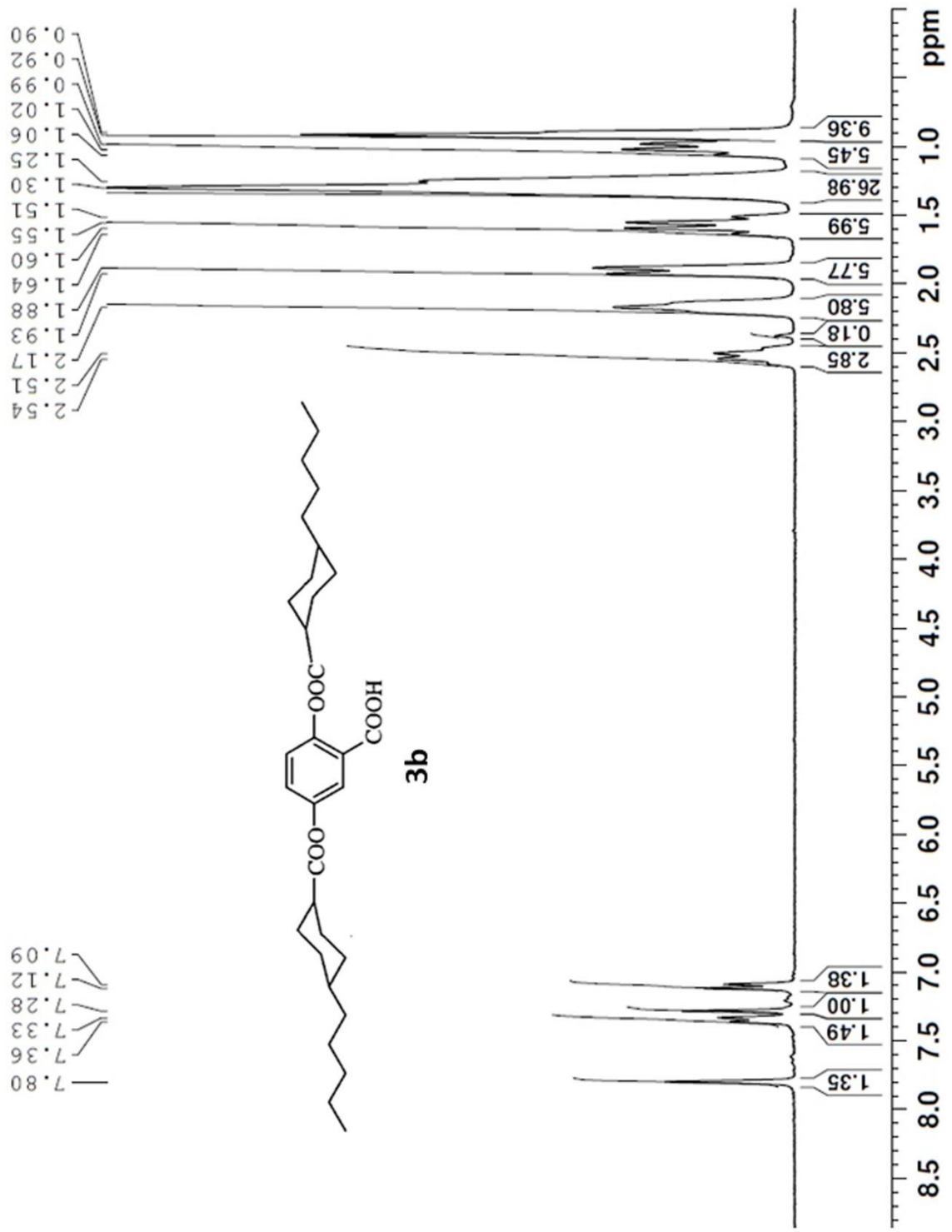


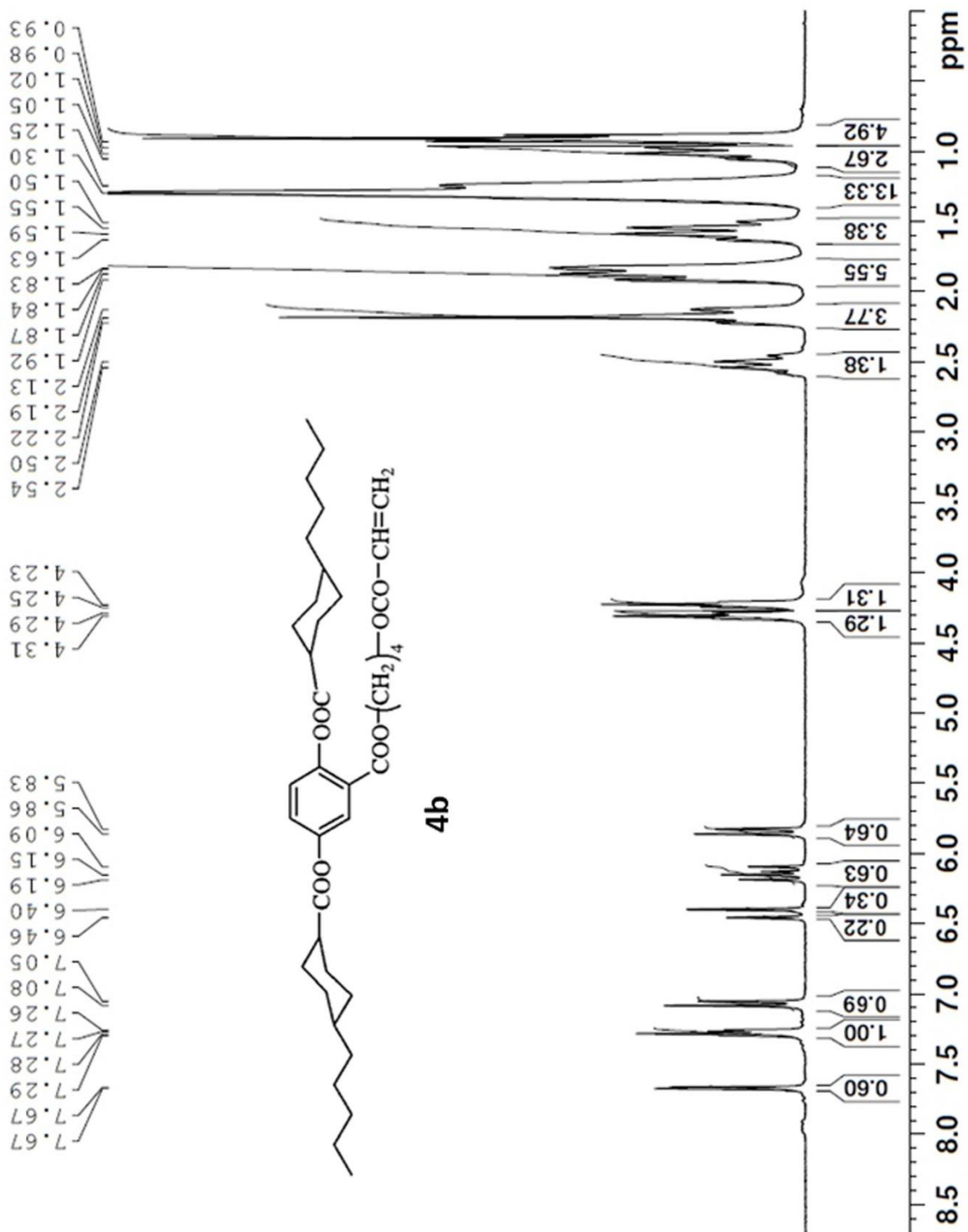












Seyedali Banisadr

Education

Ph.D., Chemistry

University of Wisconsin-Milwaukee, Milwaukee, WI, USA

September 2012-May 2018

Advisor: Prof. Jian Chen

Dissertation: New Approaches to Multi-Functional Soft Materials

M.Sc., Polymer Science and Engineering

Amirkabir University of Technology, Tehran, Iran

September 2008-October 2010

B.Sc., Polymer Science and Engineering

Azad University, Science and Research Branch, Tehran, Iran

September 2003-February 2008

Research Experience

Graduate Research Assistant, University of Wisconsin-Milwaukee, Milwaukee, WI
January 2013-May 2018

- Developed a bio-inspired, remote-controlled soft robotic device that undergoes simultaneous reconfiguration of surface color and shape upon infrared (IR) actuation
- Synthesized and analyzed various types of surface-functionalized, and highly-monodispersed polymeric nanospheres through emulsion polymerization
- Fabricated wavelength-selective, IR light-driven nanocomposite films based on nematic liquid crystalline elastomer composites
- Synthesized, purified, and characterized liquid crystalline monomers with side-on mesogenic units
- Skilled in Design of Experiments (Design Expert), Simulations (ANSYS), Data Analysis (Origin), 3D-Modeling (SketchUp), Microsoft office (Word, Excel, PowerPoint), Graphics (Adobe Photoshop), and have hands-on experience in programming (MATLAB)
- Imaging techniques: SEM, Polarized optical microscopy
- Spectroscopy techniques: FTIR, ATR, NMR, UV-Visible-NIR, Raman spectroscopy
- Analytical techniques: TGA, DSC, DMA, Tensile test, EDX, XRD, XRF, Two/four-point probe resistivity measurements
- Thin film fabrication techniques: Spin coating, Sputter coating, Spray coating, Solution casting, Thermal vacuum deposition
- Performed annual safety inspections, oversaw the chemical inventory, monitored the safety of the laboratory activities, and composed standard operating procedures as the laboratory safety coordinator

Graduate Research Assistant, Amirkabir University of Technology, Tehran, Iran
June 2009-October 2010

- Significantly enhanced the photo-oxidation and biodegradability rate of low density polyethylene (LDPE) films

Work Experience

Research & Development Intern-Polymers, Sherwin-Williams Co., Warrensville, OH
May 2017-August 2017

- Synthesized and analyzed water-borne and solvent-borne alkyd resins which contributed to the R&D team's objectives in optimizing the physical properties of the coatings for architectural and heavy industrial applications
- Evaluated the effects of composition of acrylic-based latex resins on their physical properties for architectural coatings through synthesis and analysis of the resins
- Delivered two comprehensive presentations on Design of Experiments (DOE) analysis of the synthesized water-borne alkyd-based coatings to managers and senior scientists

Quality Control Manager, QPS Co., Tehran, Iran

August 2011-July 2012

- Managed daily operations of quality control laboratory technicians
- Enhanced the customer satisfaction by ~45% through improving consistency in quality of polyethylene (PE) drip irrigation pipes
- Collaborated with the R&D team for development of U-PVC pipes and fittings
- Teamed with the Soil and Water Research Institute (SWRI) to achieve and maintain certification for drip irrigation pipes

Project Engineer, QPS Co., Tehran, Iran

December 2010-July 2011

- Supervised and led the R&D team to develop an optimized formulation for polyethylene (PE) drip irrigation pipes which resulted in a reduction in manufacturing costs by ~25%
- Supported operations by defining project timelines, and negotiated for the purchase of the essential materials to provide successful manufacturing of the PE pipes for various customers

Teaching Experience

Graduate Teaching Assistant, University of Wisconsin-Milwaukee
Fall 2013-Spring 2018

- Planned lessons, delivered instructions, and created comprehensive assessments for 'Introductory Organic Chemistry Laboratory', 'Organic Chemistry Laboratory' and 'General Chemistry'

Mentor, University of Wisconsin-Milwaukee
Spring 2013-Spring 2018

- Coached undergraduate and graduate students through their research in polymer and organic chemistry

Publications

- “Infrared actuation-induced simultaneous reconfiguration of surface color and morphology for soft robotics”, Banisadr S.; Chen J., Scientific Reports, 2017, 7, DOI: 10.1038/s41598-017-17904-y.
- “Effect of ferric salt of orange peel solid fraction on photo-oxidation and biodegradability of LDPE films” Banisadr S.; Asempour H. Iranian Polymer Journal, 2012, 21 (7), 463-471.

Selected Presentations

- “Infrared Actuation-Induced Simultaneous Reconfiguration of Surface Color and Morphology for Smart Artificial Skins”, Banisadr S.; Chen J., Poster Presentation, 2017 Materials Research Society Fall Meeting, Boston, MA, November 2017.
- “Infrared Actuation-Induced Simultaneous Reconfiguration of Color and Surface Morphology for Smart Robotic Skins”, Banisadr S.; Chen J., Poster Presentation, American Chemical Society Meeting, Milwaukee, WI, May 2017.

Academic Awards and Affiliations

- Sherwin-Williams Cooperative Education Experience Scholarship Award, August 2017
- Chancellor’s Award, University of Wisconsin-Milwaukee, 2012-2018
- Materials Research Society Member, November 2017-Present
- American Chemical Society Member, January 2016-Present
- Academic Excellence Award, Amirkabir University of Technology, Fall 2010

Workshops / Certificates

- Engineering Simulations-ANSYS, edX, Cornell University, 2016
- Chemical Hygiene Plan and Laboratory Safety Training, University of Wisconsin-Milwaukee, 2013
- MATLAB, Tehran Institute of Technology, 2007